

**Probing the influence of relative humidity and temperature on the  
sulfonated silica ceramic carbon electrode for PEM fuel cell operation**

by

Richard Acheampong

A thesis submitted to the  
School of Graduate and Postdoctoral Studies in partial  
fulfillment of the requirements for the degree of

**Master of Science in Materials Science**

Faculty Science

University of Ontario Institute of Technology

Oshawa, Ontario, Canada

May 2019

## THESIS EXAMINATION INFORMATION

Submitted by: **Richard Acheampong**

**Master of Science in Materials Science**

**Thesis title:** Probing the influence of relative humidity and temperature on the sulfonated silica ceramic carbon electrode for PEM fuel cell operation

An oral defense of this thesis took place on May 3, 2019 in front of the following examining committee:

### **Examining Committee:**

Chair of Examining Committee	Dr. Franco Gaspari
Research Supervisor	Dr. E. Bradley Easton
Examining Committee Member	Dr. Brian Ikeda
Examining Committee Member	Dr. Ralph Shiell
Thesis Examiner	Dr. Jean-Paul Desaulniers

The above committee determined that the thesis is acceptable in form and content and that a satisfactory knowledge of the field covered by the thesis was demonstrated by the candidate during an oral examination. A signed copy of the Certificate of Approval is available from the School of Graduate and Postdoctoral Studies.

## **Abstract**

Operation of fuel cells under low relative humidity (RH) and high temperature is a useful way to cut-down cost and increase performance. However, the Nafion ionomer employed in the electrode of the conventional fuel cells performs poorly under low RH and temperatures above 80 °C due to dehydration. A sulfonated silica ceramic carbon electrode (SS-CCE) has been developed to replace the Nafion-based electrode (NBE) because of its hydrophilic and durable nature. Fuel cell testing and diagnostic tools like cyclic voltammetry and electrochemical impedance spectroscopy have been utilized to evaluate polarization losses of different membrane electrode assembly (MEA) configurations for various operating conditions. The configurations include the symmetric NBE MEA, symmetric SS-CCE MEA and asymmetric SS-CCE MEA. Of all the configurations, the asymmetric SS-CCE MEA showed better and stable performance from 80 °C to 95 °C. This indicates that the SS-CCE cathode catalyst layer promotes back diffusion of water generated at the cathode to the anode resulting in an increased performance with temperature and low relative humidity. Moreover, the SS-CCE catalyst showed better stability after an accelerated stress test.

**Keywords:** proton exchange membrane fuel cell; sulfonated silica ceramic carbon electrode; relative humidity; cell temperature; durability

## **AUTHOR'S DECLARATION**

I hereby declare that this thesis consists of original work of which I have authored. This is a true copy of the thesis, including any required final revisions, as accepted by my examiners.

I authorize the University of Ontario Institute of Technology to lend this thesis to other institutions or individuals for the purpose of scholarly research. I further authorize University of Ontario Institute of Technology to reproduce this thesis by photocopying or by other means, in total or in part, at the request of other institutions or individuals for the purpose of scholarly research. I understand that my thesis will be made electronically available to the public.

Richard Acheampong

---

## **STATEMENT OF CONTRIBUTIONS**

I hereby certify that I am the sole author of this thesis and that no part of this thesis has been published or submitted for publication. I have used standard referencing practices to acknowledge ideas, research techniques, or other materials that belong to others. Furthermore, I hereby certify that I am the sole source of the creative works and/or inventive knowledge described in this thesis.

## **Acknowledgements**

My profound gratitude reaches out to my supervisor Professor Easton for the opportunity given me to work in his lab. His office door was always opened to me whenever I had questions regarding my research and writing. Professor Easton gave me the space to work independently yet steered me in the right direction whenever he thought I needed it.

I would like to thank committee members, Dr. Ikeda and Dr. Shiell for serving as my committee members and for their brilliant comments and suggestions.

Special gratitude extends to my fellow mates of the Easton and Zenkina lab. You have all been there supporting me as I worked through this project. I am greatly indebted to your valuable comments during group meetings, always motivating me to widen my research in numerous perspectives. A special mention also of Reza Alipour for taking my SEM and XRD measurements.

To my good friends, Boadu and Nyarko for their availability and support through this research and writing.

I am grateful to the following: OntarioTech University, Ballard Company and NSERC for funding the MSc research.

A special thanks to my family. Words cannot express how grateful I am to the Boateng family for the sacrifices you have made on my behalf. To my parents and siblings thank you for your prayers having sustained me to this far. This achievement would not have been possible without them.

## Table of Contents

<b>Abstract.....</b>	<b>ii</b>
<b>Acknowledgements .....</b>	<b>v</b>
<b>Table of Contents .....</b>	<b>vi</b>
<b>List of Tables .....</b>	<b>x</b>
<b>List of Figures.....</b>	<b>xi</b>
<b>Chapter 1 Introduction.....</b>	<b>1</b>
1.1 An Overview of Fuel Cell Technology .....	2
1.2 Proton Exchange Membrane Fuel Cell .....	5
1.2.1 Proton Exchange Membrane.....	8
1.2.2 Fuel Cell Electrode .....	10
1.2.2.1 Catalyst layer .....	11
1.2.2.2 Gas Diffusion Layer.....	12
1.3 Ceramic-carbon electrodes.....	13
1.3.1 Sulfonated silica ceramic carbon electrodes.....	15
1.4 Electrochemical Techniques.....	17
1.4.1 Polarization Curves.....	17
1.4.2 Cyclic voltammetry .....	19
1.4.3 Electrochemical Impedance Spectroscopy .....	22
1.5 Objectives.....	28
<b>Chapter 2 Materials and Methods.....</b>	<b>29</b>
2.1 Chemicals and Materials .....	30
2.2 Catalyst Ink Preparation .....	30
2.2.1 Nafion-based catalyst ink .....	30
2.2.2 Sulfonated silica ceramic carbon electrode catalyst ink .....	30
2.3 Physicochemical Characterization .....	31
2.3.1 Thermal Gravimetric Analysis .....	31
2.3.2 Brunauer-Emmett-Teller Surface Area and Barrett-Joyner-Halenda Pore Size analysis .....	31
2.3.3 X-Ray Diffraction.....	32
2.3.4 Scanning Electron Microscopy/ Energy Dispersive X-ray Analysis.....	32
2.4 Electrochemical Evaluation.....	33
2.4.1 Fuel Cell System.....	33

2.4.1.1 Gas Diffusion Electrode Fabrication.....	33
2.4.1.2 Membrane Electrode Assembly Fabrication.....	34
2.4.1.2.1 Membrane activation .....	34
2.4.1.2.2 MEA hot-pressing .....	34
2.4.1.3 Single fuel cell test fixture and assembly.....	35
2.4.1.4 Fuel Cell Test Station.....	36
2.4.1.5 MEA Activation (“Break-In”) .....	37
2.4.2 Polarization Curves.....	37
2.4.3 Cyclic Voltammetry .....	39
2.4.4 Hydrogen Crossover .....	39
2.4.5 Electrochemical Impedance Spectroscopy .....	40
2.4.6 Accelerated stress test of the electrodes .....	40
<b>Chapter 3 Results and Discussion .....</b>	<b>42</b>
3.1 Materials Characterization .....	43
3.1.1 Thermogravimetric Analysis .....	43
3.1.2 BET Surface Area and BJH Pore Size Analysis.....	45
3.1.3 X-Ray Diffraction.....	46
3.1.4 Transmission electron microscopy measurements .....	47
3.1.5 Scanning electron microscopy measurements .....	48
3.1.6 Energy dispersive X-ray analysis .....	49
3.2 Electrochemical evaluation of the NBE .....	51
3.2.1 Fuel cell testing.....	51
3.2.1.1 The effect of cathode relative humidity on the NBE MEA .....	51
3.2.1.2 The effect of pure oxygen and air oxidant on the symmetric NBE MEA ..	53
3.2.1.3 The effect of cell temperature on the performance of the symmetric NBE MEA.....	55
3.2.2 Hydrogen crossover and CV measurements of the symmetric NBE MEA.....	57
3.2.2.1 The effect of cathode RH on the Pt electrochemical surface area .....	57
3.2.2.2 The effect of cathode RH on the H <sub>2</sub> crossover.....	58
3.2.2.3 The effect of the cell temperature on Pt electrochemical surface area .....	60
3.2.2.4 The effect of the cell temperature on H <sub>2</sub> crossover.....	61
3.2.3 EIS measurements of the symmetric NBE .....	63
3.2.3.1 EIS measurements of the symmetric NBE MEA at varied cathode RH....	63



3.2.4 The effect of the cell temperature on the NBE conductivity .....	66
3.3 Electrochemical evaluation of sulfonated silica ceramic carbon electrodes .....	69
3.3.1 Fuel Cell Testing .....	69
3.3.1.1 Effect of the cathode RH on the performance of the symmetric SS-CCE MEA.....	69
3.3.1.2 Effect of the temperature on the performance of the symmetric SS-CCE MEA.....	71
3.3.2 Effect of asymmetric SS-CCE MEA configuration on the performance .....	72
3.3.2.1 Influence of the cathode RH on the asymmetric SS-CCE MEA .....	72
3.3.2.2 Influence of temperature on the performance of the asymmetric SS-CCE MEA.....	74
3.3.2.3 Effect of H <sub>2</sub> /air gas feeds on the asymmetric SS-CCE MEA .....	75
3.3.3 Hydrogen crossover and CV measurements of the asymmetric SS-CCE MEA .....	77
3.3.3.1 Effect of cathode RH on Pt electrochemical surface area.....	77
3.3.3.2 Effect of cathode RH on the H <sub>2</sub> crossover .....	78
3.3.4 EIS measurements of the asymmetric SS-CCE MEA .....	80
3.3.4.1 Assessing the conductivity of the asymmetric SS-CCE MEA for various cathode RH.....	80
3.3.4.2 Assessing the Pt ECSA of the asymmetric SS-CCE MEA for various cell temperatures .....	83
3.3.4.3 Effect of the cell temperature on the hydrogen crossover .....	84
3.3.4.4 Effect of the cell temperature on conductivity of the asymmetric SS-CCE MEA.....	85
3.4 Comparison between the NBE and SS-CCE-based MEAs .....	88
3.4.1 Fuel cell performances comparison between the MEA configurations.....	88
3.4.2 EIS data comparison .....	91
3.4.2.1 Comparison between the conductivity of the symmetric NBE and asymmetric SS-CCE MEA for various cathode RH .....	91
3.4.2.2 Comparison between the conductivity of the symmetric NBE and asymmetric SS-CCE MEA for various cell temperature .....	92
3.5 Diagnosing the Degradation of the NBE and SS-CCE catalyst layers.....	93
3.5.1 Potential cycling durability test .....	93
3.5.2 EIS measurements during ADT.....	96
3.6 Pre and Post-test Comparison .....	98

3.6.1 Fuel cell analysis .....	98
3.6.2 TEM analysis .....	99
3.6.3 Energy dispersive X-ray analysis .....	101
<b>Chapter 4 Conclusions and future work.....</b>	<b>104</b>
4.1 Conclusions .....	105
4.2 Future work .....	107
4.3 References .....	109
<b>Appendices.....</b>	<b>117</b>

## List of Tables

Table 2.1 Description of the MEAs tested in this study .....	35
Table 3.1 BET summary of the NBE and SS-CCE catalyst .....	46
Table 3.2 Summary of measured Pt ECSA and H <sub>2</sub> crossover at 80 °C .....	59
Table 3.3 Summary of measured Pt ECSA and H <sub>2</sub> crossover rate for various cell temperature .....	62
Table 3.4 Summary of measured Pt ECSA and H <sub>2</sub> crossover rate for various cathode RH.....	79
Table 3.5 Summary of measured Pt ECSA and H <sub>2</sub> crossover rate as a function of cell temperature .....	85

## List of Figures

<b>Figure 1.1</b> Schematic of a PEM fuel cell. ....	7
<b>Figure 1.2</b> (a) Molecular structure of Nafion, which has a Teflon-like backbone and ether-linked side chains connected to a sulfonic acid group. The equivalent weight (EW) satisfies $EW = 100x + 446$ , if $y = 1$ . For $EW = 1100$ , $x \approx 6.5$ . (b) Cluster-network model: hydrophilic clusters connected by short narrow channels, short curves: Nafion side chains.....	9
<b>Figure 1.3</b> Transport processes in the cathode gas diffusion electrode. ....	11
<b>Figure 1.4</b> Sol-gel reaction mechanism .....	14
<b>Figure 1.5</b> Schematic of a ceramic-carbon electrode <sup>[27]</sup> (Reproduced with permission).....	14
<b>Figure 1.6</b> Structural comparison of the unsulfonated and sulfonated organosilane precursors.....	16
<b>Figure 1.7</b> Typical polarization curve of PEM fuel cell .....	18
<b>Figure 1.8</b> Cyclic voltammogram of a Pt electrode in a PEM fuel cell. Arrows showed the forward and reverse directions. The numbers showed various electron reaction involving dissolved species. ....	20
<b>Figure 1.9</b> Transmission Line Model for impedance spectroscopy of porous electrode. ....	25

<b>Figure 1.10</b> EIS response of PEM fuel cell under H <sub>2</sub> /N <sub>2</sub> at 30 °C represented by (a) Nyquist (b) Capacitance and (c) Normalized capacitance plot.....	27
<b>Figure 2.1</b> Fabrication process of gas diffusion electrode .....	33
<b>Figure 2.2</b> (a) Expanded view of the Nuvant cell and (b) an assembled Nuvant cell.....	36
<b>Figure 2.3</b> A Commercial Fuel Cell Test Station .....	37
<b>Figure 3.1</b> TGA/DTG scans in flowing air for the Premetek (commercial catalyst), the NBE and the SS-CCE; temperature was ramped at 20 °C/min to 1000 °C.....	44
<b>Figure 3.2</b> Volume of nitrogen plotted as a function of relative pressure as measured during BET surface analysis of (a) NBE and (b) SS-CCE catalyst. ....	45
<b>Figure 3.3</b> XRD patterns of 20% Pt on Vulcan XC-72 (Premetek) and SS-CCE catalysts.....	46
<b>Figure 3.4</b> TEM images of a (a) 20% Pt/C, Premetek, (b) NBE and (c) SS-CCE catalyst layers.....	47
<b>Figure 3.5</b> SEM image of SS-CCE of (a) 2.00k (b) 5.00k magnifications. ....	48
<b>Figure 3.6</b> (a) EDX spectrum of SS-CCE and (b) elemental mapping of SS-CCE catalyst layer. ....	49
<b>Figure 3.7</b> Cross-sectional SEM images (a) and EDS mapping (b) of the SS-CCE. ....	50

<b>Figure 3.8</b> Performance curves of the symmetric NBE MEA at various cell temperatures a) 70 °C b) 75 °C c) 80 °C and d) 85 °C as a function of the cathode RH where anode fixed at 100% RH. The flow rates of H <sub>2</sub> and O <sub>2</sub> supplied were 100- and 200-mL min <sup>-1</sup> with back pressure of 10 psig. ....	52
<b>Figure 3.9</b> Peak power density vs cathode RH plots obtained for Figure 3.8 data where a) 70 °C b)75 °C c) 80 °C d) 85 °C cell temperatures. ....	53
<b>Figure 3.10</b> Performance curves of the symmetric NBE MEA with (a) H <sub>2</sub> /O <sub>2</sub> (b) H <sub>2</sub> /air gas feeds configuration at cell temperature 85°C with varied cathode RH and anode fixed 100% RH. The flow rate of H <sub>2</sub> was 100 mL min <sup>-1</sup> and O <sub>2</sub> and air were 200- and 1000-mL min <sup>-1</sup> respectively with 10 psig backpressure. ....	54
<b>Figure 3.11</b> Performance curves of the symmetric NBE MEA as a function of the cell temperature with (a) H <sub>2</sub> /O <sub>2</sub> (b) H <sub>2</sub> /air gas feeds. The flow rate of H <sub>2</sub> was 100 mL min <sup>-1</sup> and O <sub>2</sub> and air were 200- and 1000-mL min <sup>-1</sup> respectively with 10 psig backpressure. Both gases were humidified at 100% RH. ....	55
<b>Figure 3.12</b> Peak power density vs cell temperature plots extracted from the Figure 3.11 .....	56
<b>Figure 3.13</b> (a) CVs (20 mV s <sup>-1</sup> ) and (b) ECSA obtained for symmetric NBE MEA at 80 °C under H <sub>2</sub> /N <sub>2</sub> gas feeds. The cathode was varied between 20% and 100% RH where anode was fixed at 100% RH. Backpressure applied to both sides was 10 psig. ....	57

<b>Figure 3.14</b> (a) Chronoamperogram (insert = expanded graph) and (b) current measured as a function of the cathode RH for symmetric NBE MEA at a potential of 0.5 V vs RHE under H <sub>2</sub> /N <sub>2</sub> at 80 °C. The anode was fixed at 100% RH whereas the cathode RH was varied from 20 to 100% RH. The backpressure to both sides was 10 psig.....	58
<b>Figure 3.15</b> (a) CVs (20 mV s <sup>-1</sup> ) and (b) ECSA obtained for the symmetric NBE MEA at various cell temperature from 70 °C to 95 °C under H <sub>2</sub> /N <sub>2</sub> gas feeds. Both the anode and cathode gases were humidified at 100% RH. Backpressure applied at both sides was 10 psig.....	60
<b>Figure 3.16</b> (a) Chronoamperogram (inserted = expanded (a)) and (b) current measured with symmetric NBE MEA at a potential of 0.5 V vs RHE under H <sub>2</sub> /N <sub>2</sub> at various cell temperature from 70 °C to 95°C. The anode and cathode was fixed at 100% RH. The backpressure on both sides was 10 psig. ....	61
<b>Figure 3.17</b> (a) Nyquist (b) capacitance and (c) normalized capacitance plots for the symmetric NBE MEA at 80 °C under H <sub>2</sub> /N <sub>2</sub> gas feeds. The anode was fixed at 100% RH whereas the cathode RH was varied between 20 to 100%. DC bias potential of 0.425 V was applied. Backpressure of 10 psig was applied on both sides. ....	63
<b>Figure 3.18</b> Expansion of the high frequency region of the Nyquist plot.....	64
<b>Figure 3.19</b> (a) Membrane resistance (b) total ionic resistance and (c) limiting capacitance of the symmetric NBE MEA as a function of cathode RH at 80 °C.....	66

<b>Figure 3.20</b> (a) Nyquist (b) capacitance and (c) normalized capacitance plots obtained for the symmetric NBE MEA as a function of the cell temperature under H <sub>2</sub> /N <sub>2</sub> gas feeds. The anode and cathode gases were humidified at 100% RH. DC bias potential of 0.425 V was applied. Backpressure of 10 psig was applied on both sides.....	67
<b>Figure 3.21</b> Expansion of the high frequency region of the Nyquist plot.....	67
<b>Figure 3.22</b> (a) membrane resistance (b) total ionic resistance and (c) limiting capacitance of the symmetric NBE MEA as a function of the cell temperature from 70 to 95 °C at 100% RH. ....	69
<b>Figure 3.23</b> Performance curves of the symmetric SS-CCE MEA for various cell temperatures: a) 70 °C b) 75 °C c) 80 °C d) 85 °C and cathode RH where the anode is fixed at 100% RH. The flow rates of H <sub>2</sub> and O <sub>2</sub> supplied were 100- and 200-mL min <sup>-1</sup> with a back pressure of 10 psig.....	70
<b>Figure 3.24</b> (a) Performance curves of the symmetric SS-CCE MEA as a function of the cell temperature with H <sub>2</sub> /O <sub>2</sub> and (b) peak power density vs cell temperature curves. The flow rate of H <sub>2</sub> and O <sub>2</sub> was 100 and 200 mL min <sup>-1</sup> respectively with 10 psig backpressure. Both gases were humidified at 100% RH. ....	72
<b>Figure 3.25</b> (a) Performance curves and (b) peak power density of the asymmetric SS-CCE MEA at 85 °C and various cathode RH, ranging from 20% to 60% where anode is kept at 100% RH. The flow rate of H <sub>2</sub> and O <sub>2</sub> was 100- and 200-mL min <sup>-1</sup> respectively with 10 psig backpressure. ....	73



**Figure 3.26** (a) Performance and (b) peak power density curves for the asymmetric SS-CCE MEA as a function of the cell temperature at 100% RH. The flow rate of H<sub>2</sub> and O<sub>2</sub> was 100- and 200-mL min<sup>-1</sup> respectively with a 10 psig backpressure. .... 74

**Figure 3.27** Performance curves of the asymmetric SS-CCE MEA as a function of (a) cathode relative humidity at 80 °C and (b) cell temperature at 100% RH. The flow rate of H<sub>2</sub> and air was 100- and 1000-mL min<sup>-1</sup> respectively with 10 psig backpressure. 76

**Figure 3.28** Peak power density vs (a) cathode RH at 80 °C and (b) cell temperature at 100% RH plots extracted from Figure 3.27. .... 76

**Figure 3.29** (a) CVs (20 mV s<sup>-1</sup>) and (b) ECSA measured for asymmetric SS-CCE MEA at 80°C under H<sub>2</sub>/N<sub>2</sub> gas feeds. The cathode was varied between 20 and 100% RH where anode was fixed at 100% RH. Backpressure applied at both sides was 10 psig..... 77

**Figure 3.30** (a) Chronoamperogram and (b) current measured with asymmetric SS-CCE MEA at a potential of 0.5 V vs RHE under H<sub>2</sub>/N<sub>2</sub> at 80 °C. The anode was fixed at 100% RH whereas the cathode RH was varied from 20 to 100% RH. The backpressure on both sides was 10 psig..... 78

**Figure 3.31** (a) Nyquist, (b) capacitance, and (c) normalized capacitance plots for the asymmetric SS-CCE MEA at 80 °C under H<sub>2</sub>/N<sub>2</sub> gas feeds. The anode was fixed at 100% RH whereas the cathode RH was varied between 20% and 100%. DC bias potential of 0.425 V was applied. Backpressure of 10 psig was applied on both sides. .... 80

<b>Figure 3.32</b> Expansion of the high frequency region of the Nyquist plot from which the ionic resistances were estimated. ....	81
<b>Figure 3.33</b> (a) Membrane resistance (b) total ionic resistance and (c) limiting capacitance of the asymmetric SS-CCEE MEA as a function of cathode RH at 80 °C. ....	82
<b>Figure 3.34</b> (a) CVs (20 mV s <sup>-1</sup> ) and (b) ECSA obtained for the asymmetric SS-CCE MEA at various cell temperature from 70 °C to 95 °C under H <sub>2</sub> /N <sub>2</sub> gas feeds. Both the anode and cathode gases were humidified at 100% RH. Backpressure applied to both sides was 10 psig.....	83
<b>Figure 3.35</b> (a) Chronoamperogram and (b) HOR current measured with asymmetric SS-CCE MEA at a potential of 0.5 V vs RHE under H <sub>2</sub> /N <sub>2</sub> at various cell temperature from 70 to 95°C. The anode and cathode were fixed at 100% RH. The backpressure on both sides was 10 psig. ....	84
<b>Figure 3.36</b> Presents the Nyquist (a) and capacitance plots (b&c) obtained with the asymmetric SS-CCE MEA as a function of the cell temperature under H <sub>2</sub> /N <sub>2</sub> gas feeds. The anode and cathode gases were humidified at 100% RH. DC bias potential of 0.425 V was applied. Backpressure of 10 psig was applied on both sides. ....	86
<b>Figure 3.37</b> Expansion of the high frequency region of the Nyquist plot.....	86
<b>Figure 3.38</b> (a) Membrane resistance (b) total ionic resistance and (c) limiting capacitance of the asymmetric SS-CCE MEA as a function of the cell temperature from 70 to 95 °C at 100% RH. ....	88

<b>Figure 3.39</b> Peak power density comparison of the symmetric NBE, a symmetric SS-CCE and asymmetric SS-CCE MEA as a function of the cathode RH at 85 °C. ....	89
<b>Figure 3.40</b> Peak power density comparison for the symmetric SS-CCE, symmetric NBE and asymmetric SS-CCE MEA as a function of cell temperature at 100% RH. ....	90
<b>Figure 3.41</b> Comparison of the (a) membrane resistance (b) total ionic resistance and (c) capacitance of the symmetric NBE and the asymmetric SS-CCE MEA as a function of the cathode RH at 80 °C. ....	91
<b>Figure 3.42</b> (a) Membrane resistance, (b) total ionic resistance, and (c) limiting capacitance comparison of the NBE and the asymmetric SS-CCE MEA as a function of the cell temperature at 100% RH.....	93
<b>Figure 3.43</b> CVs recorded at different cycles for (a) NBE MEA and (b) Asymmetric SS-CCE MEA at 30 °C under H <sub>2</sub> /N <sub>2</sub> . ....	94
<b>Figure 3.44</b> Estimated ECSA from the CVs (Figure 3.44) as a function of the number of cycles .....	95
<b>Figure 3.45</b> Comparison of the EIS data of the symmetric NBE MEA (left) and the asymmetric SS-CCE MEA (right) collected under H <sub>2</sub> /N <sub>2</sub> at dc bias potential 0.425 V. ....	96
<b>Figure 3.46</b> Expansion of the high frequency region of Figure 3.45.a of the (a) symmetric NBE (b) asymmetric SS-CCE MEA.....	97

<b>Figure 3.47</b> Pre and Post-tests performance curves for the (a) symmetric NBE and (b) Asymmetric SS-CCE MEA under H <sub>2</sub> /O <sub>2</sub> at 85 °C cell temperature; anode and cathode kept at 100% RH; backpressure on both sides is 10 psig. ....	98
<b>Figure 3.48</b> TEM analysis of the NBE (A&B) and SS-CCE (C&D) catalyst and their corresponding size distribution. The analysis was performed using a Jeol 2010F field emission gun (FEG) operated at 200 kV. The microscope is equipped with an Oxford Inca EDS system. ....	100
<b>Figure 3.49</b> Postmortem EDX analysis of the NBE catalyst layer: A) Fresh catalyst B) End-of-test analysis using a Jeol 2010F field emission gun (FEG) operated at 200 kV. The microscope is equipped with an Oxford Inca EDS system. ....	102
<b>Figure 3.50</b> Post mortem EDX analysis of the SS-CCE catalyst layer: A) Fresh catalyst B) End-of-test analysis using a Jeol 2010F field emission gun (FEG) operated at 200 kV. The microscope is equipped with an Oxford Inca EDS system. ....	103

## **LIST OF ABBREVIATIONS AND SYMBOLS**

AC	– Alternating current
AST	– Accelerated stress test
BET	– Brunauer-Emmett-Teller
BJH	– Barrett-Joyner-Halenda
C	– Capacitance
CCE	– Ceramic Carbon Electrode
CCM	– Catalyst coated membrane
CE	– Counter electrode
CL	– Catalyst Layer
CV	– Cyclic voltammetry
DC	– Direct current
DTG	– Differential thermal gravimetry
DI	– Deionized
ECSA	– Electrochemically active surface area
EDX	– Energy dispersive X-ray
EIS	– Electrochemical impedance spectroscopy
EW	– Equivalent weight
GDE	– Gas diffusion electrode
GDL	– Gas diffusion layer
GHG	– Greenhouse gas
HOR	– Hydrogen oxidation reaction
I	– Current
MEA	– Membrane electrode assembly
MPL	– Microporous layer
NBE	– Nafion-based electrode
OCV	– Open circuit voltage
ORR	– Oxygen reduction reaction

PEM – Proton exchange membrane  
PTFE – Poly(tetrafluoroethylene)  
PFSA – Perfluorosulfonic acid  
 $R_{\text{electronic}}$  – Electronic resistance  
 $R_{\text{ionic}}$  – Ionic resistance  
RE – Reference electrode  
RH – Relative humidity  
RHE – Reversible hydrogen electrode  
 $R_M$  – Membrane resistance  
 $R_{\Sigma}$  - Total catalyst layer resistance  
SEM – Scanning electron microscopy  
SHE – Standard Hydrogen Electrode  
SS-CCE – sulfonated silica ceramic carbon electrode  
SPEEK – sulfonated polyether ether ketone  
TEM – Transmission electron microscopy  
TEOS – Tetraethyl orthosilicate  
TGA – Thermogravimetric analysis  
TPS – 3-(trihydroxysilyl)-1-propanesulfonic acid  
WE – Working electrode  
XRD – X-ray diffraction

## **Chapter 1 Introduction**

## 1.1 An Overview of Fuel Cell Technology

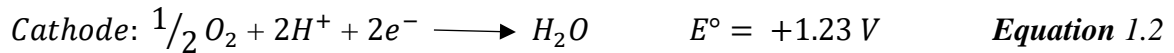
Fossil fuels including coal, oil and natural gas remain dominant energy sources on which the world depend to power homes, vehicles, industry, etc.<sup>[1]</sup> However, the production and combustion of these fuels produce million of tons of carbon dioxide (CO<sub>2</sub>) and other greenhouse gases (GHGs) in the atmosphere.<sup>[2]</sup> The increased atmospheric concentration of CO<sub>2</sub> (over 400 parts per million) are the primary contributor to current climate changes and global warming.<sup>[2-4]</sup> These have led to extreme weather around the globe, such as flooding, droughts, high winds, runaway fires, and high seas in coastal areas.<sup>[3]</sup> In order to circumvent the environmental and health issues associated with climate change, there is a need to shift our energy systems from fossil fuels that produce greenhouse gases towards renewable energy that are not harmful. Among the many renewable energy sources considered, hydrogen-powered systems has been identified to be one of the best way to cut-down CO<sub>2</sub> emissions.<sup>[5]</sup>

Hydrogen can be produced by reforming fossil fuels or biomass. This paves the way for using fossil fuel in the most efficient and environment-friendly manner. It can also be produced by electrolysis (i.e., splitting water into hydrogen and oxygen) using hydroelectricity, solar, wind and nuclear power sources.<sup>[6]</sup> Hydrogen fuel can be harnessed by fuel cell devices to produce electricity. These devices are being lauded for their free carbon emissions. Therefore, fuel cells have the potential to eliminate major issues associated with the production and consumption of energy.<sup>[1]</sup>

A fuel cell is an electrochemical device that converts chemical energy into electrical energy. At the basic level, it is made up of an electrolyte sandwiched between two electrodes: one negative electrode (anode) and the other positive electrode (cathode).



The anode compartment is fed with hydrogen while the cathode compartment is fed with oxygen. The hydrogen at the anode side splits into protons and electrons (i.e., hydrogen oxidation reaction), protons goes through the electrolyte whereas electrons flow through an external circuit as useful electricity. The protons and electrons combine with oxygen at the cathode side to generate water and heat as the only by-products.<sup>[7]</sup> In certain types of fuel cell, ions travels from the cathode to the anode side, yet, the principle remains the same. In an acid electrolyte, the half reactions occurring at both sides of the electrodes are given as:



Most often, fuel cells are compared to batteries, since both produces electricity through chemical reactions. However, unlike a battery, a fuel cell produces energy if fuel (H<sub>2</sub>) and oxidant (O<sub>2</sub>) are supplied. Therefore, fuel cells are refueled as opposed to recharged.<sup>[7]</sup> With fuel cells, a desired amount of power can be generated by the number of single cells combined (i.e., fuel cell stack).

Historically, the term “fuel cell” was first coined by Sir William Groove in 1839. In the 1842, Groove invented the fuel cell and called it the “gaseous voltaic battery”, which produced electricity by combining hydrogen and oxygen.<sup>[8]</sup> However, fuel cells remained unpractical due to lack of theoretical understanding of how it operates. About a century later, an English engineer, Francis Thomas Bacon successfully demonstrated the practical use of a 5 kW fuel cell stack in 1952.<sup>[8]</sup>

Recent developments in fuel cell technology clearly prove that the future clean energy generation could belong to the hydrogen economy. Fuel cells can power almost all devices that require electricity for its operation, and it is probably the most versatile energy generation technology ever invented. The fuel cell has been employed in different applications including transportation and stationary, portable and micropower because of their high efficiency (40% – 60%), no or low emissions, silent operation, and no moving parts, which is expected to extend life.<sup>[8]</sup>

Besides the advantages of the fuel cell, there are several key challenges towards their commercial viability. These include cost, durability and lack of hydrogen infrastructure.<sup>[5]</sup> Cost is the primary hurdle of fuel cell commercialization. The key cost factors of manufacturing fuel cell are the platinum catalyst, the membrane and the bipolar plates.<sup>[5]</sup> Recent developments have focused on cost reduction approaches including reducing or replacing precious platinum with less expensive metal catalyst.<sup>[9]</sup> Durability is another obstacle that fuel cells must overcome, especially for the automotive application. The current fuel cell systems must meet the durability target (i.e., 5000 h at a laboratory scale) of the US Department of Energy for automotive applications which would make them competitive with the ICE in the world market. Another major issue is the lack of hydrogen infrastructure. Hydrogen production, storage and distribution are key areas to expand on to achieve market success for fuel cells and this may require a significant capital investment.<sup>[7,8,10]</sup>

Over the last two decades, a large number of fuel cell related papers and patents have been approved and applied in various challenging areas to facilitate development.<sup>[8]</sup> Huang et al.<sup>[10]</sup> compiled and analyzed papers and patents related to the fuel cell field from

1991 to 2010 focusing on the scientific and technical development trends in fuel cell technology. They reported that the number of papers and patents published between 1991 and 2003 as relatively small, but after 2003, there was a dramatic increase of publications. This signifies the continuous interest and involvement of the scientific and engineering community to make fuel cell viable and affordable. The United States, China, and Japan have shown keen interest in this field contributing more than half of the overall papers and patents published worldwide.<sup>[10]</sup> Overall, the first quarter of this century has seen significant progress of fuel cell systems and have been demonstrated in various applications from battery chargers to home heating and power to cars.

Fuel cells are generally grouped into various types and operates at different temperatures. They are mainly classified according to the type of electrolyte use. Based on recent reports, the proton exchange membrane (PEM) fuel cells have attracted much attention among the various types of fuel cells. Therefore, the next section of this report presents a concise review of the PEM fuel cell.

## **1.2 Proton Exchange Membrane Fuel Cell**

The PEM fuel cell has been recognized as a distinct fuel cell technology to power transportation (e.g., cars, trucks, buses and ships), stationary (e.g., combined heat and power, and uninterruptible power supplies) and portable devices (e.g., torches, battery charges, cameras, etc.). This is because of its low emission, high efficiency and quiet operation.<sup>[11,12]</sup> Its most efficient and economical operation conditions occur at high pressures and high temperatures therefore, intense research has been dedicated to their development to broadening its operation for these conditions. For example, low relative humidity operation can eliminate the need for large humidifiers and simplify system

design.<sup>[13]</sup> Also, operating at high temperatures offers several advantages including the effective removal of heat where a small radiator would be required to remove heat more effectively due to the large temperature difference between the system and its surroundings. This could be of great benefit for transportation systems. Increasing temperature could enhance water management where issues like flooding would be eliminated from the fuel cell systems. Moreover, operating at high temperatures improves the catalyst tolerance to carbon monoxide poisoning, which allows low cost reformat hydrogen fuel to be used.<sup>[11,14,15]</sup> In this regard, it is of great interest to explore new materials that have superior performance and durability under elevated temperatures and low relative humidities.

Recent studies have shown that the addition of hydrophilic particles to either the catalyst or membrane could enhance performance under low relative humidity and high temperature.<sup>[11,15–31]</sup> The quest for low cost and durable materials continue to be the driving force for further research on PEM fuel cell.

The PEM fuel cell stand out from other fuel cells because of its immobile electrolyte. The PEM's solid proton conducting electrolyte simplifies sealing during the production process, reduces corrosion which in turn could extend the cell's life.<sup>[7]</sup> Considering these unique qualities make it a suitable alternative to replace the traditional ICE.

As shown in Figure 1.1, a single PEM fuel cell basically consists of two electrodes sandwiching a membrane electrode assembly (MEA). A PEM fuel cell stack can also be built by connecting cells in series to produce a required amount of power. The MEA is termed the heart of the PEM fuel cell since it is where all the electrochemical processes occur. The MEA is made up of a solid proton conductor (i.e., the PEM), catalyst layers (CLs) and gas diffusion layers (GDLs). Technically, these components are fabricated

individually and then pressed together, with an appropriate temperature and pressure, to form MEA. The characteristics of the MEA components play a key role in the overall performance of the PEM fuel cell. The MEA also serves as a separator for the anode and cathode compartments of the fuel cell. There are several processes that occur in the PEM fuel cell. These include:

1. the flow of gas through channels and their diffusion through porous media (i.e., GDL and CL),
2. the transport of protons through the PEM and electrons through the GDL and graphite plates, and
3. the water transport processes either by electro-osmotic drag (i.e., from anode to cathode) or back diffusion (i.e., from cathode to anode).<sup>[8]</sup>

These processes are most influence by several parameters such as cell temperature, relative humidity, pressure and reactants flow rates.

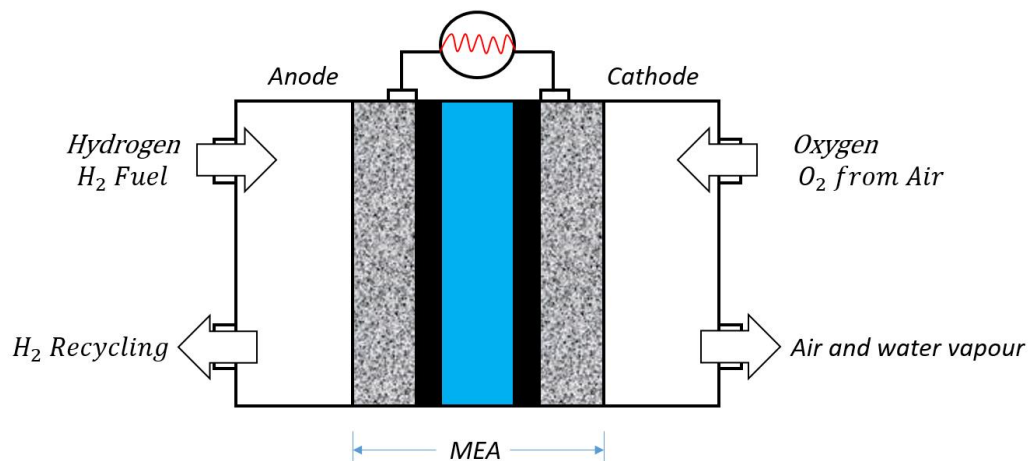


**Figure 1.1** Schematic of a PEM fuel cell.

### 1.2.1 Proton Exchange Membrane

The PEM is one of the key materials that makes the PEM fuel cell more attractive to various applications, especially for transportation (electric vehicle). The PEM serves as the medium through which protons and water travel. It also functions as a barrier to mixing of fuel and oxidants at the anode and cathode compartments respectively.<sup>[8]</sup> A PEM material must exhibit high proton conductivity ( $> 100 \Omega \text{ cm}^{-1}$ ), chemical and mechanical stability under fuel cell operating conditions, impermeability of fuels and oxidants, and good water transport capability (high water flux) from the cathode to the anode.<sup>[32]</sup>

The PEM of fuel cells is a type of cation exchange membrane traditionally made of perfluorosulfonic acid (PFSA) ionomer. This is basically a copolymer of poly(tetrafluoroethylene) (PTFE) and poly(trifluoroethylene) substituted with sulfonic acid group.<sup>[32]</sup> It is a strong ion-exchange material because of the substituted functional group ( $\text{SO}_3\text{H}$ ), which easily dissociate into a mobile cation ( $\text{H}^+$ ) and the corresponding immobilized counter ion ( $\text{SO}_3^-$ ).<sup>[33]</sup>

The most prominent PFSA membrane is Nafion, developed by DuPont in the late 1960s, and, for this reason, it is helpful to understand its chemical structure. Figure 1.2.a. shows the molecular structure of Nafion. The structure is made up of a Teflon-like backbone connecting the sulfonic acid group. Because of different hydrophilicities of each region, the structure shows phase separation into hydrophobic (backbone) and hydrophilic (sulfonic acid group) domains.<sup>[33]</sup> The function of the hydrophobic domain (backbone) is to provide mechanical strength and dimension stability, whereas the hydrophilic domain (sulfonic acid groups) provides proton conductivity.<sup>[7,31]</sup> Based on the cluster model of Nafion membrane shown in Figure 1.2.b. <sup>[33,34]</sup>, the sulfonic ion clusters is about 4 nm and

are uniformly dispersed in a continuous fluorocarbon lattice interconnected with narrow channels with diameter of approximately 1 nm. These channels serve as a route for protons transport.<sup>[34]</sup> Protons are transported along with about 3 to 5 water molecules from the anode to the cathode side through these channels.<sup>[34]</sup>

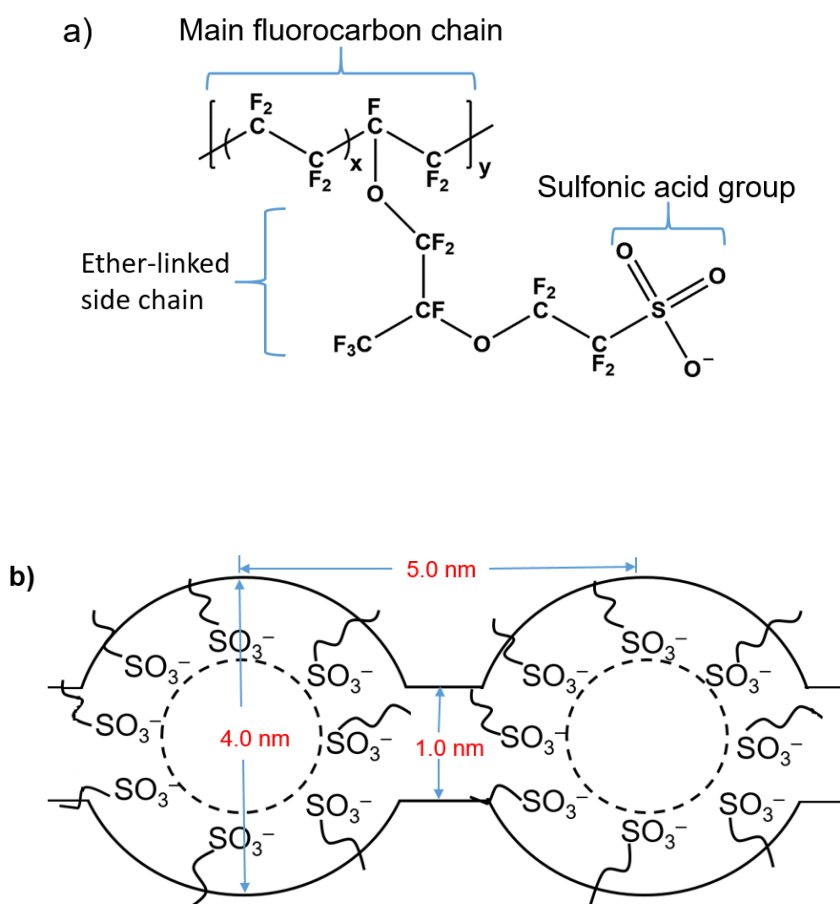


**Figure 1.2** (a) Molecular structure of Nafion, which has a Teflon-like backbone and ether-linked side chains connected to a sulfonic acid group. The equivalent weight (EW) satisfies  $EW = 100x + 446$ , if  $y = 1$ . For  $EW = 1100$ ,  $x \approx 6.5$ . (b) Cluster-network model: hydrophilic clusters connected by short narrow channels, short curves: Nafion side chains.

The proton conductivity of the Nafion membrane depends strongly on its water content. Nafion membranes are known to exhibit sufficient proton conductivity when fully hydrated (high relative humidity), which could be susceptible to poor conductivity when dehydrated.<sup>[35]</sup>

### **1.2.2 Fuel Cell Electrode**

A PEM fuel cell electrode is the structure that stretches from the surface of the PEM to the bipolar plate of the cell. It is made up of a continuous network of a thin catalyst layer (CL) bonded onto a porous, electrically conductive substrate (e.g. carbon paper or carbon cloth).<sup>[8]</sup> The catalyst can either be deposited onto the PEM, which is termed as a catalyst coated membrane (CCM) or the GDL also known as the gas diffusion electrode (GDE). The electrode provides the platform for hydrogen oxidation reaction (HOR) and oxygen reduction reaction (ORR) in their respective compartment. The structure of the electrode greatly influences the transport processes that occur in the cell. Therefore, a well-structured electrode must effectively accommodate these processes for high efficiency of the cell. Figure 1.3 shows the transport processes occurring at the cathode of the PEM fuel cell, and include:<sup>[36]</sup>

1. the proton transport from the anode via the membrane to the CL,
2. electrons transport from the current collector through the GDL, and
3. the transport of reactant gases and product water to and from the electrode respectively.



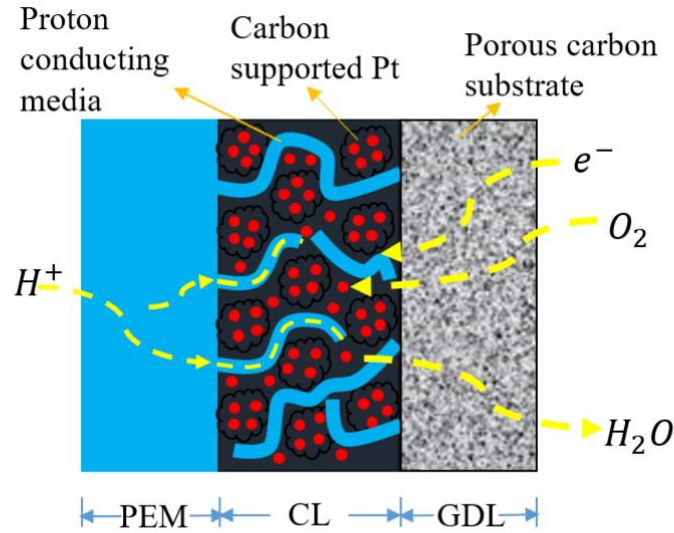


**Figure 1.3** Transport processes in the cathode gas diffusion electrode.

Moreover, the active portion of the electrode is where the protons, electrons and gases have contact (i.e., where electrochemical reaction can take place). The intersection of these three species is referred to as the three-phase boundary.<sup>[8]</sup> Therefore, the electrode is designed such that the pathway for these species are uniformly distributed throughout the CL to reduce transport losses.<sup>[36]</sup> The CL and GDL play a unique role in the GDE and will be discussed in the following sections.

### 1.2.2.1 Catalyst layer

As shown in Figure 1.3, the CL is sandwiched between the PEM and the GDL and is where both HOR and ORR take place. The thin film CL is cast from a homogenous mixture of solubilized ionomer and carbon supported platinum. The catalyst “ink” is deposited on either the PEM or the GDL by several methods including spraying, sputtering, painting, screen printing, decaling, evaporative deposition and spreading.<sup>[8]</sup> The main objective is to establish an infinitesimally small area between the membrane and the CL to reduce contact resistance.<sup>[36]</sup> The traditional PEM fuel cell CL, as depicted in Figure 1.3,

can be described as a continuous network of ionomer (Nafion), platinum particles (size  $\sim 2 - 6$  nm) and carbon particles ( $20 - 50$  nm).<sup>[37]</sup> The catalyst structure is constructed such that the three main species that contribute to the electrochemical reactions have access. The three species are gases, electrons and protons. Within this structure, electrons move through the electronically conductive materials (i.e., the carbon support) while the ionomer creates routes for proton transport and serves as a binder of the platinum-carbon nanoparticles. The through-connected pore network (i.e., voids) in the catalyst provides a pathway for the mass transport of reactants gases and the removal of product water to and from the CL respectively.<sup>[8,37]</sup> Recently, remarkable achievements have been reported in the development of PEM fuel cell electrocatalyst where high performances can be obtained with low Pt loading ( $< 0.20$  mg cm<sup>-2</sup>). This has drastically reduced the cost of platinum-based electrocatalyst.

#### **1.2.2.2 Gas Diffusion Layer**

The GDL is composed of a porous carbon paper or cloth backing, at times coated with a microporous layer (MPL) to manage water in the cell. The MPL is composed of teflonized carbon (e.g., PTFE) that ensures the pores of the carbon backing do not clog up with liquid water. The GDL provides a mechanical support to the CL. It also provides pathways for effective diffusion of the reactant gases to the entire active area of the catalyst layer. In addition, the GDL electrically connects the catalyst layer to the bipolar plate that transport electrons to and from the catalyst layer. Finally, the thickness of the GDL must be in the range of  $100 - 300$   $\mu\text{m}$  to avoid mass transport issues.<sup>[36]</sup>

The electrodes are designed to transport gasses, electrons and protons to the catalyst layer for high fuel cell performance.

### 1.3 Ceramic-carbon electrodes

One of the key components in the fuel cell electrode is the ionomer. The ionomer not only aid in protons conduction, but also serves as a binder for the carbon supported platinum (Pt/C) matrix. A typical conventional ionomer is a solubilized Nafion. The Nafion is an expensive material and requires to be highly humidified to perform better. These have become an impediment to operating PEM fuel cell under low relative humidity, which could reduce parasitic power losses due to gas humidification.<sup>[38]</sup> Therefore, there is a great deal of interest in finding alternatives ionomers to the perfluorosulfonic acid ionomers (e.g., Nafion).

The ceramic carbon electrode (CCE) has developed rapidly over the last decade and has become an area of active research. One advantage of the CCE over Nafion is cost. In addition, CCE materials are more hydrophilic, which is reflected in the increased water uptake of their composite materials.<sup>[15–20,28,29,31,38–45]</sup> Therefore, the ability of CCE composites to retain water in dry environments (i.e., low relative humidity and high temperature) make them attractive for high temperature PEM fuel cell operation. Moreover, their chemical structure can easily be modified to fit an application. As a result, several research groups have demonstrated different applications of CCE for a wide variety of electrochemical applications, including biosensing<sup>[46]</sup>, electrocatalysis<sup>[47]</sup> and energy storage cells.<sup>[19,20,29,38,40,42,44]</sup>

For fuel cell electrodes, the Pt/C catalyst can be held together by a ceramic binder through a process known as the sol-gel reaction.<sup>[48]</sup> The sol-gel process involves several chemical reactions that occur simultaneously to produce gels from colloidal suspensions or sol.<sup>[48]</sup> As shown in Figure 1.4<sup>[48]</sup>, the tetraethyl orthosilicate (TEOS) in water solution

undergoes hydrolysis and condensation to produce silicate sol, which can subsequently be gelled.

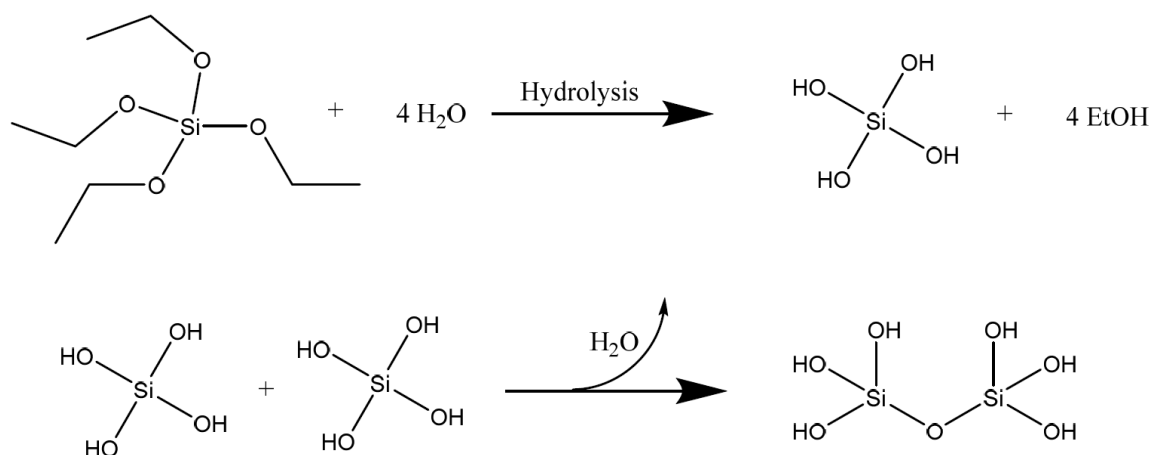


**Figure 1.4** Sol-gel reaction mechanism

During a sol-gel process, silicon atoms could form stable Si-C bonds that are resistant to air oxidation and to hydrolysis.<sup>[48]</sup> This class of compound provide a bridge between inorganic and organic elements. As the sol-gel reaction proceeds, the Pt/C particles are interconnected through the silicate chains, as depicted in Figure 1.5.

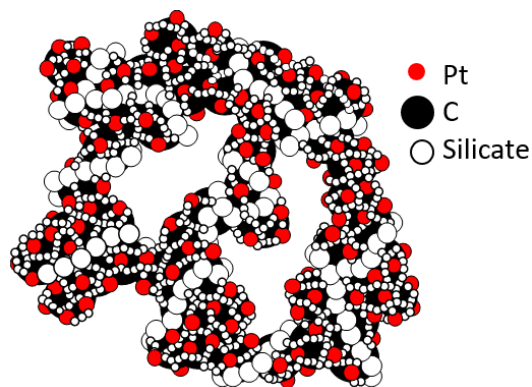


**Figure 1.5** Schematic of a ceramic-carbon electrode .<sup>[27]</sup> (Reproduced with permission)

As a result, the electrode material benefits from the mechanical properties of the silicate backbone and from the uniform carbon distribution in the electrode (i.e., enhancing electron conductivity). In addition, the preparation method allows control over the physicochemical characteristics of the electrode. A suitable monomer precursor can be incorporated to affect certain properties, such as proton conductivity. Recent work<sup>[49]</sup> in our laboratory shows that small quantities of sulfonated silane (e.g., the 3-(trihydrosilyl)-1-propanesulfonic acid, TPS) combined with TEOS enhanced the proton conductivity as well as the hydration capability of the electrode.

### **1.3.1 Sulfonated silica ceramic carbon electrodes**

While ceramic carbon electrodes (CCE) have been considered as the potential alternative to replace Nafion-based electrodes (NBE), there are still issues that need to overcome to realize the full potential of the CCE as fuel cell electrodes. Despite the CCE's remarkable performance under dry conditions, their catalytic activity is still a hurdle to overcome. Therefore, improving catalytic activity and finding an optimum silane loading will make CCE viable for a wide range of operating conditions from low to high temperature operation.

Recent studies in our lab have been dedicated to the investigation of the sulfonated silica ceramic carbon electrode (SS-CCE), aimed to improve the catalytic activity of the CCE. The SS-CCE is a modified form of the CCE, where an organosilane precursor with a sulfonic acid group is added to an unsulfonated organosilane precursor (e.g., TEOS) to improve proton conductivity. In here, TPS was investigated as the sulfonated organosilane

precursor. As shown in Figure 1.6, the TPS structure contains a sulfonic acid functional group like that found in the Nafion ionomer (Figure 1.2.a).

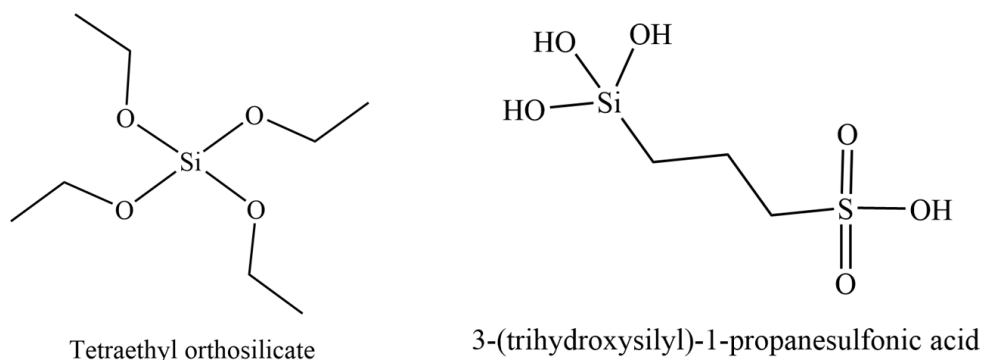


**Figure 1.6** Structural comparison of the unsulfonated and sulfonated organosilane precursors.

Eastcott *et al*, reported that the addition of a small amount of the TPS to the TEOS (5:95 ratios) greatly enhanced the proton conductivity of the electrode.<sup>[50]</sup> The organosilanes were added dropwise to the Pt/C matrix and polymerized to form a gel. The *in situ* polymerization further enhanced the catalytic and mechanical stability of the electrode by initiating chemical bonding between the organosilanes and the surface hydroxyl groups on the carbon support.<sup>[38]</sup> Moreover, they found out that the SS-CCE does not only show enhanced proton conductivity, but they were able to maintain a stable fuel cell performance from 100 to 20% relative humidity (RH) due to their hygroscopic nature.<sup>[38]</sup>

While these sulfonated silica ceramic carbon electrodes can retain water in dry operating conditions, their viability in hot conditions in an operating PEM fuel cell is yet

to be proven. This work seeks to understand, in detail, how the SS-CCE could transport/retained water in dry/hot conditions in a PEM fuel cell using various electrochemical measurements.

## **1.4 Electrochemical Techniques**

The diagnosis of the fuel cell electrodes measures its suitability for fuel cell operation and can also provide valuable feedback for optimization of the MEA structure. The following sections describe recent diagnostic tools used for characterizing fuel cell electrodes.

### **1.4.1 Polarization Curves**

Fuel cell testing is a well-established tool used for characterizing the performance of fuel cell's electrodes (both single cell and stacks).<sup>[51]</sup> During fuel cell testing, two voltages can be observed; the open circuit voltage (OCV) and the working voltage. OCV is the value measured during fuel cell testing when no net current passes through the external circuit. At 0 Amp, the cell achieves an electrochemical equilibrium. In this case, the cell voltage is the difference in thermodynamic voltage between the cathode and the anode, which are associated with the Gibbs free energy  $\Delta G = -nFE^\circ$ .<sup>[52]</sup> The standard thermodynamic cell voltage for a PEM fuel cell is 1.23 V. However, in practice the measured OCV is always lower than 1.23 V. This is mainly due to molecular hydrogen cross over from the anode to the cathode compartment. Sometimes, impurities (organics and oxides) within the catalyst layers can decrease OCV. The working potential seems to be more useful in fuel cell testing, where the fuel cell is under load with power being produced. As a result, the working voltage becomes lower than the OCV and it continues to decrease with increasing current density. The relationship between a working voltage (cell voltage) and current

density is expressed as the polarization curve. Good fuel cell performance display a polarization curve with high current density at high cell voltage giving a high power output.<sup>[51]</sup> The power density can be calculated by multiplying the cell voltage by its corresponding current density value at each point of the curve.

The polarization curve also gives information about the performance losses in the fuel cell under operating conditions. In addition, it can be used to measure the dependent of fuel cell performance on certain parameters such as electrode composition, cell temperature, relative humidity, backpressure, flow rates of reactants and stoichiometrics.<sup>[51]</sup> Figure 1.7 displays a typical fuel cell polarization curve showing the various losses over the current range. These losses include the activation, ohmic and mass transport in the lower, mid- and high current densities, respectively.

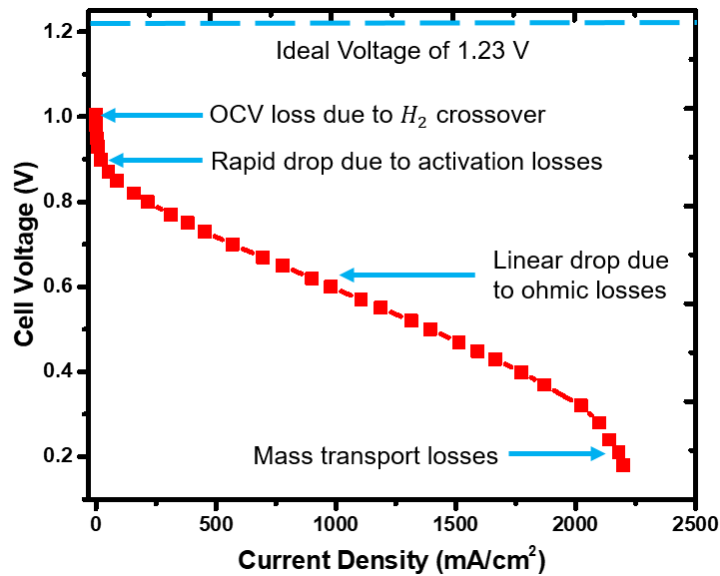


**Figure 1.7** Typical polarization curve of PEM fuel cell



In the low current density region, the working voltage drops drastically due to charge-transfer kinetics which, are the oxygen reduction and hydrogen oxidation rates at the electrode surface.<sup>[52]</sup> These losses depend on the ORR because of its slow kinetics. In the mid-current densities range, the losses are caused by internal resistances, which are the electric contact resistance among the fuel cell components and the proton resistance of the PEM.<sup>[52]</sup> These losses become significant with poor hydration of the MEA. This region also presents a working potential that is linearly dependent on the current density.

In the high current density range, the dominate loss is by mass transport. This occurs when the rate of reactant (i.e., oxygen) and product water are slower than the rate of reaction.<sup>[51]</sup> The water tends to fill the pores of the gas diffusion electrode thereby causing flooding in the system. As a result, the working voltage drops drastically causing poor fuel cell performance.

#### **1.4.2 Cyclic voltammetry**

Cyclic voltammetry (CV) is a well-established technique for extracting qualitative and quantitative information about the electrochemical processes occurring at the electrode/electrolyte surfaces. These processes include electrochemical kinetics, the reversibility of the reaction, reaction mechanisms, and electrocatalytic processes.<sup>[34]</sup> For the case of fuel cell, the *in situ* CV technique has not only been used to measure the electrochemical surface area (ECSA) of the GDE but also it has proven to be quite an effective technique for investigating the molecular hydrogen crossover in the fuel cell device.<sup>[53]</sup>

In a fuel cell configuration, CV experiments are performed using hydrogen gas at the anode side of the MEA as both the counter electrode (CE) and reference electrode (RE).

The cathode side of the MEA is bathed with nitrogen gas and serves as the working electrode (WE). In this configuration, the surface of the WE is explored for faradaic/non-faradaic processes occurring at the electrode/electrolyte interface. The potential of the electrode is scanned with a triangular waveform at a constant rate between two potential limits (upper and lower limits) and at the same time, recording the current passing through the working electrode and counter electrode.<sup>[34]</sup>

A typical fuel cell CV plot using a platinum catalyst is illustrated in Figure 1.8. The figure shows a total of six peaks. The upward peaks represent the oxidation of the active species on the electrode while the downward peaks represent reduction of species.

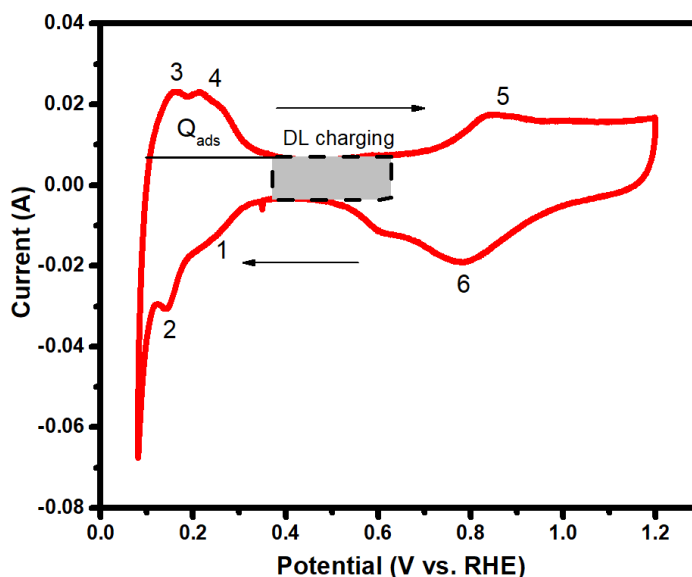
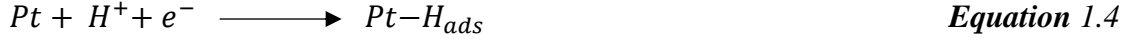
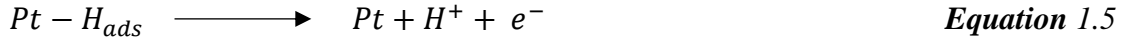


**Figure 1.8** Cyclic voltammogram of a Pt electrode in a PEM fuel cell. Arrows showed the forward and reverse directions. The numbers showed various electron reaction involving dissolved species.

The deposition process<sup>[54]</sup> begins in the region of peaks 1 and 2 where molecular hydrogen is adsorbed on the crystal surfaces of platinum (i.e., Pt(100) and Pt(111)). It can be expressed as follows:

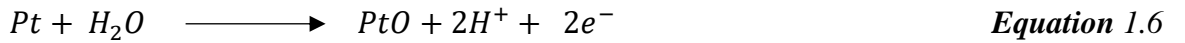


After a potential reversal at 0.08 V, the adsorbed hydrogen ( $H_{ads}$ ) reoxidizes on the platinum crystal surfaces giving peaks 3 and 4. This  $H_2$  desorption reaction can be expressed as follows:

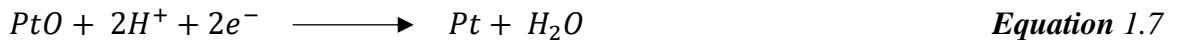


Noticeably, in a small region between 0.4 V and 0.7 V as the scan goes positive potentials, the platinum electrode behaves as a polarized electrode with a small current that is purely capacitive.<sup>[54]</sup> This region is also known as double-layer capacitance region.

Peak 5, at a more positive region, corresponds to the oxidation of the Pt surface to form PtO, which can be expressed with the following reaction:



When the potential reaches its maximum (1.20 V), the scan reverses where a cathodic peak 6 slowly builds at a potential of about 0.6 V. This huge peak response represents the reduction of surface PtO to release the Pt surface. This process can be expressed as the following reaction:



The shape and size of the peaks presented in the voltammogram gives information about the relative kinetic rates and diffusion coefficients of the dissolved species.<sup>[55]</sup> The near-

mirror image relationship that exists between the hydrogen adsorption and desorption peaks 1, 2, 3 and 4 suggests that  $H_{ads}/H^+(aq)$  redox couple are reversible. Contrarily, Pt/PtO peaks 5 and 6 at the more positive region show an irreversibility behavior.<sup>[54]</sup>

The platinum ECSA of the electrode gives information of the catalyst particles available in the reaction medium.<sup>[55]</sup> From the voltammogram, the ECSA of the electrode is determined from hydrogen adsorption charge ( $Q_{ads}$ ) and the Coulombic charge density ( $210 \mu cm^{-2}$ ), assuming a monolayer of hydrogen was adsorbed on a clean polycrystalline platinum surface that is given by the following equation:

$$\text{Pt ECSA (m}^2\text{PtgPt}^{-1}\text{)} = \frac{Q_{ads}}{210L_{Pt}A_{geo}} \times 10^5 \quad \text{Equation 1.8}$$

where  $L_{Pt}$  is the platinum loading of the electrode ( $mg_{Pt} cm^{-2}$ ) and  $A_{geo}$  is the geometric active area of the electrode ( $cm^2$ ). The total charge for the hydrogen adsorption is determined by integrating the area under the hydrogen desorption peaks ( $Q_{des}$ ), where a straight line is drawn from the double layer capacitance region (i.e., 0.450 V) to the final minimum voltage (0.08 V) as shown in Figure 1.8. A correction of the background charging is done by subtracting the current observed at the double layer region from the total current.

### 1.4.3 Electrochemical Impedance Spectroscopy

Electrochemical impedance spectroscopy (EIS) has become an interesting diagnostic tool in the field of fuel cell technology for measuring polarization losses in a short period of time.<sup>[49,56–60]</sup> In contrast to CV, which measures current and electrode potential as a function of time, EIS experiments measure signals at a constant potential as a function of

frequency.<sup>[60]</sup> Primarily, impedance is the measure of the ability of an electrochemical system to resist the flow of electrical current. Such studies were focused on the cathode catalyst layer, which is considered as the most critical component of the PEM fuel cell. The EIS technique perturbs a system by applying a small AC voltage signal (< 20 mV) at a potential known as the DC bias from an initial frequency to a final frequency (in most cases from 100 kHz to 0.1 Hz), where the resulting signals are measured as function of frequency. To understand the impedance of electrochemical device, it is important to have a good grasp of simple electrical circuits. The electrical circuit is usually made up of three passive elements, which include resistors, capacitors and inductors.<sup>[60]</sup> The behaviour of the resistance is different from that of the capacitance and inductance. The Ohm's law relates to the resistance in the circuit through Equation 1.9.

$$V = IR \quad \text{Equation 1.9}$$

where  $I$ , in Amps (A) represents the current passing through resistance, with voltage  $V$ , in volts (V), and resistance  $R$ , in Ohm ( $\Omega$ ).

Under the alternating current (AC) conditions, conductance and inductance can impede the flow of electrons and for this reason the impedance,  $Z$  can relate the voltage and current by the following:

$$V = IZ \quad \text{Equation 1.10}$$

The AC component (i.e, sinusoidal voltage wave) must be considered by the following:

$$V(t) = V_m \sin(\omega t + \theta) \quad \text{Equation 1.11}$$

where  $V(t)$  is the instantaneous voltage value at an instant of time  $t$ ,  $V_m$  is the peak amplitude of the sinusoidal voltage wave ( $V$ ),  $\theta$  is the phase angle,  $\omega$  is the angular frequency (rad/s), and  $t$  is the time (s).<sup>[52]</sup> The angular frequency  $\omega$  can be expressed as  $2\pi f$ , since the angle spun in one revolution is  $2\pi$  radians. Therefore, Equation 1.11 can be rewritten as:

$$V(t) = V_m \sin(2\pi ft + \theta) \quad \text{Equation 1.12}$$

In the same way the sinusoidal current wave can be expressed as the following:

$$I(t) = I_m \sin(2\pi ft + \phi) \quad \text{Equation 1.13}$$

where  $I(t)$  is the instantaneous current value at an instant of time  $t$ ;  $I_m$  is the amplitude or the maximum value of the sinusoidal current wave (A);  $\phi$  is the phase angle;  $f$  is the frequency (Hz); and  $t$  is the time (s).<sup>[52]</sup> The electrical resistance associated with an AC circuit is known as AC impedance. Considering the definition of resistance by Ohm's law, the relationship between the current-voltage in impedance can be expressed as follows:

$$Z = \frac{V(t)}{I(t)} \quad \text{Equation 1.14}$$

where  $V(t)$  and  $I(t)$  are the voltage and current measured in an AC system. For a sinusoidal system, the phase angle of a resistor is equal to zero and thus the AC impedance of a resistor is given by Equation 1.15:

$$Z_R = R \quad \text{Equation 1.15}$$

On the other hand, the AC impedance of a capacitor,  $Z_C$  can be expressed as:

$$Z_C = \frac{1}{i\omega C} \quad \text{Equation 1.16}$$

where,  $i$  is an imaginary number given as  $i = \sqrt{-1}$ . The overall impedance of the system is contributed by the AC impedance of the resistor and capacitor, which are in parallel. This can be denoted by the following expression;

$$Z_{R/C} = \frac{1}{Z_R} + \frac{1}{Z_C} \quad \text{Equation 1.17}$$

where  $Z_R$  and  $Z_C$  contribute to the real and imaginary parts of the impedance respectively.

Therefore, the equation can be rewritten as;

$$Z_{total} = Z' + Z'' \quad \text{Equation 1.18}$$

where  $Z'$  are the real components and  $Z''$  are the imaginary components of the impedance measured in ohms.

To gain insight into the MEA using EIS, the electrode-electrolyte interface can be represented by an equivalent circuit transmission line model. The equivalent circuit contains circuit elements representing impedance response contributed by various MEA components. Pickup *et al* have constructed a finite transmission line equivalent circuit, shown in Figure 1.9, which is widely used to model porous electrodes and PEM fuel cell electrodes.<sup>[57,58,61,62]</sup>

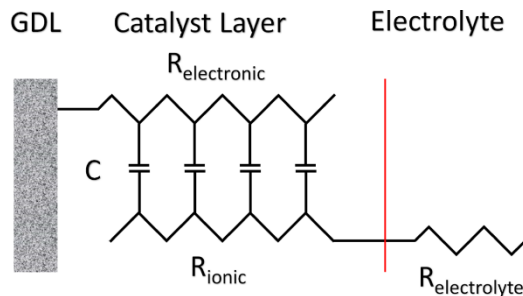


**Figure 1.9** Transmission Line Model for impedance spectroscopy of porous electrode.

The model is composed of two parallel resistive rails; one representing the electron transport through conducting Pt/C particles ( $R_{electronic}$ ) and the other rail for ion transport in the catalyst layer ( $R_{ionic}$ ).<sup>[57,61]</sup> As depicted by the model, the two rails connected by capacitors, assumed that capacitance is uniformly distributed throughout the catalyst layer.<sup>[57,61]</sup> Another assumption made was that  $R_{electronic}$  is negligible compared to  $R_{ionic}$ , because of the high electronic conductivity of carbon particles. For this reason, the impedance due to electron transfer is significantly small and can be ignored.<sup>[57,61]</sup> Therefore, the total catalyst layer resistance,  $R_{\Sigma}$  is often assumed to be equal to the ionic resistance (*i. e.*  $R_{\Sigma} = R_{ionic}$ ). In addition, the membrane resistance ( $R_{membrane}$ ) is omitted simply because it would only shift the plot along the real axis.<sup>[57,61]</sup> Considering these assumptions, the impedance response of the PEM fuel cell electrode can be modeled for any ionic conductivity profile.<sup>[57,61]</sup> Moreover, the use of H<sub>2</sub>/N<sub>2</sub> gas feeding configuration simplifies the model such that the anode charge-transfer becomes negligible while the cathode charge-transfer is infinite, which could be useful for elucidating the total ionic resistance associated with the electrode at high frequencies (100 kHz – 1000 Hz).<sup>[52]</sup>

Figure 1.10 shows an impedance spectrum of a PEM fuel cell under H<sub>2</sub>/N<sub>2</sub>, represented by the Nyquist (a), capacitance (b) and normalised (c) plot. The Nyquist plot ( $Z''$  vs  $Z'$ ) exhibits a Warburg-like response at the mid-to-high frequency region which corresponds to the ion migration through the catalyst layer. The length of the Warburg region before it curves upward can be projected onto the real impedance axis to give the total ionic resistance ( $R_{\Sigma}/3$ ) of the electrode.<sup>[61]</sup> This is determined by the intersection of the two slopes as shown in Figure 1.10.a.



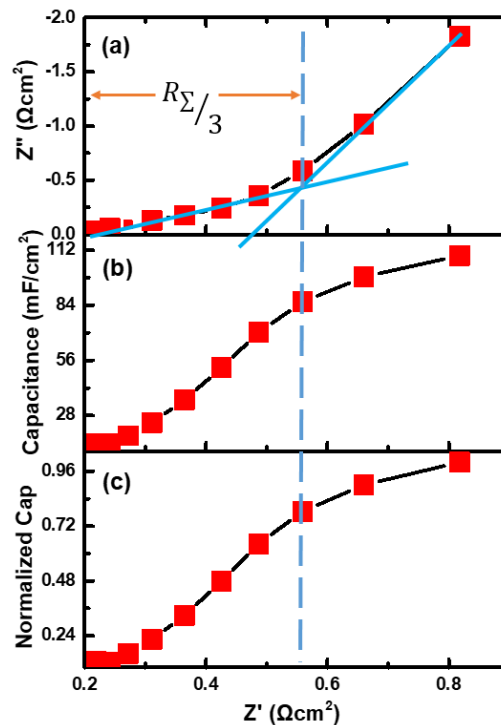


**Figure 1.10** EIS response of PEM fuel cell under  $\text{H}_2/\text{N}_2$  at 30 °C represented by (a) Nyquist (b) Capacitance and (c) Normalized capacitance plot.

Generally, the Warburg region can be related to the capacitance plot ( $C$  vs  $Z'$ ) as shown in Figure 1.10.b. The capacitance ( $C = -1/\omega Z''$ ) represents the effectiveness of electron and proton transport to the catalyst site. This is measured by the height of the capacitance slopes before it plateaus at a limiting point. This represents the total capacitance and resistance of the catalyst layer. Finally, the capacitance plot can be normalized to a limiting capacitance (as shown in Figure 1.10.c), to enable a qualitative comparison of the ionic conductivity for different catalyst compositions and operating conditions.<sup>[57]</sup>

## 1.5 Objectives

The objective of this study is to investigate the properties of sulfonated-silica ceramic carbon electrode (SS-CCE), specifically the impact they have on the PEM fuel cell performance under more extreme conditions such as high temperatures and low relative humidities, because water plays key role in the conductivity of fuel cell electrodes. I explored the use of electrochemical tools such as fuel cell testing, cyclic voltammetry and electrochemical impedance spectroscopy to address the following questions:

1. How will the cell temperature between 70°C and 95 °C influence the performance of SS-CCE?
2. How will the cathode relative humidities influence the performance of SS-CCE?
3. What impact does the symmetric/asymmetrical MEA configuration have on the cell performance?
4. How durable are SS-CCE at these conditions after tests?

In the addition, benchmark data will be collected using commercial material (i.e., NBE) prepared in the Lab. The test results of the commercial material will be compared with the SS-CCE based MEA performances under various operating conditions.

## **Chapter 2 Materials and Methods**

## **2.1 Chemicals and Materials**

Isopropanol, IPA 99.50% purity (Fisher scientific), sulfuric acid 95 – 98% purity (ACP Chemicals), hydrogen peroxide 30% (EMD Millipore Corporation), tetraethyl orthosilicate, TEOS 98% purity (Aldrich), 3-(trihydroxysilyl)-1-propane sulfonic acid, TPS 30 – 35% in water (Gelest, Inc.), 5 wt% Nafion (DuPont), 6 M ammonium hydroxide was prepared and refrigerated, 20% Pt on Vulcan XC-72 (Premetek), Sigracet 29 BC gas diffusion layer (Fuel cell store), Nafion membrane NRE212 (Ion-power). Compressed gases including H<sub>2</sub> (99.999%), N<sub>2</sub> (99.998%), O<sub>2</sub> (HFC grade), air (extra dry) were purchased from Praxair.

## **2.2 Catalyst Ink Preparation**

### **2.2.1 Nafion-based catalyst ink**

Based on theoretical calculation of Pt and Nafion loading targets, the required mass of a commercial Platinum supported on carbon catalyst (20% Pt on Vulcan XC-72, Premetek) was weighed into a clean dry beaker. Deionized (DI) water was added prior to the addition of isopropanol (IPA) to avoid ignition of the catalyst powder. Volumes of isopropanol and deionized water added were in amounts of 1:3 ratios respectively. While stirring a required volume of 5wt% Nafion solution was slowly added to the mixture. The catalyst mixture was stirred for 2 h and placed under sonication for 1 h to obtain a good blend of the Nafion and catalyst. Afterwards, it was left to stir overnight to acquire a homogeneous suspension of catalyst ink.

### **2.2.2 Sulfonated silica ceramic carbon electrode catalyst ink**

SS-CCE catalyst ink was prepared by dispersing a required mass of a commercial Pt/C catalyst (20% Pt on Vulcan XC-72, Premetek) in DI water followed by the addition

of isopropanol and 6 M  $\text{NH}_4\text{OH}$  solution to adjust the pH of the catalyst to 8 – 9. Volume of the TEOS and TPS solution in a 95:5 ratio was added slowly to the mixture in drops while being stirred. The catalyst mixture was then stirred for ~ 3 days to polymerize the organosilane monomers. A gel solution of the SS-CCE was achieved after several 3 days of stirring.

## **2.3 Physicochemical Characterization**

### **2.3.1 Thermal Gravimetric Analysis**

Thermogravimetric analysis (TGA) was carried out using TA instruments Q600 SDT thermal analyzer. A dried catalyst sample weighing ca. 6 – 10 mg was loaded into alumina pans and heated from room temperature up to 1000 °C at a ramp of 20 °C/min under air at a flow rate of 50 mL/min. The mass of the sample was monitored as a function with temperature. Thermograms were used to determine the weight percent of individual components present in the catalyst material and their thermal stability.

### **2.3.2 Brunauer-Emmett-Teller Surface Area and Barrett-Joyner-Halenda Pore Size analysis**

The surface area and the pore size distribution of the electrode material was measured using a Quantochrome NOVA 1200e Surface Area and Pore Size Analyzer using nitrogen physisorption method. The sample was loaded into a physisorption tube and placed in the degassing chamber. The catalyst sample was slowly heated to 200 °C and held at this temperature for about 6 h under vacuum. This was done to remove contaminants from the catalyst sample. After degassing, the sample was weighed and transferred into the adsorption chamber of the Brunauer-Emmett-Teller (BET) instrument where catalyst

sample was cooled in liquid nitrogen. Nitrogen adsorption-desorption isotherms were recorded and analyzed using the NovaWin Software.

### **2.3.3 X-Ray Diffraction**

X-ray diffraction (XRD) measurements were conducted to investigate the crystalline size of a catalyst sample. XRD patterns were obtained using a Rigaku Ultima IV X-ray diffractometer that employs Cu K $\alpha$  radiation ( $\lambda = 0.15418$  nm). Patterns were acquired over a  $2\theta$  range of  $10 - 100^\circ$  using a step size of  $0.02^\circ$ . XRD pattern presents a plot of the intensity of X-rays scattered at different angles by the sample. Data analysis was done using PDXL integrated X-ray powder diffraction software by Rigaku. Peak shapes and widths presented in the pattern were used to determined crystalline size of the catalyst sample.

### **2.3.4 Scanning Electron Microscopy/ Energy Dispersive X-ray Analysis**

The morphology (e.g. surface features) and structure (e.g. porosity) of the catalyst layer were investigated using a HITACHI Flex SEM 1000 Scanning Electron Microscope (SEM). About  $1\text{ cm}^2$  of the catalyst layer was cut with a fresh razor blade and placed on a standard SEM stub with a conductive carbon tape. SEM images were measured with an accelerating voltage of 10 kV and various magnifications at different sample sites. The thickness of the MEA before and after test were verified by a cross-section technique using the SEM.

Energy dispersive X-ray (EDX) analysis was employed to investigate the elemental compositions of various electrodes. EDX spectra were acquired using a HITACHI Flex SEM 1000 SEM equipped with an energy dispersive spectrometer.

## 2.4 Electrochemical Evaluation

### 2.4.1 Fuel Cell System

#### 2.4.1.1 Gas Diffusion Electrode Fabrication

Sigracet 29 BC was the GDL for all electrodes tested. The GDL can be subdivided into carbon paper and microporous layer (MPL). The MPL is made up of high surface area carbon black (Vulcan XC-72) and PTFE, which provides good support for the CL and at same time helps minimizes contact resistances between the GDL/CL. The GDE is basically prepared by spray depositing the catalyst ink onto the GDL using an air spray gun as shown in Figure 2.1. The same spraying procedure was used for both Nafion and SS-CCE catalyst inks to prepare a NBE and a SS-CCE. Platinum loading target for both NBE and SS-CCE electrodes was  $0.20 \text{ mg/cm}^2$ . The target Nafion and silicate loadings for this work were 30% and 40% respectively.

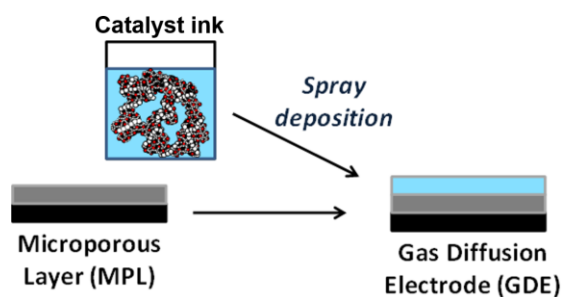


**Figure 2.1** Fabrication process of gas diffusion electrode

### **2.4.1.2 Membrane Electrode Assembly Fabrication**

#### **2.4.1.2.1 Membrane activation**

Before assembling the electrodes, the solid electrolyte (Nafion NRE212) was activated to improve its proton conductivity. The activation was done following a stepwise procedure;

- a. Nafion NRE 212 was cut into the required sizes and were washed and boiled in DI water for an hour.
- b. Membranes were soaked in hot (ca. 80°C) 3% H<sub>2</sub>O<sub>2</sub> for 1 h.
- c. Membranes were rinsed with boiling DI water for 20 min.
- d. The membranes were then immersed in hot 0.5 M H<sub>2</sub>SO<sub>4</sub> for an hour to remove metallic impurities.
- e. Lastly, the membranes were rinsed in boiled DI water for 2 h to remove traces of acids.

N.B: DI water for the last step was changed every 20 min.

#### **2.4.1.2.2 MEA hot-pressing**

An activated Nafion membrane was sandwiched between two 5 cm<sup>2</sup> GDEs and placed between two aluminum platens wrapped with aluminum foil. The assembly was inserted into a hydraulic press with hot plates set at 100 °C and then pressed to 39 kPa for 3 min. The assembly was removed from the press and allowed to cool to room temperature before taking out the MEA. Table 2.1 shows the three types of MEA configurations investigated.



**Table 2.1 Description of the MEAs tested in this study**

MEA	Anode catalyst layer (0.2 mg cm <sup>-2</sup> )	Membrane	Cathode catalyst layer (0.2 mg cm <sup>-2</sup> )
Symmetric NBE	NBE	NRE212	NBE
Symmetric SS-CCE	SS-CCE	NRE212	SS-CCE
Asymmetric SS-CCE	NBE	NRE212	SS-CCE

#### **2.4.1.3 Single fuel cell test fixture and assembly**

The MEA were tested inside a 5 cm<sup>2</sup> cell made by Nuvant (test fixture). The Nuvant cell consists of a pair of Poco graphite blocks with a serpentine flow-field. Parallel flow channels with a cross section area 0.5 mm (width) and 0.5 mm (depth) designed for both the anode and cathode graphite plates. A pair of gold-plated connectors fastened to aluminum end plates were used as current collectors. Gas pipes were connected through Swagelok fittings. A cartridge heater and a thermocouple well are also provided to produce heat and measure temperature in the system. A pair of gaskets made of a Teflon were used as sealing material.

Figure 2.2 shows an expanded view and the assembled of the Nuvant cell. The bolts were initially tightened by hand to secure the position of the MEA and gaskets assembly in the test fixture. The test fixture was then torqued at 5.65 Nm using a torque wrench for a proper sealing and a good electronic contact between the graphite plates and MEA. The PEM fuel cell was mounted no the test stand (fuel cell station) where all the test leads

(i.e, anode and cathode vents, anode and cathode load sensor and thermocouple) were connected.

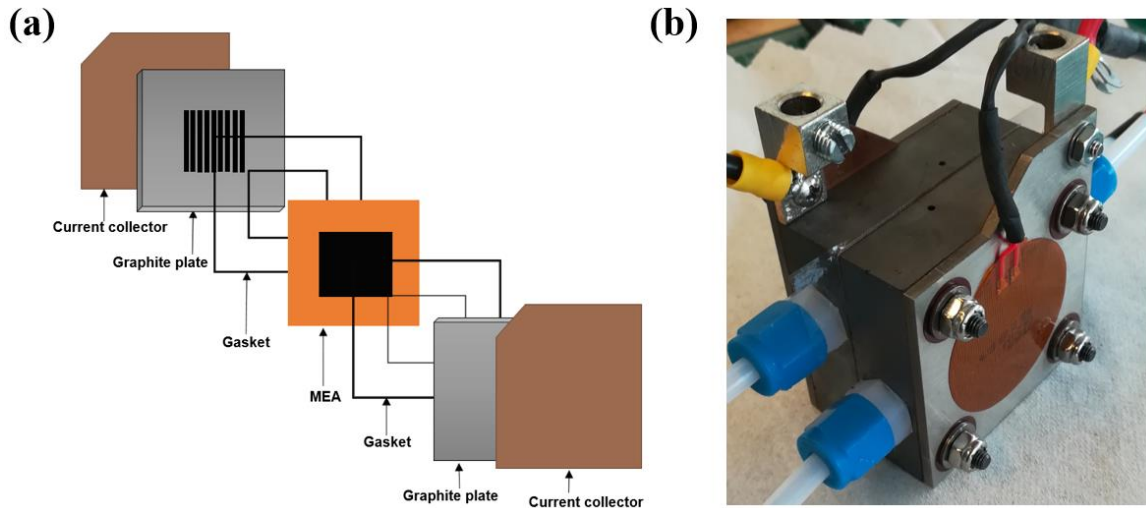


**Figure 2.2** (a) Expanded view of the Nuvant cell and (b) an assembled Nuvant cell

#### 2.4.1.4 Fuel Cell Test Station

Figure 2.3 shows a fuel cell test station purchased from the Fuel Cell Technologies, Inc. This device is specifically designed for testing a single cell under an actual fuel cell operating condition. Basically, it consists of a DC electronic load, two humidity bottles and a computer utilizing LabVIEW-based software. The software is designed for controlling operational parameters such as temperature, gas flow, humidity temperature and gas line heater temperature. The software is also used to collect and plot data for the I-V curves.

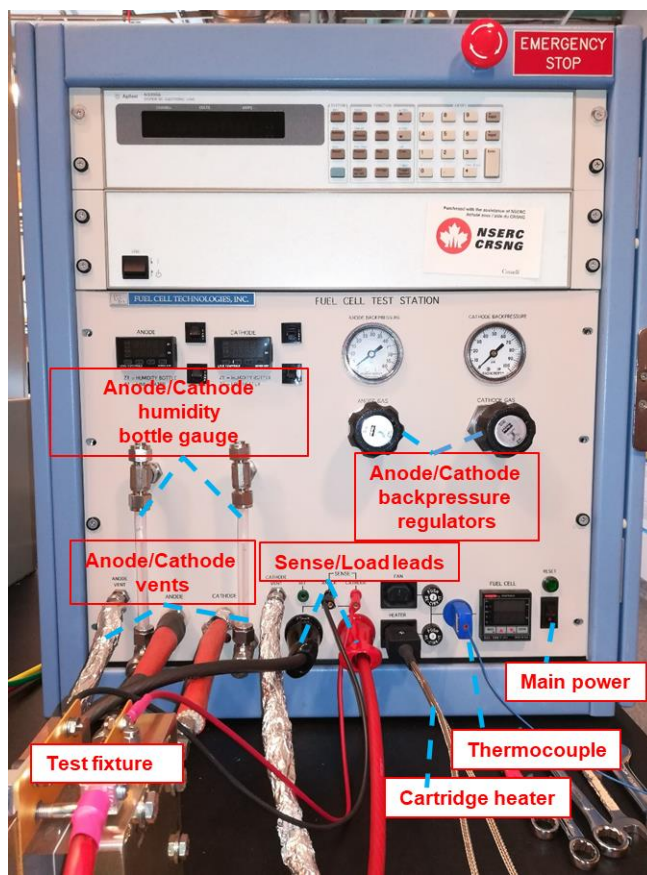


**Figure 2.3** A Commercial Fuel Cell Test Station

#### 2.4.1.5 MEA Activation (“Break-In”)

Prior to the electrochemical evaluation, the MEA was subject to a “break-in” process under  $H_2/O_2$  for about 6 h at 50 °C. This process increases the catalyst utilization by establishing transfer channels for electrons, protons and oxygen in the catalyst layer.<sup>[63]</sup> The cell, operating at 50 °C, was held at 0.6 V for an hour followed by 6 cycles alternating between 0.40 V and 0.60 V with each cycle held for 20 min.

#### 2.4.2 Polarization Curves

This technique was used to evaluate the performance of the fuel cell. Performance of the fuel cell was monitored by polarization curves (graph of cell voltage vs current

density) and power density curves (product of cell voltage and current density), which would be termed as performance of the cell. A good fuel cell performance must display polarization curves with high current density at high cell voltage given a high peak power. Polarization curves were measured at various cell and gas temperatures under  $H_2/O_2$  and  $H_2$ /air gas feeds. Hydrogen was fed at the anode compartment and oxygen or air was fed at the cathode compartment. The reactant gases fed into the fuel cell were humidified by passing through heated water bottles installed in the fuel cell test station. Therefore, gas temperatures were controlled by the humidifier temperature. In this case, the relative humidity levels of the reactants were monitored by the temperature of the gas humidifiers with respect to the cell temperature.

The fuel cell was fed with reactant gases from pressurized tanks. The pressure from these tanks were controlled by a backpressure regulator placed at the outlet of the test station. The fuel cell was operated at 10 psig (170 kPa) backpressure during all tests. The mass flow rates for the  $H_2$  and  $O_2$  were 100 and 200 mL/min respectively and the air oxidant flow rate was increased to 1000 mL/min.

The current density produced is directly proportional to the reactants consumed.<sup>[64]</sup> In the case of air as the oxidant, the flow rate was increase by a factor of 5 in order to increase the number of moles of the oxygen in the dry air to that of the pure oxygen. LabVIEW software (National Instruments) was used for controlling the cell temperature, reactant flow rate, humidification temperature and load voltage through a computer that has been connected the fuel cell station.

Prior to the polarization test, the cell temperature and the humidification temperatures were held for about two hours to obtain a steady state system. Polarization

curves were recorded from OCV 0.95 V to a final cell voltage 0.25 V using a potentiostatic step. The voltage step size during the measurement was 0.03 V. In all, 29 data sets were recorded for the polarization curve. Seven or more curves were recorded, and the data were averaged to give a precise polarization curve of that condition. A total of 3 MEAs were tested under each operational condition to ensure reproducibility of the results.

### **2.4.3 Cyclic Voltammetry**

CV was performed using a Solartron 1470E multi-channel potentiostat, which was controlled by a Multistat software. After the polarization test,  $H_2$  was kept on the anode and the cathode compartment was flushed with  $N_2$  to remove all oxygen. The load leads were removed from the test stand and the leads from the potentiostat were connected to the test fixture (Nuvant cell). In this case, the anode serves as both the reference (i.e., Reversible Hydrogen Electrode, RHE) and counter electrodes and the cathode as the working electrode. The cathode voltage was scanned from 0.08 V to 1.20 V at a potential scan rate of  $20\text{ mVs}^{-1}$ . A total of 3 scans were collected for analysis. The CVs were measured at various cell temperatures and cathode relative humidities to evaluate their effect on the Pt ECSA.

### **2.4.4 Hydrogen Crossover**

Under the  $H_2/N_2$  gas feed configuration, HOR current was measured. Potential of 0.50 V applied as the current produced was recorded. At this fixed potential, where no faradaic processes take place (i.e., in the DL region), any molecular hydrogen that permeates through the membrane to the cathode compartment will be oxidized yielding a diffusion limited current (i.e., a plateau curve).<sup>[65]</sup> Plot of current against the time was used

to determine the limiting current. The H<sub>2</sub> crossover rate ( $J_{H_2}^{cross}$ , mol cm<sup>-2</sup> s<sup>-1</sup>) was calculated using Equation 2.2.<sup>[65]</sup>

$$J_{H_2}^{cross} = \frac{I_{H_2}^{cross}}{nFA} \quad \textbf{Equation 2.2}$$

where  $I_{H_2}^{cross}$  is the current obtained because of oxidized H<sub>2</sub>,  $n$  is the electron number of H<sub>2</sub> oxidation ( $n = 2$ ),  $F$  is the Faraday constant (96485.3329 A s mol<sup>-1</sup>) and  $A$  is the MEA active area (5 cm<sup>2</sup>)

#### 2.4.5 Electrochemical Impedance Spectroscopy

EIS was measured using a Solartron 1470E multi-channel potentiostat with a Solartron 1260 frequency response analyzer controlled using multistat software (Scribner Associates). Measurements were made immediately after the CVs and hydrogen crossover measurements. A perturbation voltage (5 mV) was applied between a frequency of 100 kHz to 0.1 Hz at a DC bias potential of 0.425 V (vs RHE). EIS measurements were performed at various cell temperatures and relative humidity to investigate how these conditions affects the membrane resistance, ionic resistance and the total capacitance of the electrode. The cell temperature and the RH were controlled by the fuel cell station.

#### 2.4.6 Accelerated stress test of the electrodes

The durability of the SS-CCE and Nafion-based electrodes were determined by a Drive Cycle Test prescribed by DOE/Fuel Cell Technology.<sup>[66]</sup> Briefly, 5000 cyclic voltammetry scans were obtained between 0.08 V and 1.20 V at a scan rate of 200 mV s<sup>-1</sup> under 30 °C cell temperature with H<sub>2</sub>/N<sub>2</sub> gas feed. In addition, EIS test were performed immediately after every 1000 CVs scans. CVs, Nyquist and capacitance plots were

constructed from the collected data to assess the ECSA and the conductivity of the electrode after the accelerated stress test (AST).

In addition, post mortem transmission electron microscopy (TEM) and energy dispersive X-ray (EDX) analysis were conducted to confirm changes in the electrode structure after the durability test. Samples for TEM and EDX tests were collected by carefully scratching the surface of the CL with a sterile scalpel. The samples were sent to the University of McMaster to be analysed. Using the ImageJ software, more than two hundred particle sizes were measured to calculate the mean particle size before and after the AST.

## **Chapter 3 Results and Discussion**



### 3.1 Materials Characterization

#### 3.1.1 Thermogravimetric Analysis

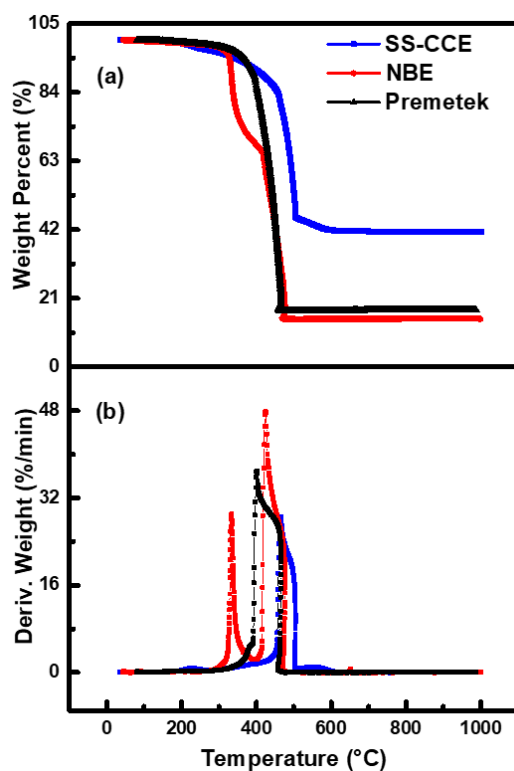
TGA were conducted to assess the composition and the thermal stability of the electrodes. TGA presents the mass loss of a sample as a function of temperature while differential thermal gravimetry (DTG) curve illustrates the point at which weight loss is most apparent. Figure 3.1 shows TGA/DTG curves for the NBE and the SS-CCE compared with the Premetek (commercial catalyst). The TGA/DTG curves were obtained under air flowing at a flow rate of 50 mL/min. Samples were heated from room temperature to 1000 °C with a temperature ramp of 20 °C/min.

Figure 3.1 shows that the NBE initial losses between 25 °C and 200 °C could be due to water and other volatile solvents. The onset decomposition temperature of the Nafion ionomer was observed at 320 °C, followed by the combustion of the carbon to CO<sub>2</sub> at 400 °C leaving a residual solid mass containing only Pt, which occurred at temperature above 480 °C. Based on the residual mass, a back calculation was done to estimate actual masses of individual components including Pt, Nafion, and carbon in the electrode. As a result, the electrode was found to be made of 27.10% Nafion, 17.40% Pt, 53.33% carbon and about 2% was lost to water and other volatile compounds.

In the case of the SS-CCE composite, the onset temperature of the decomposition of sulfonic acid groups occurs at 240 °C, in agreement with previous works on SS-CCE reported in literature.<sup>[38],[24]</sup> This was followed by the combustion of carbon to CO<sub>2</sub> at 500 °C and the last step is a residual mass composed of a silicate and Pt at temperature above 500 °C. The residual mass was used to calculate actual masses of Pt and silicate. It was found that the SS-CCE was made of about 11% of Pt and about 32% silicate.

The silicate is composed of a  $\text{SiO}_2 + \text{SiO}_{1.5}$  network, both from the starting materials TEOS and TPS respectively.

In addition, the onset combustion temperature of carbon was increased for the SS-CCE ( $500^\circ\text{C}$ ) compared to the NBE ( $400^\circ\text{C}$ ). This difference could be due to the incorporation of the silicates into the Pt/C matrixes where the electrode benefits from the mechanical characteristics of the silicate.<sup>[48]</sup> For this reason, the silicate prevents the carbon from further combustion, thereby increasing the thermal stability of the electrode.



**Figure 3.1** TGA/DTG scans in flowing air for the Premetek (commercial catalyst), the NBE and the SS-CCE; temperature was ramped at  $20^\circ\text{C}/\text{min}$  to  $1000^\circ\text{C}$ .

### 3.1.2 BET Surface Area and BJH Pore Size Analysis

BET nitrogen adsorption method was used to determine the surface area of the NBE and SS-CCE catalysts. The gas adsorption method allows the measurement of the size and volume distribution of micropores ( $\leq 2.0$  nm). Figure 3.2 shows isotherms (volume of nitrogen per gram of material at standard temperature vs relative pressure,  $P/P^\circ$ ) for the NBE and SS-CCE catalysts.

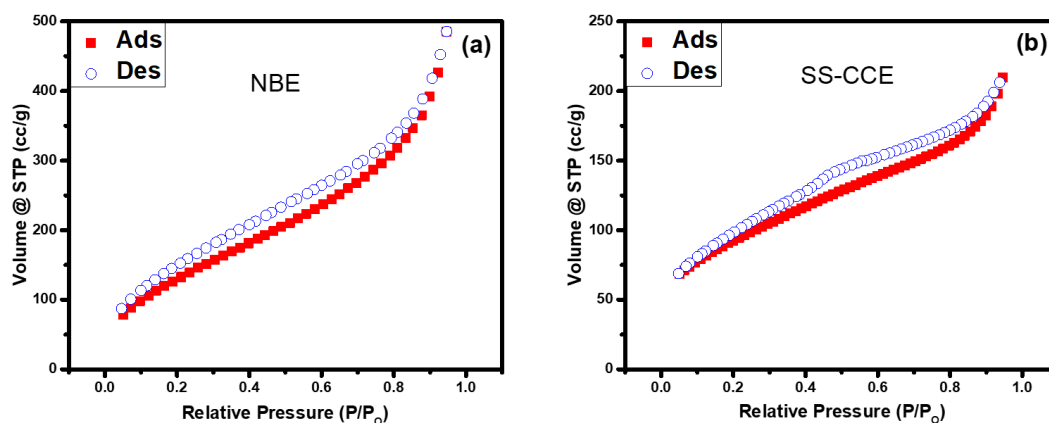


**Figure 3.2** Volume of nitrogen plotted as a function of relative pressure as measured during BET surface analysis of (a) NBE and (b) SS-CCE catalyst.

Table 3.1 is a summary of specific surface area and pore sizes of each electrode material. From the data shown in Figure 3.2 and Table 3.1, the instrument reported surface areas of  $227 \text{ m}^2\text{g}^{-1}$  for the NBE and  $264 \text{ m}^2\text{g}^{-1}$  for the SS-CCE catalyst. In addition, the average pore sizes for the NBE and SS-CCE were 1.54 nm and 1.10 nm respectively. These results indicate that the SS-CCE catalyst is more porous material compared to the NBE catalyst.

**Table 3.1 BET summary of the NBE and SS-CCE catalyst**

Properties	NBE	SS-CCE
Pore radius (nm)	1.54	1.10
Micropore volume (cm <sup>3</sup> g <sup>-1</sup> )	0.607	0.258
BET surface area (m <sup>2</sup> g <sup>-1</sup> )	227	264

### 3.1.3 X-Ray Diffraction

XRD was performed for structure and phase analysis of the catalyst samples. Figure 3.3 shows the XRD patterns for the commercial catalyst (20% Pt on Vulcan XC-72) and the SS-CCE catalyst.

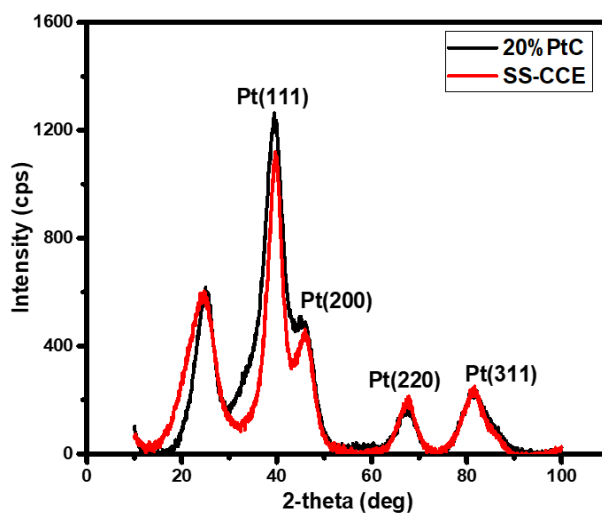


**Figure 3.3** XRD patterns of 20% Pt on Vulcan XC-72 (Premetek) and SS-CCE catalysts.

These patterns were overlaid on each other for comparison. The broad peak centered at ca. 26.2° is carbon (002) whereas peaks at ca. 40°, 47°, 68° and 82° are due to Pt (111),

Pt (200), Pt (220) and Pt (311) face-centered cubic faces respectively.<sup>[3-5]</sup> From the SS-CCE pattern, no peaks were observed for silica, which indicates that the silicate is amorphous. The small difference in peaks of Pt (111) and Pt (200) related to the SS-CCE, suggests small particle sizes of the SS-CCE composite. It can also be seen that peak at ca. 26° was broad for the SS-CCE, indicating the presence of silicate on the carbon surface. However, peaks presented by the SS-CCE were sharper than that shown by the commercial catalyst, suggesting an increased in crystallinity of the SS-CCE composite.<sup>[11,23]</sup> Therefore the XRD data have confirmed that TEOS and TPS were successfully deposited into the Pt/C matrix.

### 3.1.4 Transmission electron microscopy measurements

The morphology of the electrodes was investigated using a TEM. Figure 3.4 shows the TEM images of the received Pt/C (Premetek) compared with the NBE and the SS-CCE catalyst. The TEM images show a fine and uniform, dispersed black and gray spots which represents the absorption of electrons by the platinum and carbon particles respectively as confirmed by the TEM instrument.

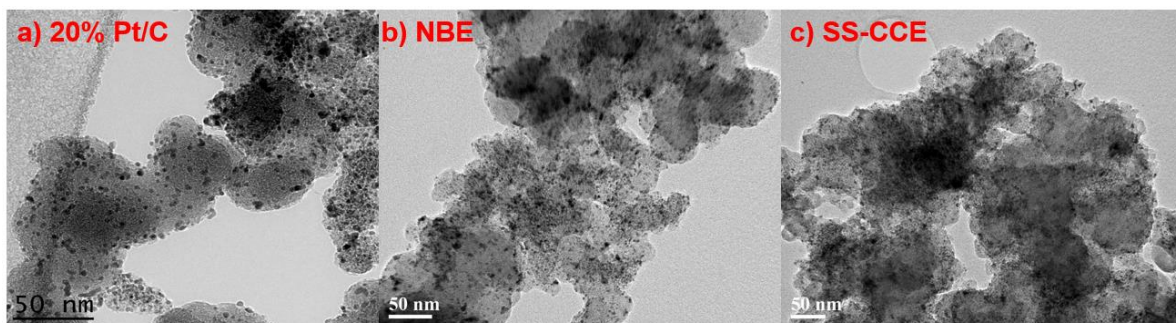


**Figure 3.4** TEM images of a (a) 20% Pt/C, Premetek, (b) NBE and (c) SS-CCE catalyst layers

The TEM images related to the NBE and the SS-CCE catalysts show a slight agglomeration due to the amorphous nature of the respective ionomers incorporated Pt/C matrix. This observation was more obvious in Figure 3.4.c (SS-CCE), which indicates that silicates are highly amorphous. This was consistent with the XRD measurements. The average particle size of Pt was ca. 2 – 3 nm, consistent with the specifications provided by the supplier.

### 3.1.5 Scanning electron microscopy measurements

The microstructure analysis of the SS-CCE catalyst layer was performed by SEM. Figure 3.5 shows SEM images with different magnifications. It can be seen that particles are well connected, which indicates that silicate was uniformly dispersed in the Pt/C matrix. The microscopic surface of the layer was seen to be covered with small pores, which could enhance water removal and reactants mass transport. This could lead to better fuel cell performance.

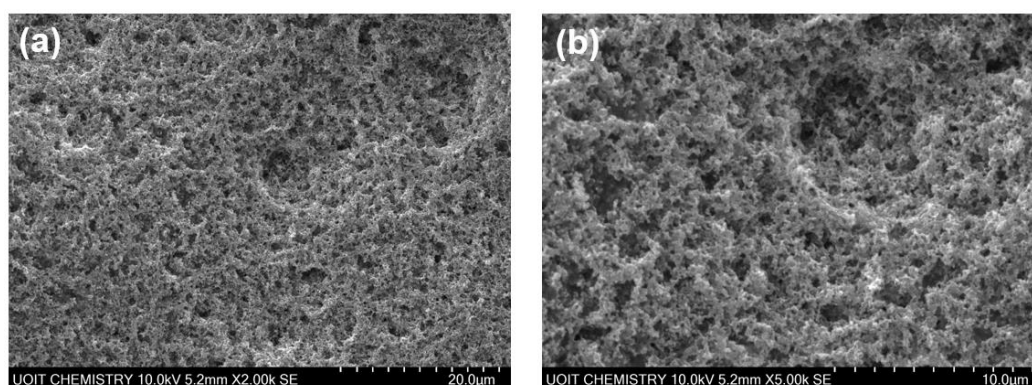


**Figure 3.5** SEM image of SS-CCE of (a) 2.00k (b) 5.00k magnifications.

### 3.1.6 Energy dispersive X-ray analysis

EDX analysis was performed on the SS-CCE gas diffusion electrode to determine the elemental composition of the electrode. The EDX spectrum of the SS-CCE GDE is shown in Figure 3.6.a. The spectrum shows peaks of a Si and S along with the Pt and C peaks. The peaks due to the Si and S originated from the starting materials TEOS and TPS monomers respectively. This confirms the presence of silicates in the catalyst. The weak peak of Al observed in the spectrum is due to the aluminum sample holder used as the SEM stub. Figure 3.6.b shows the elemental mapping on the surface of the SS-CCE GDE. The mapping result shows a thorough mixture of individual elements, more importantly the uniform dispersion of the Si.

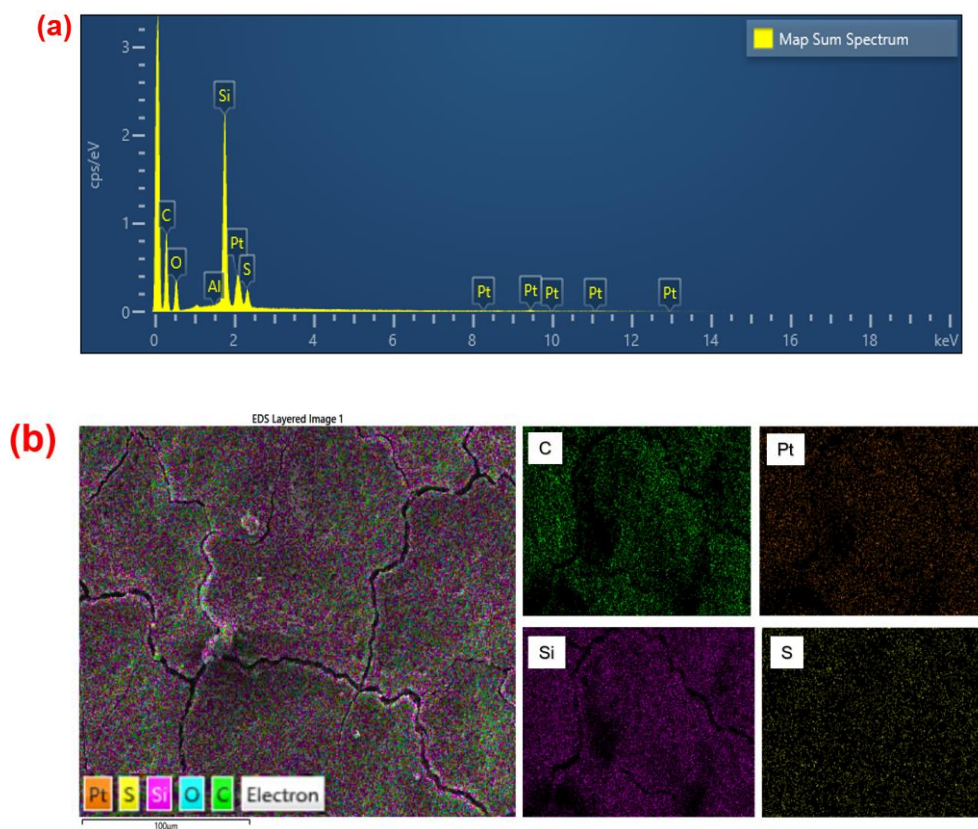


**Figure 3.6** (a) EDX spectrum of SS-CCE and (b) elemental mapping of SS-CCE catalyst layer.

The thickness of the catalyst layer sprayed on the GDL was measured using SEM and EDS techniques. Figure 3.7 presents a cross-section SEM image and EDS mapping of the SS-CCE GDE respectively. The EDS mapping confirms that the top layer of the GDE is the thin film catalyst, showing a uniform mixture of Si and Pt. The thickness was measured at six different places along the area shown as catalyst layer using ImageJ software. The average thickness was found to be 7.5  $\mu\text{m}$ . The thickness of the SS-CCE GDE is within the appropriate thickness of a commercial GDE reported in literature.<sup>[67]</sup> However, the traces of catalyst found in the circled area was due to the fragments of the catalyst transferred during cutting.

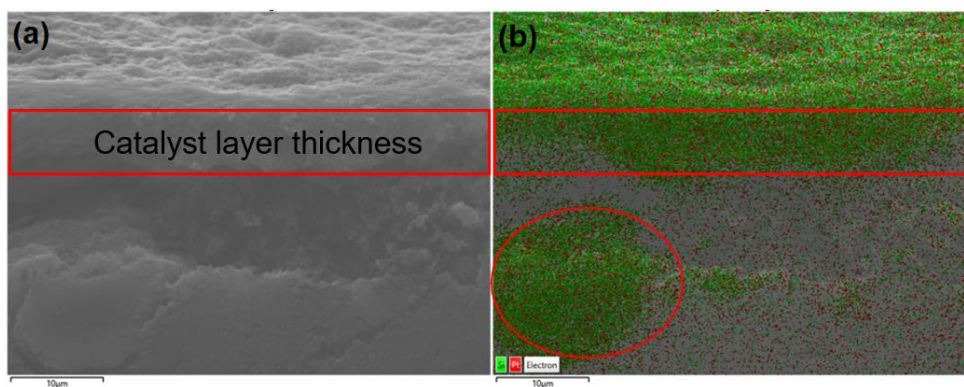


**Figure 3.7** Cross-sectional SEM images (a) and EDS mapping (b) of the SS-CCE



## **3.2 Electrochemical evaluation of the NBE**

### **3.2.1 Fuel cell testing**

#### **3.2.1.1 The effect of cathode relative humidity on the NBE MEA**

The influence of cathode relative humidity (RH) on the PEM fuel cell performance was determined by fuel cell testing where the anode was kept at constant 100% RH and the cathode was varied between 40% – 100% RH. Cathode gas RH was varied because it has been found that cell performance is mostly affected by the humidification at the cathode side.<sup>[68]</sup> This test was conducted at various operating cell temperature ranging from 70 °C to 85 °C. The hydrogen and oxygen flow rates were 100 mL/min and 200 mL/min respectively. The backpressure applied to both sides of the cell was 10 psig (170 kPa). Figure 3.8 shows the performance curves obtained for various cell temperatures. The polarization curves (I-V curves) at each operating temperature showed an increase in performance with increasing the cathode RH. This improvement may be attributed to the effect of relative humidity. Figure 3.8 shows the peak power density as a function of the cathode RH. This figure provides a better visualization of the performance dependence on the cathode RH. The increase in performance could be due to better hydration and increase proton conductivity of the Nafion membrane. At low cathode RH, the sharp decline in performance could be due to increase ionic resistance as a result of the poor hydration of the membrane. In summary, the NBE MEA performs well at fully humidified conditions including 80% and 100% cathode RH.

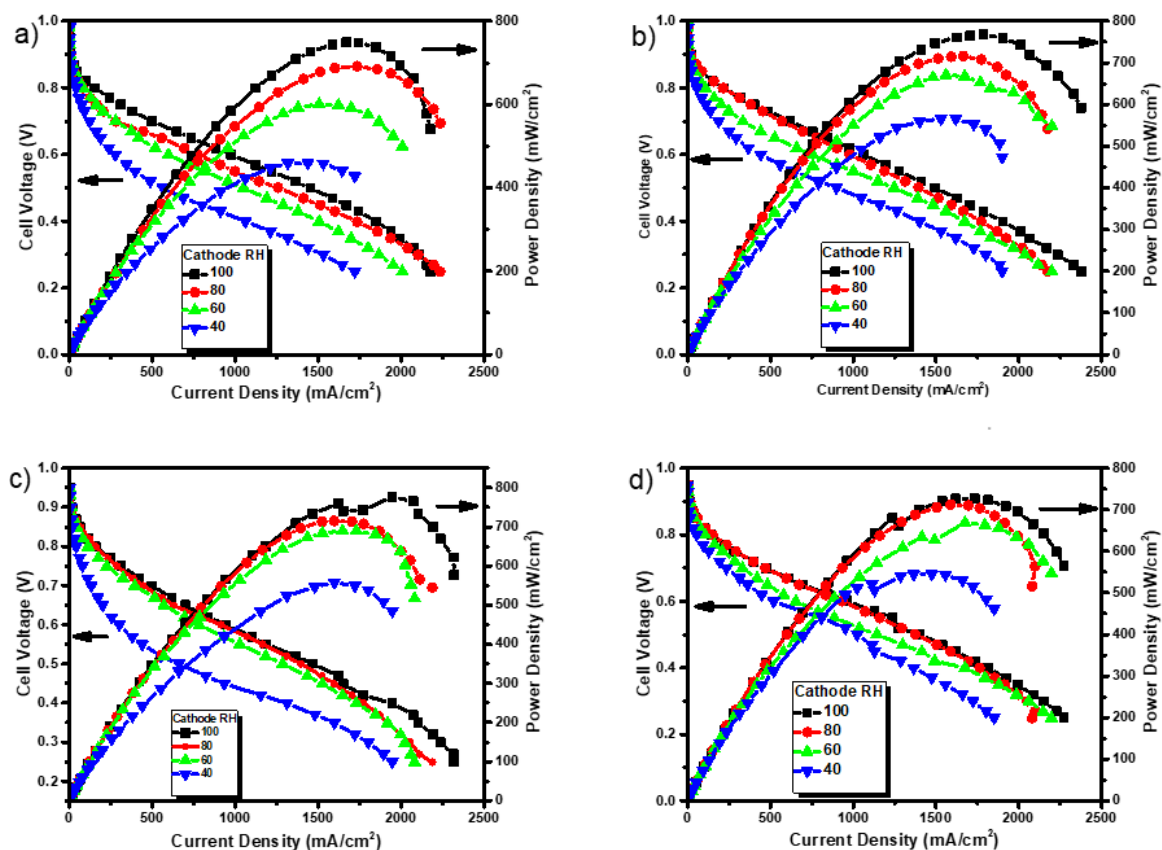


**Figure 3.8** Performance curves of the symmetric NBE MEA at various cell temperatures a) 70 °C b) 75 °C c) 80 °C and d) 85 °C as a function of the cathode RH where anode fixed at 100% RH. The flow rates of H<sub>2</sub> and O<sub>2</sub> supplied were 100- and 200-mL min<sup>-1</sup> with back pressure of 10 psig.

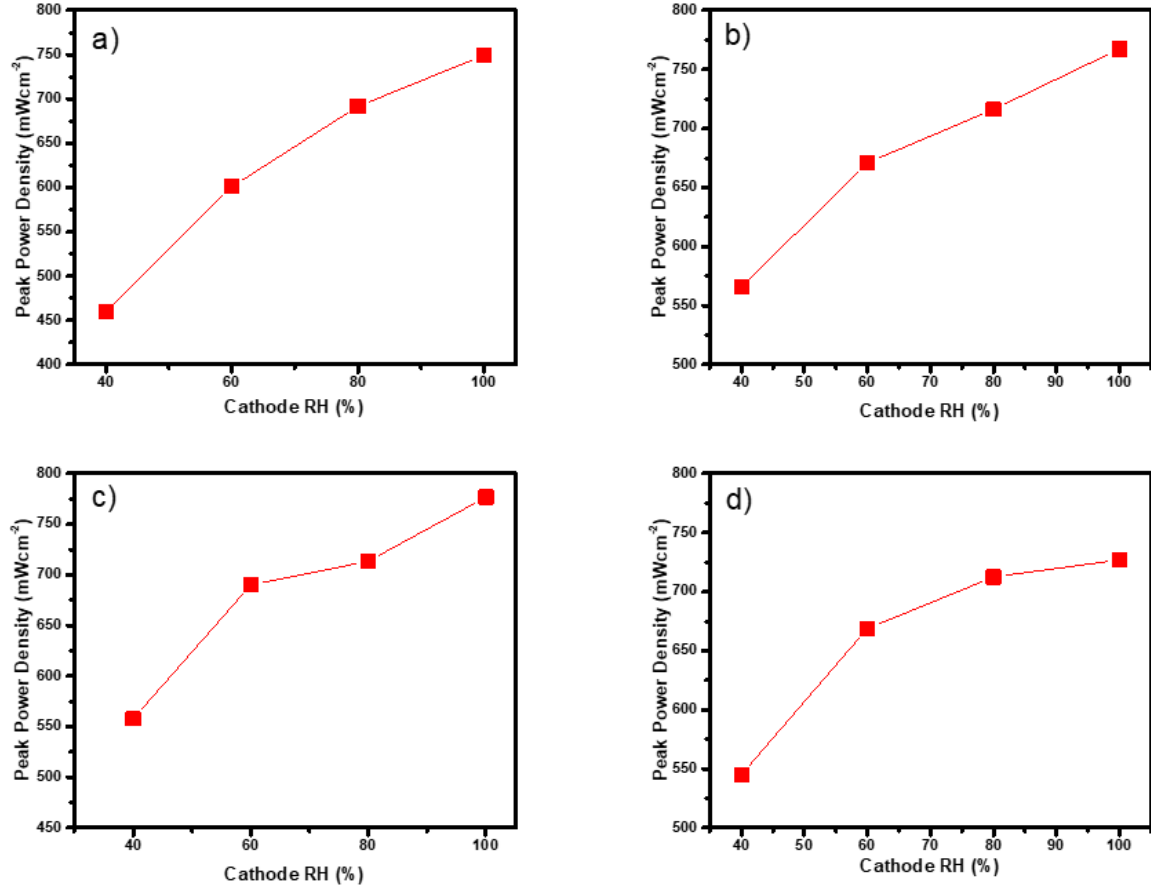


**Figure 3.9** Peak power density vs cathode RH plots obtained for Figure 3.8 data where a) 70 °C b) 75 °C c) 80 °C d) 85 °C cell temperatures.

### 3.2.1.2 The effect of pure oxygen and air oxidant on the symmetric NBE MEA

The effect of pure oxygen and air on cell performance was examined at 85 °C cell temperature and various cathode RHs. The partial pressure of oxygen in air is 20.95%. Weydahl *et al.*<sup>[69]</sup> found out that reducing the partial pressure of oxygen have a major influence on the PEM fuel cell performance. For this case, the flow rate of air was increased by a factor of 5 in order to keep oxygen stoichiometry equal for both oxidant compositions.<sup>[68]</sup> The performance curves as a function of the cathode RH are shown in Figure 3.10. The cell operated under pure oxygen (Figure 3.10.a) demonstrated higher

power densities than that operated under air (Figure 3.10.b). For instance, at the 100% cathode RH, pure oxygen shows a peak power density of  $725 \text{ mW cm}^{-2}$  compared to  $450 \text{ mW cm}^{-2}$  for the air oxidant. The loss in performance associated with air oxidant could be explained by the increased mass transport resistance of oxygen.<sup>[68,69]</sup> Moreover, the performance for both oxidants decreases with cathode RH, which could be due to dehydration of the MEA. This behavior was more pronounced for air and could be related to the high flow rate, which tends to promote drying of the MEA.

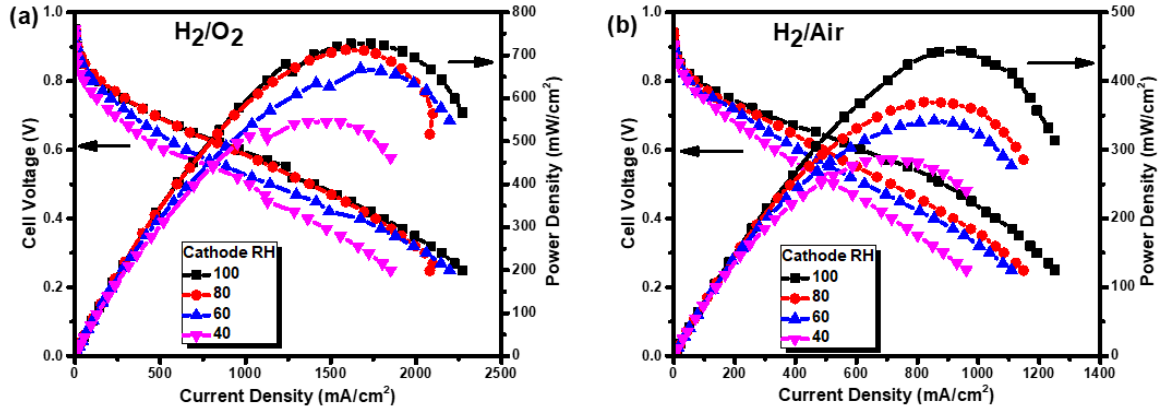


**Figure 3.10** Performance curves of the symmetric NBE MEA with (a) H<sub>2</sub>/O<sub>2</sub> (b) H<sub>2</sub>/air gas feeds configuration at cell temperature 85°C with varied cathode RH and anode fixed 100% RH. The flow rate of H<sub>2</sub> was 100 mL min<sup>-1</sup> and O<sub>2</sub> and air were 200- and 1000-mL min<sup>-1</sup> respectively with 10 psig backpressure.

### 3.2.1.3 The effect of cell temperature on the performance of the symmetric NBE MEA

The effect of the operating temperature on the NBE MEA performance was evaluated at different cell temperatures ranging from 70 to 95 °C. The anode and cathode were kept at 100% RH for each operating temperature. Figure 3.11 shows the performance of the symmetric NBE MEA under H<sub>2</sub>/O<sub>2</sub> and H<sub>2</sub>/air as a function of the cell temperature. The performance increases with increasing temperature from 70 °C to 85 °C until 90 °C and 95 °C where a significant decay in performance was observed.

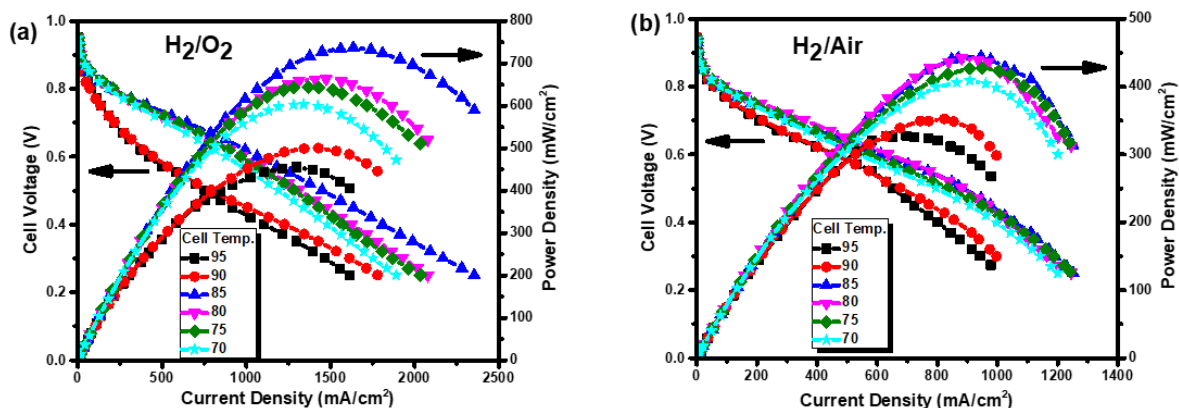


**Figure 3.11** Performance curves of the symmetric NBE MEA as a function of the cell temperature with (a) H<sub>2</sub>/O<sub>2</sub> (b) H<sub>2</sub>/air gas feeds. The flow rate of H<sub>2</sub> was 100 mL min<sup>-1</sup> and O<sub>2</sub> and air were 200- and 1000-mL min<sup>-1</sup> respectively with 10 psig backpressure. Both gases were humidified at 100% RH.

Under the H<sub>2</sub>/O<sub>2</sub> gas feeds (Figure 3.11.a), the cell operating at 70 °C and exhibited a peak power density of 570 mW cm<sup>-2</sup>, which increases gradually to 740 mW cm<sup>-2</sup> at 85 °C. This can be attributed to enhance mass transport of the reactants and membrane conductivity with increasing cell temperature. At 90 °C and 95 °C, dehydration seems to be a major issue as ionic resistance increases, resulting in a sharp decline in performance.

For the  $\text{H}_2/\text{air}$  gas feed experiments, the performance at 70 to 85 °C showed minor dependence on cell temperature. This behavior could be explained by the high flow rate of air, which could aid in efficient mass transport and water removal and, as a result, increase the cell performance. However, a decline in performance was observed at temperatures above 85 °C maybe due to drying of the MEA.

Figure 3.12 shows a plot of peak power density versus the cell temperature summarizing the trends in the performances. It was found that the cell temperature had a significant influence on membrane conductivity since proton mobility increases with operating temperature.<sup>[30,68]</sup> For the case of the symmetric NBE MEA, temperature above 85 °C could result in poor performance due to dehydration.

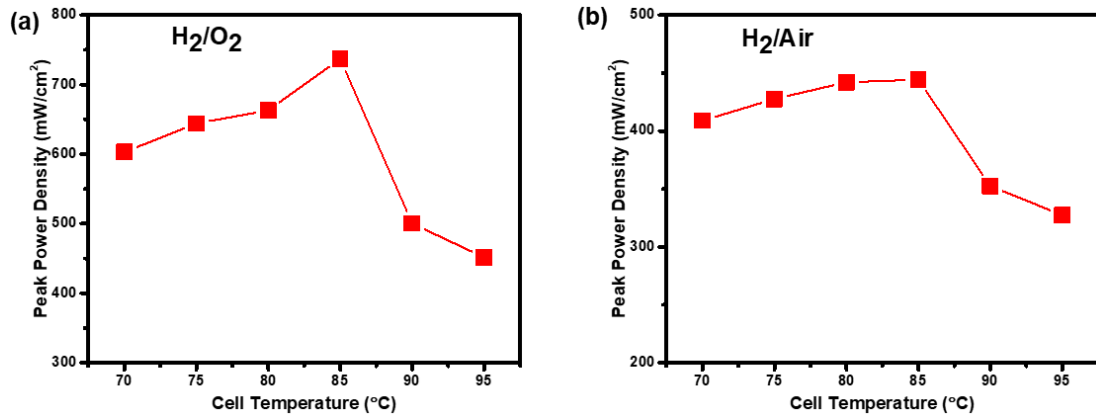


**Figure 3.12** Peak power density vs cell temperature plots extracted from the Figure 3.11

### 3.2.2 Hydrogen crossover and CV measurements of the symmetric NBE MEA

#### 3.2.2.1 The effect of cathode RH on the Pt electrochemical surface area

Figure 3.13 shows CV and the numeric ECSA plots at various cathode RH where the anode was kept at 100% RH. In Figure 3.13 (a), CVs show the redox and double layer processes of the electrode between the potential ranges of 0.08 V to 1.20 V at a scan rate of 20 mV s<sup>-1</sup>. At the potential range of 0.08 V to 0.35 V, well-defined H<sub>2</sub> adsorption/desorption peaks were obtained for high cathode RHs from 100% to 60%. These peaks became less defined when cathode RH was decreased to 40% and 20%.

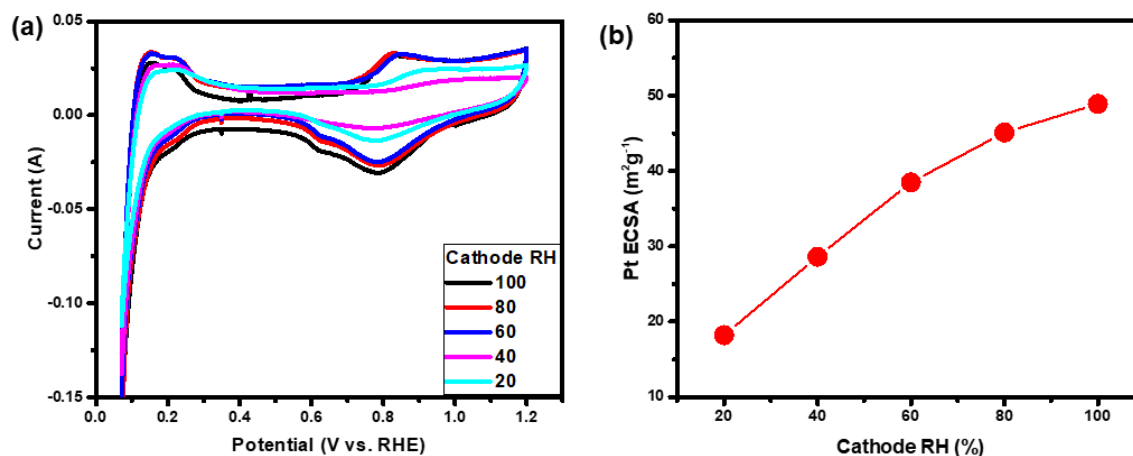


**Figure 3.13** (a) CVs (20 mV s<sup>-1</sup>) and (b) ECSA obtained for symmetric NBE MEA at 80 °C under H<sub>2</sub>/N<sub>2</sub> gas feeds. The cathode was varied between 20% and 100% RH where anode was fixed at 100% RH. Backpressure applied to both sides was 10 psig.

The variations of peaks would come from different hydration levels of the MEA. The area under the H<sub>2</sub> adsorption peak was integrated with a CView software for each CV to evaluate the ECSA. As shown in Figure 3.13 (b), the ECSA increased with cathode RH

indicating a decrease in resistivity due low water content. Moreover, at a potential greater than 0.60 V (surface oxide formation and reduction of Pt region) large irreversible peaks were obtained for high cathode RH; indicating that the higher the water content, the more oxides will form on the Pt surface.<sup>[70]</sup> It was found that more active sites (i.e., ECSA) could be access for electrochemical reactions at high RH.

### 3.2.2.2 The effect of cathode RH on the H<sub>2</sub> crossover

Hydrogen crossover was measured using a steady-state electrochemical method where the current produced from the oxidation of H<sub>2</sub> at the cathode is recorded at a potential of 0.50 V relative to the potential of the anode (SHE).<sup>[65]</sup> The backpressure applied to both anode and cathode sides were kept constant at 10 psig. In this case, mass transport by convection was neglected, which means diffusion mass transport processes were assumed to be taken place in the PEM fuel cell.<sup>[71]</sup> Figure 3.14 (a) shows a chronoamperogram as a function of cathode RH. It was observed that the current increases with decreasing cathode RH from 100 to 20%.

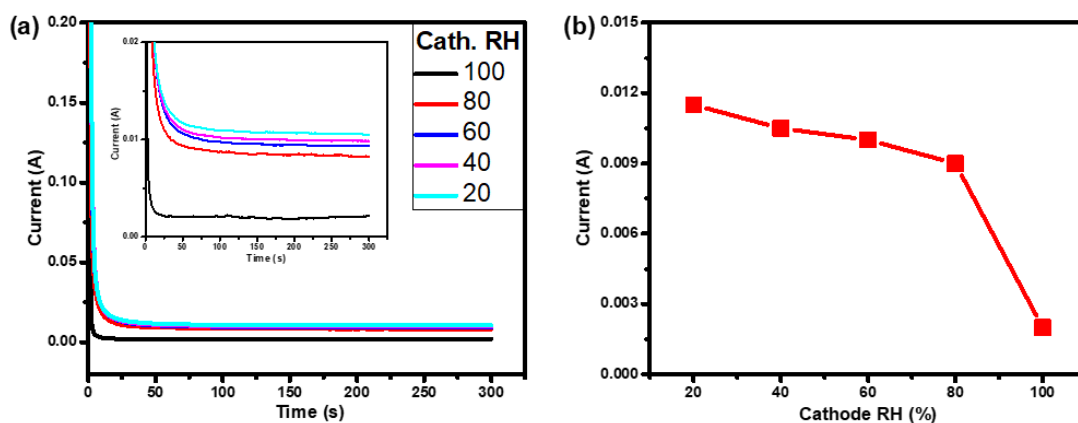


**Figure 3.14** (a) Chronoamperogram (insert = expanded graph) and (b) current measured as a function of the cathode RH for symmetric NBE MEA at a potential of 0.5 V vs RHE under H<sub>2</sub>/N<sub>2</sub> at 80 °C. The anode was fixed at 100% RH whereas the cathode RH was varied from 20 to 100% RH. The backpressure to both sides was 10 psig.



As shown in Figure 3.14 (b) the H<sub>2</sub> crossover increases with decreasing cathode RH.

The inlet total pressure of the anode gas line can be expressed as the sum of the H<sub>2</sub> partial pressure and the water vapour pressure. Based on this, Cheng *et al.*<sup>[65]</sup> suggested that an increase in RH on both sides could result in an increase in the magnitude of water vapour pressure, which would result in reduced H<sub>2</sub> partial pressure. Therefore, a decreased H<sub>2</sub> partial pressure will reduce hydrogen crossover. The same trend was observed in this experiment as increasing cathode RH resulted in low H<sub>2</sub> crossover rate. The H<sub>2</sub> crossover rate was calculated using Equation 2.2 based on the measured current. Table 3.2 shows a summary of the measured Pt ECSA and the hydrogen crossover rate.

**Table 3.2 Summary of measured Pt ECSA and H<sub>2</sub> crossover at 80 °C**

Cathode RH (%)	Pt ECSA (m <sup>2</sup> g <sup>-1</sup> )	H <sub>2</sub> crossover rate (nmol cm <sup>-2</sup> s <sup>-1</sup> )
100	48.90	2.0
80	45.10	9.0
60	38.50	10.0
40	28.62	11.0
20	18.20	12.0

### 3.2.2.3 The effect of the cell temperature on Pt electrochemical surface area

The ECSA of the NBE MEA was evaluated for various cell temperatures where the anode and cathode RHs were kept 100% on both sides. Figure 3.15 (a) represents CVs of the symmetric NBE MEA as a function of the cell temperature, ranging from 70 °C to 95 °C.

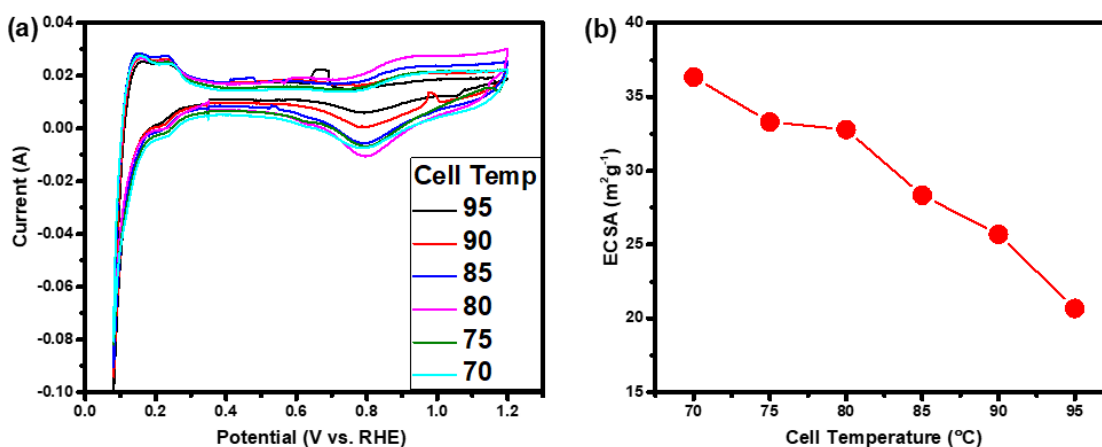


**Figure 3.15** (a) CVs (20 mV s<sup>-1</sup>) and (b) ECSA obtained for the symmetric NBE MEA at various cell temperature from 70 °C to 95 °C under H<sub>2</sub>/N<sub>2</sub> gas feeds. Both the anode and cathode gases were humidified at 100% RH. Backpressure applied at both sides was 10 psig.

The Pt oxide formation/reduction region (i.e, potential higher than 0.60 V) is greatly influenced by the cell temperature. Larger peaks of Pt oxidation/reduction were observed for lower cell temperatures from 70 to 85 °C. This could be due to the high-water sorption of the membrane (Nafion) at lower temperatures, hence more oxides were formed and reduced on the platinum surface. However, indistinct peaks of Pt oxidation/reduction were obtained at 90 °C and 95 °C, which could be due to dehydration. This could increase the

resistivity of the catalyst. Figure 3.15 (b) shows the measured ECSA as a function of the cell temperature. This plot indicates that the Pt ECSA decreases with increasing cell temperature. This is because at temperatures above 80 °C, less water would be condensed at the surface of the membrane and this would decrease water sorption.<sup>[72]</sup> This increases resistivity, thereby decreasing the ECSA.

### 3.2.2.4 The effect of the cell temperature on H<sub>2</sub> crossover

The effect of the H<sub>2</sub> crossover on the symmetric NBE MEA was evaluated for various temperatures. Figure 3.16 “a” and “b” shows the chronoamperogram a plot of the measured HOR current versus the cell temperature respectively.

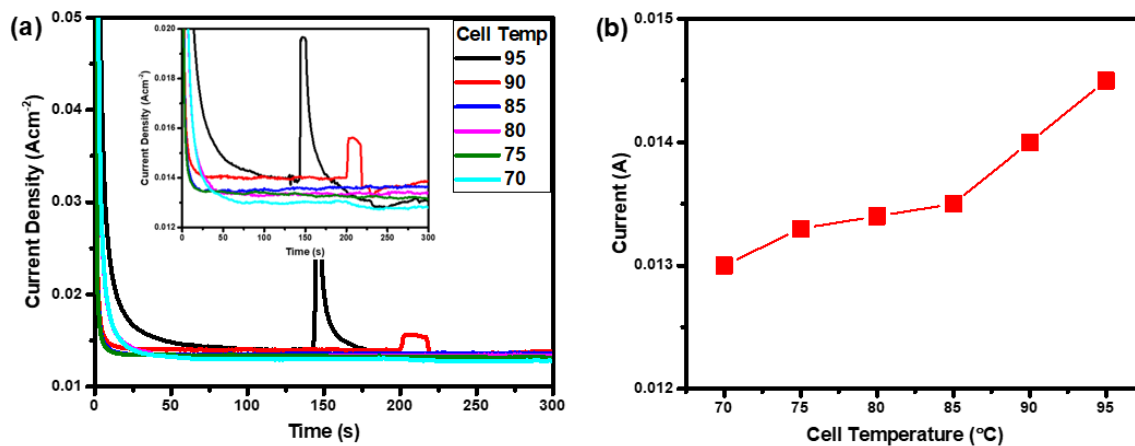


**Figure 3.16** (a) Chronoamperogram (inserted = expanded (a)) and (b) current measured with symmetric NBE MEA at a potential of 0.5 V vs RHE under H<sub>2</sub>/N<sub>2</sub> at various cell temperature from 70 °C to 95°C. The anode and cathode was fixed at 100% RH. The backpressure on both sides was 10 psig.

From the inserted graph that H<sub>2</sub> crossover increases with increasing the cell temperature. Truc *et al.*<sup>[71]</sup> have also reported the same trend in the temperature range of 30 °C to 90 °C and attributed their results to increased H<sub>2</sub> diffusion coefficient as the cell temperature increases. It has been postulated by Yoshitake *et al.*<sup>[73]</sup> that increasing temperature could be a key cause of the mechanical failure of the membrane, which could either be the formation of pin holes or the detachment of the membrane from the electrode. When these occur, the permeability of the H<sub>2</sub> through the membrane increases. The peaks observed at high temperatures could be due to slugs of liquid in the cell. This probably indicates that the NBE MEA presents an unstable operation conditions at high temperatures, which could have great influence on the overall performance.

Table 3.3 presents a summary of the measured Pt ECSA and the H<sub>2</sub> crossover rates as a function of the cell temperature. It was found that the rate at which molecular hydrogen crosses from the anode increases with temperature.

**Table 3.3 Summary of measured Pt ECSA and H<sub>2</sub> crossover rate for various cell temperature**

Cell temperature (°C)	Pt ECSA (m <sup>2</sup> g <sup>-1</sup> )	H <sub>2</sub> crossover rate (nmol cm <sup>-2</sup> s <sup>-1</sup> )
70	36.34	13.5
75	33.30	13.8
80	32.80	13.9
85	28.35	14.0
90	25.70	14.5
95	20.70	15.0

### 3.2.3 EIS measurements of the symmetric NBE MEA

#### 3.2.3.1 EIS measurements of the symmetric NBE MEA at varied cathode RH

Impedance measurements were conducted on the symmetric NBE MEA at 425 mV as a function of the cathode RH. This potential (425 mV) is suitable for probing the intrinsic charge/mass transport properties of the catalyst because it lies within the double layer region of the CV where no faradaic processes is expected to occur.<sup>[74]</sup> Figure 3.17 shows the Nyquist, capacitance, and normalized capacitance plots for the symmetric NBE MEA at 80 °C and various cathode RH, ranging from 20 to 100%.

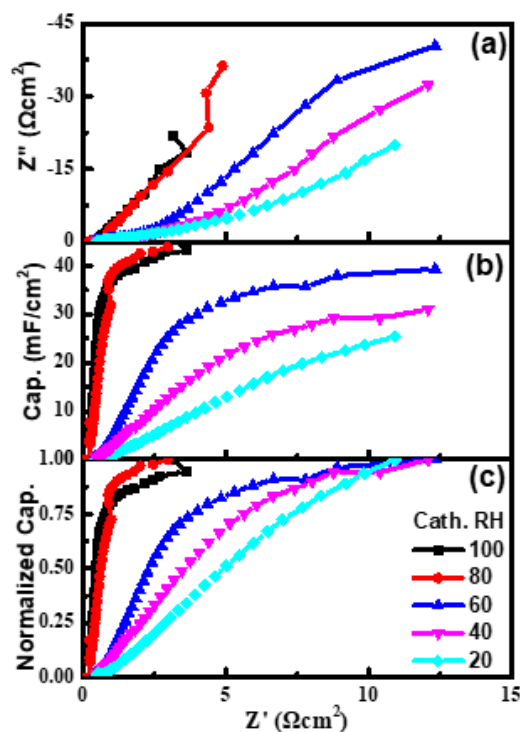


**Figure 3.17** (a) Nyquist (b) capacitance and (c) normalized capacitance plots for the symmetric NBE MEA at 80 °C under H<sub>2</sub>/N<sub>2</sub> gas feeds. The anode was fixed at 100% RH whereas the cathode RH was varied between 20 to 100%. DC bias potential of 0.425 V was applied. Backpressure of 10 psig was applied on both sides.

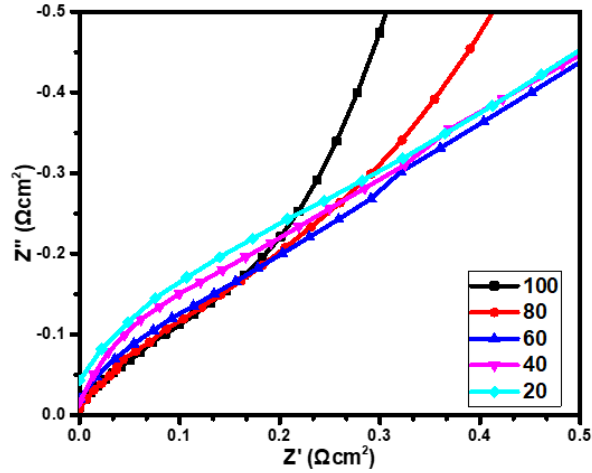


**Figure 3.18** Expansion of the high frequency region of the Nyquist plot.

As mentioned earlier in chapter 2, the Nyquist plot (Figure 3.17.a) shows two main regions. First, the high frequency (Warburg-type response), which represents the electronic and ionic resistances in the CL.<sup>[74]</sup> The Warburg impedance is often referred to as the ionic resistance, since the contribution of the electronic resistance might be small.<sup>[61]</sup> In the low frequency region, the impedance plot curves up, which indicates the capacitive nature of the CL.<sup>[74]</sup> The resistance associated with the proton conduction in the membrane was subtracted from the experimental data. By expanding the high frequency region of the Nyquist plot as shown in Figure 3.18, the total ionic resistance was manually estimated ( $R_{\Sigma} = 3 \times \text{length of Warburg response projected onto the real axis, } Z'$ ).<sup>[61,74]</sup> Under fully humidified conditions (100% and 80% RH), the length of the Warburg is smaller indicating low ionic resistance. On the other hand, the length increased with decreasing the cathode RH from 60% to 20% which was attributed to larger ionic resistance due to reduced water content.

Figure 3.17 (b) and (c) show the capacitance and the normalized capacitance plots respectively. These plots give better understanding of how the conductivity varies across the CL.<sup>[57,61]</sup> At the 100 and 80% cathode RH, the length of the slopes at mid frequency is steeper indicating smaller ionic resistance. Upon decreasing the cathode RH from 60% to 20%, the slopes became less steep indicating high ionic resistance. These differences could be explained by the degree of hydration of the MEA where high RH reduces resistivity in the CL.

The membrane resistance ( $R_M$ ), total ionic resistance ( $R_\Sigma$ ) and the limiting capacitance associated to the symmetric NBE MEA were extracted from the EIS data. Figure 3.19 shows the  $R_M$ ,  $R_\Sigma$ , and the limiting capacitance of the symmetric NBE MEA as a function of the cathode RH. These parameters are useful for obtaining the optimum operating conditions of fuel cell electrodes. All the three parameters were greatly influenced by the humidification conditions where the  $R_M$  and the  $R_\Sigma$  increases with decreasing cathode RH. Similarly, the limiting capacitance also decreases with the cathode RH. These can be attributed to the poor proton conduction in dry conditions.

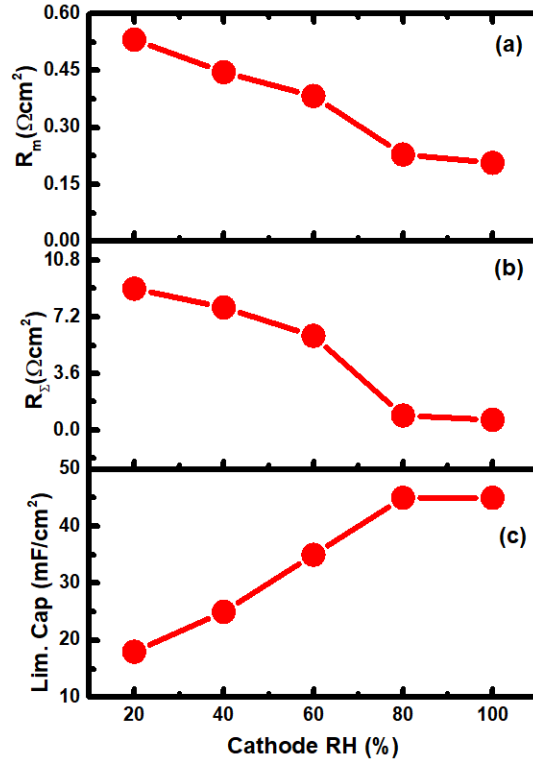


**Figure 3.19** (a) Membrane resistance (b) total ionic resistance and (c) limiting capacitance of the symmetric NBE MEA as a function of cathode RH at 80 °C.

### 3.2.4 The effect of the cell temperature on the NBE conductivity

The ionic transport properties of the symmetric NBE MEA were monitored as a function of the cell temperature, ranging from 70 to 95 °C at 100% RH. The Nyquist and capacitance plots are shown in Figure 3.20. In Figure 3.20.a, the slopes become less steep as the cell temperature increases indicating larger ionic transport resistance.



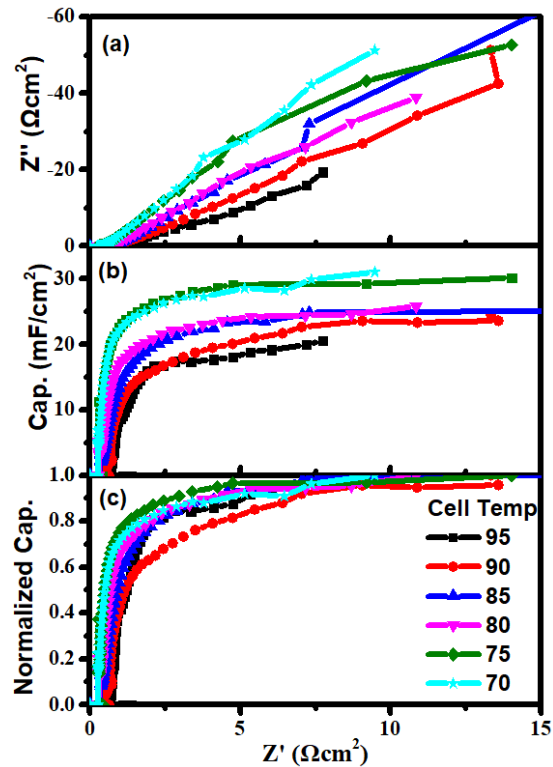


**Figure 3.20** (a) Nyquist (b) capacitance and (c) normalized capacitance plots obtained for the symmetric NBE MEA as a function of the cell temperature under  $\text{H}_2/\text{N}_2$  gas feeds. The anode and cathode gases were humidified at 100% RH. DC bias potential of 0.425 V was applied. Backpressure of 10 psig was applied on both sides.

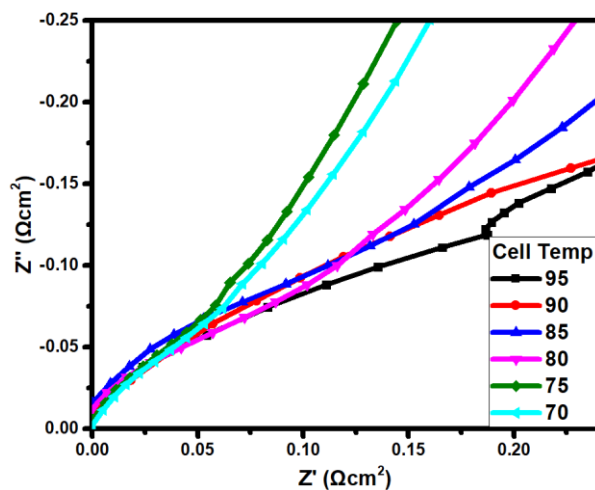


**Figure 3.21** Expansion of the high frequency region of the Nyquist plot

In Figure 3.21, the ionic resistances estimated from the Warburg length increase with temperature. This could be attributed to the difficulty of the membrane (Nafion) to adsorb water as the temperature increases from 80 °C to 95 °C.<sup>[72]</sup> This may result in the dehydration of the membrane and would contribute to the larger ionic resistance with increasing temperature.<sup>[75]</sup>

The resistivity across the CL can be clearly seen in the capacitance plots shown in Figure 3.20.b. From this figure, the length of the mid frequency slopes (i.e., before the plateau at limiting capacitance) decreases with temperatures from 70 °C to 95 °C. This could be due to the reduced water content at the membrane/electrode interface with increasing temperature.<sup>[72]</sup> When this occurs, the membrane tends to detach from the electrode, which may have contributed to increase the ionic resistance of the CL.<sup>[75]</sup> Figure 3.20.c shows the normalized capacitance plot as a function of the temperature. The plots were normalized to provide a better visual (i.e., qualitative) comparison of ionic conductivity of electrodes that had different limiting capacitance values <sup>[38,61]</sup>. It can be seen (Figure 3.20.c) that the conductivities are approximately the same for all operating conditions.

Figure 3.22 shows the  $R_M$ ,  $R_\Sigma$  and the limiting capacitance as a function of temperature. This figure gives a more quantitative description of the high ionic resistance associated with the symmetric NBE MEA. It was found that  $R_M$  and  $R_\Sigma$  increases with temperature, which resulted in a decrease in the limiting capacitance. It can be inferred from the plots that the high ionic resistance associated with increasing the temperature could be due to the retard water sorption of the membrane with temperature.<sup>[72]</sup>

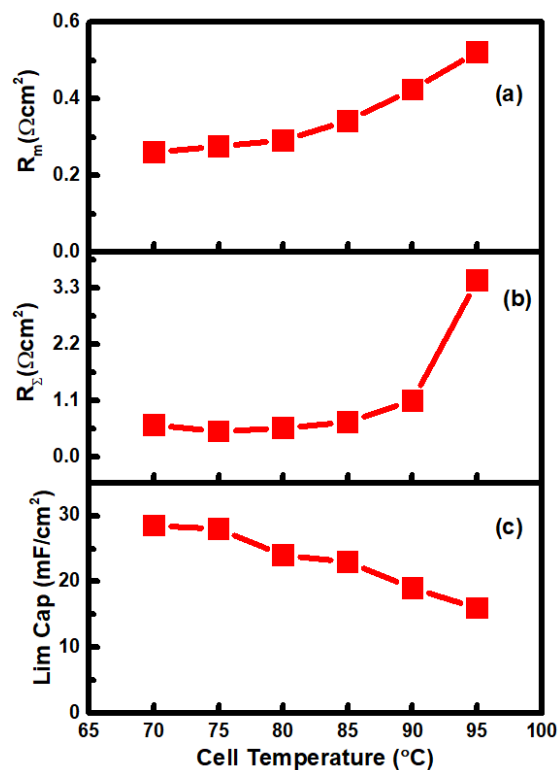


**Figure 3.22** (a) membrane resistance (b) total ionic resistance and (c) limiting capacitance of the symmetric NBE MEA as a function of the cell temperature from 70 to 95 °C at 100% RH.

### 3.3 Electrochemical evaluation of sulfonated silica ceramic carbon electrodes

#### 3.3.1 Fuel Cell Testing

##### 3.3.1.1 Effect of the cathode RH on the performance of the symmetric SS-CCE MEA.

To investigate the influence of cathode humidification on the symmetric SS-CCE MEA performance, the anode RH was kept constant at 100% and the cathode RH was varied from 20% to 100%. The backpressures at both sides were set at 10 psig (170 kPa). The cell measurements were conducted at various cell temperatures, ranging from 70 °C to 85 °C. Figure 3.23 shows the performance curves for various cell temperatures and cathode RH. The performance was investigated with the same electrode composition, but different

MEA assemblies. There was no difference in performance for all the MEAs investigated, which confirms the reproducibility of these results.

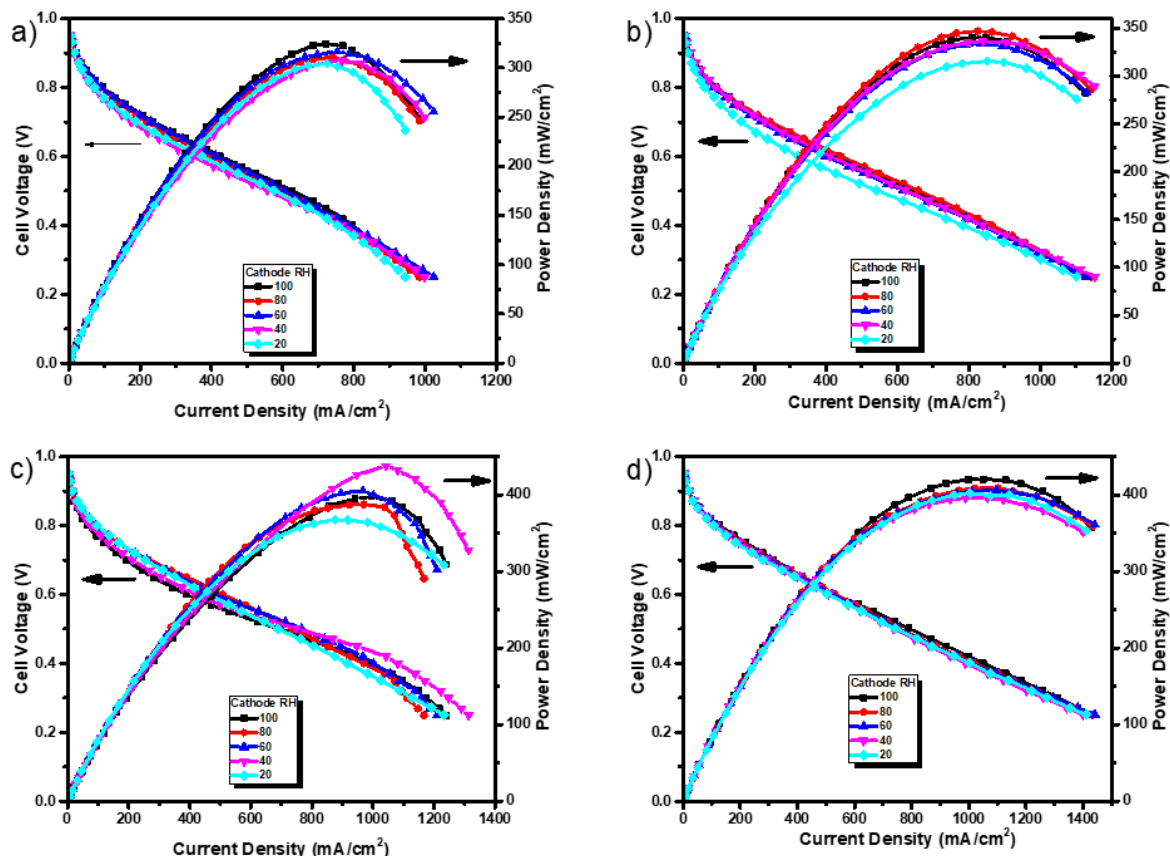


**Figure 3.23** Performance curves of the symmetric SS-CCE MEA for various cell temperatures: a) 70 °C b) 75 °C c) 80 °C d) 85 °C and cathode RH where the anode is fixed at 100% RH. The flow rates of H<sub>2</sub> and O<sub>2</sub> supplied were 100- and 200-mL min<sup>-1</sup> with a back pressure of 10 psig.

Performance curves show minor dependence on cathode RH at all operating temperatures. For instance, at cell temperature 85 °C, 100% RH showed a peak power density of 420.5 mW cm<sup>-2</sup> whereas 20% RH showed 402.1 mW cm<sup>-2</sup> peak power density. This performance shows that there was just 4% decay in performance by decreasing cathode RH from 100 to 20%. This indicates that the SS-CCE was able to retain water for

membrane hydration, which led to effective proton conductivity under low relative humidity.<sup>[24,38]</sup> Several authors have reported similar performances with silica-based MEA.<sup>[1,21-29,30-35]</sup> Besides, it is noteworthy that the performance at high current densities were seen to improve for low cathode RH. This was evident at a cell temperature of 80 °C, where 100% cathode RH showed limiting current of 1241 mA cm<sup>-2</sup> whereas 40% cathode RH showed 1313 mA cm<sup>-2</sup>. This could be the effect of RH. Since the SS-CCE catalyst is hydrophilic, flooding could be the major issue resulting in poor cell performance due to mass transfer limitation at high RH. On the other hand, operating at low cathode RH could eliminate flooding and enhance mass transfer process, thereby increasing performance. Therefore, operating a fuel cell with the symmetric SS-CCE MEA will require a low to intermediate cathode RH for better performance.

### **3.3.1.2 Effect of the temperature on the performance of the symmetric SS-CCE MEA**

Figure 3.24 shows the performance curves for the SS-CCE as a function of cell temperature at 100% anode and cathode RH. The performances were seen to increase with the operating temperature in the current density range. The maximum power density at 100% RH were 360 mW/cm<sup>2</sup> at 70 °C, 370 mW/cm<sup>2</sup> at 75°C, 410 mW/cm<sup>2</sup> at 80 °C, 421 mW/cm<sup>2</sup> at 85 °C, and 425 mW/cm<sup>2</sup> at 90 °C. This improvement with temperature may be attributed to the effect of the reaction kinetics, especially for the oxygen reduction reaction (ORR). This could decrease the charge-transfer resistance with the cell temperature. On the other hand, when the cell temperature was further increase to 95 °C, the maximum power density decreased to 410 mW cm<sup>-2</sup> as shown in Figure 3.24.b. This could be related to the mechanical stability of the membrane (Nafion) at that elevated

temperature, which could increase the charge-transfer resistance.<sup>[79]</sup> This could limit the benefits of the SS-CCE catalyst for higher temperatures operation. The reason for this requires further investigation.

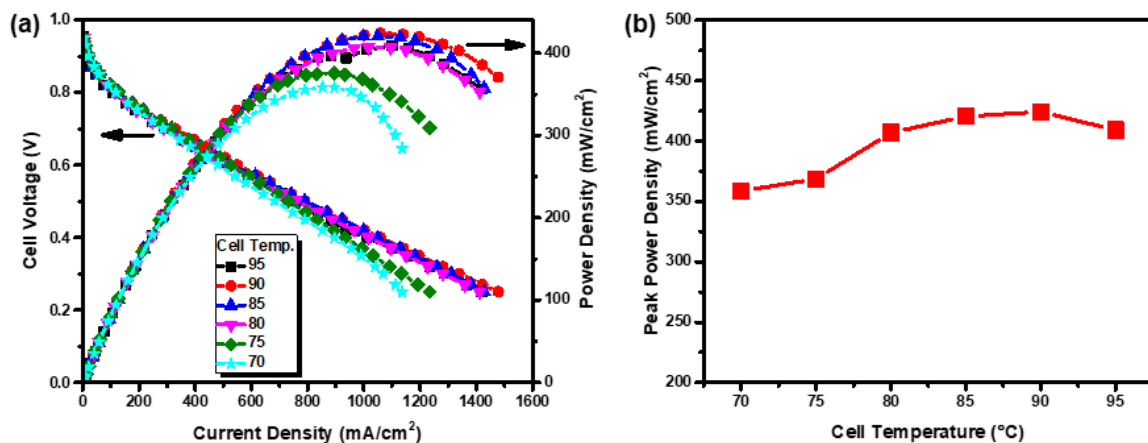
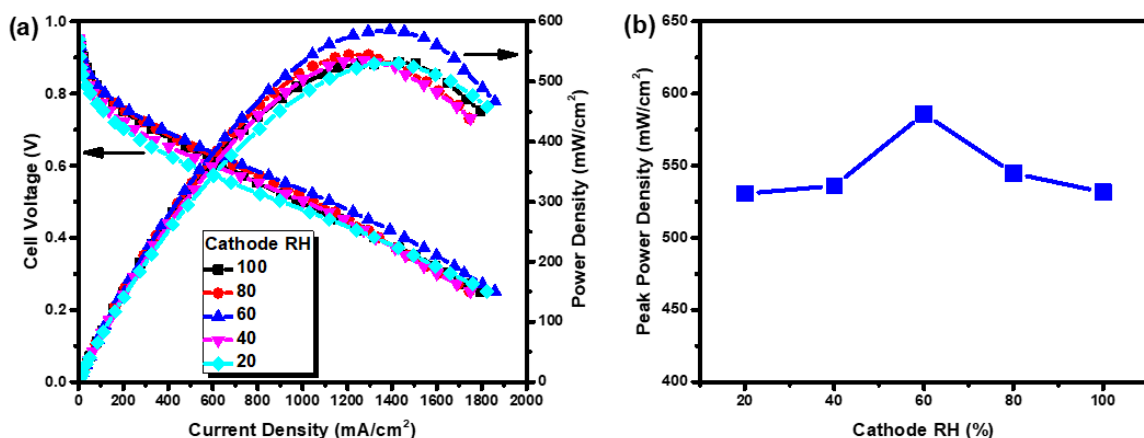


**Figure 3.24** (a) Performance curves of the symmetric SS-CCE MEA as a function of the cell temperature with H<sub>2</sub>/O<sub>2</sub> and (b) peak power density vs cell temperature curves. The flow rate of H<sub>2</sub> and O<sub>2</sub> was 100 and 200 mL min<sup>-1</sup> respectively with 10 psig backpressure. Both gases were humidified at 100% RH.

### 3.3.2 Effect of asymmetric SS-CCE MEA configuration on the performance

#### 3.3.2.1 Influence of the cathode RH on the asymmetric SS-CCE MEA

The performance of an asymmetric SS-CCE MEA was assessed as a function of cathode RH. The asymmetric SS-CCE MEA was composed of a NBE anode CL and a SS-CCE cathode CL as shown in Table 2.1. The anode RH was kept at 100% whereas the cathode RH was varied from 100% to 20%. The cell was operated at 85 °C with flow rates set at 100 mL min<sup>-1</sup> for the H<sub>2</sub> and 200 mL min<sup>-1</sup> for the O<sub>2</sub> and a backpressure of 10 psig (170 kPa) was applied to both sides. Figure 3.25 presents the performance of an asymmetric SS-CCE MEA as a function of the cathode RH. It was found that the asymmetric SS-CCE MEA showed a minor dependence on cathode RH like the symmetric SS-CCE MEA.



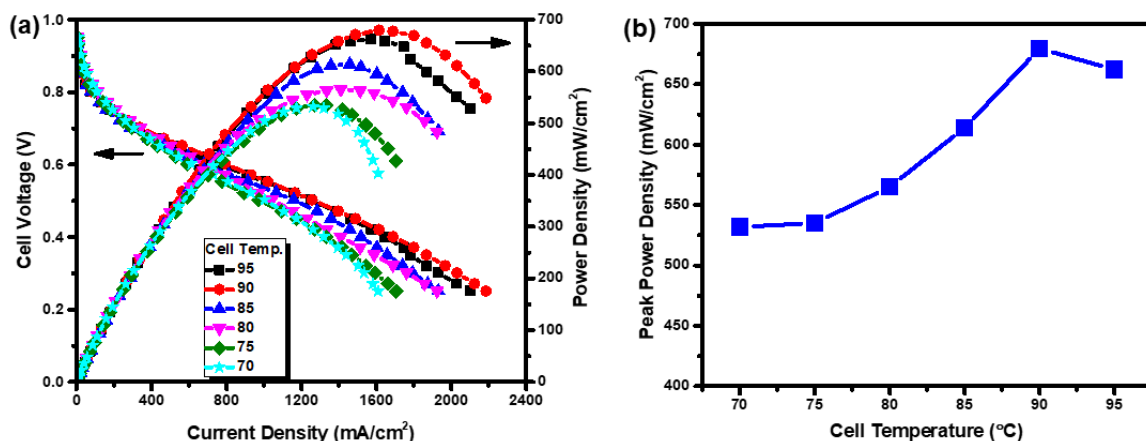
**Figure 3.25** (a) Performance curves and (b) peak power density of the asymmetric SS-CCE MEA at 85 °C and various cathode RH, ranging from 20% to 60% where anode is kept at 100% RH. The flow rate of  $\text{H}_2$  and  $\text{O}_2$  was 100- and 200- $\text{mL min}^{-1}$  respectively with 10 psig backpressure.

Figure 3.25.b shows a plot of the peak power density versus the cathode RH. The improvement at 60% cathode RH may be attributed to the hydration effect. This was explained that at the mid cathode RH (i.e., 60%), the cell is not too wet (above 60%) or too dry (below 60%), which could result in efficient proton conduction. Because the SS-CCE catalyst is hydrophilic, high RH could increase the mass transport limitation while low RH could increase the ionic transfer resistance, thereby decreasing performance of the PEM fuel cell.

Interestingly, the asymmetric SS-CCE MEA showed an improved performance compared to the symmetric SS-CCE MEA. The asymmetric SS-CCE MEA recorded a maximum power density of  $600 \text{ mW cm}^{-2}$  compared to the  $420 \text{ mW cm}^{-2}$  of the symmetric SS-CCE MEA. This could be explained by the combined improvement of the ionic and mass transport processes, resulting in high  $\text{H}_2$  and  $\text{O}_2$  utilization at the anode and cathode side respectively, and by the absence of liquid water at the membrane/electrode interface.

### 3.3.2.2 Influence of temperature on the performance of the asymmetric SS-CCE MEA

The performance of an asymmetric SS-CCE MEA as a function of the cell temperature, ranging from 70 °C to 95 °C is shown in Figure 3.26. The performance of the cell improves with cell temperature from 70 °C to 90 °C, but showed a slight decrease at 95 °C. This performance trend was like that observed for the symmetric SS-CCE MEA. The decrease in performance at 95 °C could be due to the poor water sorption of the membrane in such hot condition.<sup>[72]</sup> Interestingly, the asymmetric SS-CCE MEA showed higher performances than symmetric SS-CCE MEA as shown in Figure 3.26.b.



**Figure 3.26** (a) Performance and (b) peak power density curves for the asymmetric SS-CCE MEA as a function of the cell temperature at 100% RH. The flow rate of H<sub>2</sub> and O<sub>2</sub> was 100- and 200-mL min<sup>-1</sup> respectively with a 10 psig backpressure.

This indicates that employing an NBE at the anode side of the MEA increases the exchange current density and reduces mass transport losses due to flooding. With increasing the current density, the performance began to drop sharply at low temperatures (i.e., 70 °C and 75 °C) while those above 80 °C kept their pace. This could be due to mass transport issues (especially flooding) in the high current density when the cell is operated at low



temperature. With increasing the cell temperature, mass transport resistance decreases, which resulted in improved performance at high current density.<sup>[80]</sup>

### **3.3.2.3 Effect of H<sub>2</sub>/air gas feeds on the asymmetric SS-CCE MEA**

Fuel cell testing was carried out to investigate the effect of air oxidant on the asymmetric MEA. Two sets of experiments were conducted. One set was to investigate the performance at 85 °C with various cathode RH and the other set was for various cell temperatures and 100% RH on both sides. The flow rates of hydrogen and air were 100- and 1000-mL min<sup>-1</sup> respectively. The cell was operated at 10 psig (170 kPa) backpressure. Figure 3.27 shows the asymmetric MEA performance curves as a function of cathode RH (Figure 3.27.a) and cell temperature (Figure 3.27.b). The cell tested with air oxidant exhibited lower performances than that of cell tested under pure oxygen (Figure 3.25 and 3.26). This may be explained by the dilution of oxygen concentration in air composition, which could result in increased mass transport resistance.<sup>[68]</sup> Besides, the performances were seen to change rapidly with the cathode RH and cell temperature fluctuations. These can be seen in the peak power density plots shown in Figure 3.28. These may be due to the hydration effect of the MEA. Moreover, the variation was different than that observed when using pure oxygen (Figure 3.25 and 3.26). This could be explained by the high flow rate of air oxidant (1000 mL/min) compared to the pure oxygen (200 mL/min). The high flow rate of the air could enhance evaporation of water in the cell. This tends to decrease the proton conductivity of the membrane and the overall performance of the cell. Therefore, using pure air as an oxidant can offset the benefits of operation of the SS-CCE at high cell temperatures and low relative humidities.

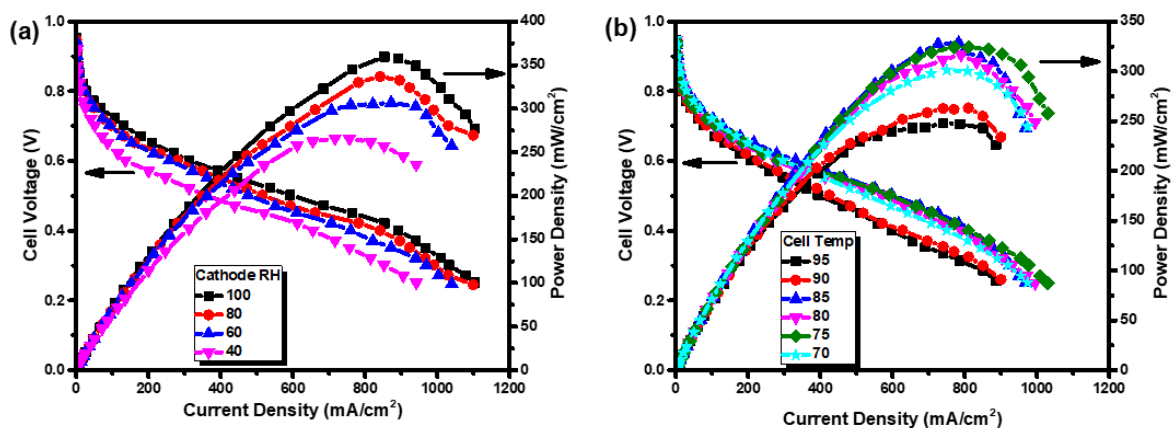


**Figure 3.27** Performance curves of the asymmetric SS-CCE MEA as a function of (a) cathode relative humidity at 80 °C and (b) cell temperature at 100% RH. The flow rate of  $H_2$  and air was 100- and 1000- $mL\ min^{-1}$  respectively with 10 psig backpressure.

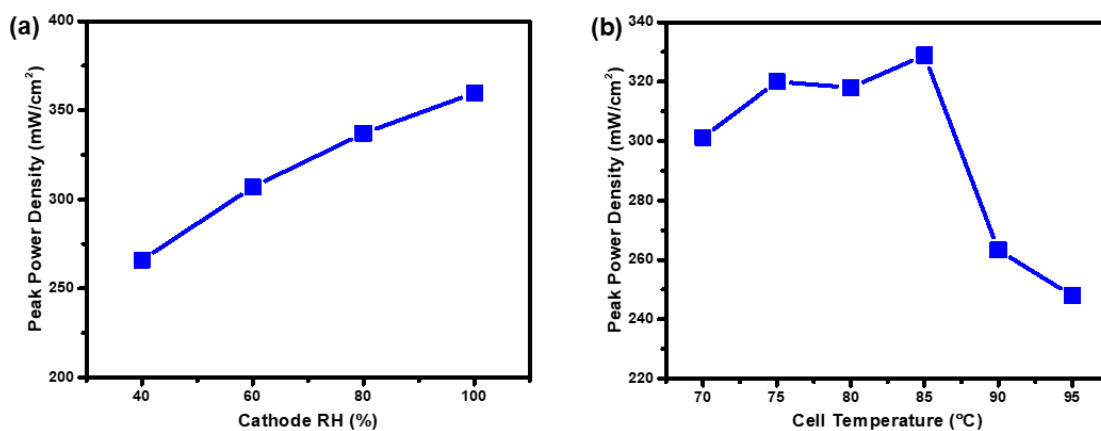


**Figure 3.28** Peak power density vs (a) cathode RH at 80 °C and (b) cell temperature at 100% RH plots extracted from Figure 3.27.

### 3.3.3 Hydrogen crossover and CV measurements of the asymmetric SS-CCE MEA

#### 3.3.3.1 Effect of cathode RH on Pt electrochemical surface area

Figure 3.29 shows the CVs measured under hydrogen (anode) and nitrogen (cathode) for the asymmetric SS-CCE MEA as a function of the cathode RH at 80 °C. The hydrogen adsorption/desorption peaks were observed at potentials lower than 0.40 V as shown in Figure 3.29.a. The area under the H desorption peaks was used to estimate the ECSA. Figure 3.29.b shows the measured ECSA as a function of the cathode RH. The ECSA increases with increasing cathode RH. This could be due to the presence of water at the catalyst/membrane interface, which tends to expose more active sites of the platinum electrode. In contrast, the reduced water content at lower RH tends to increase resistivity in the CL resulting in lower active areas.

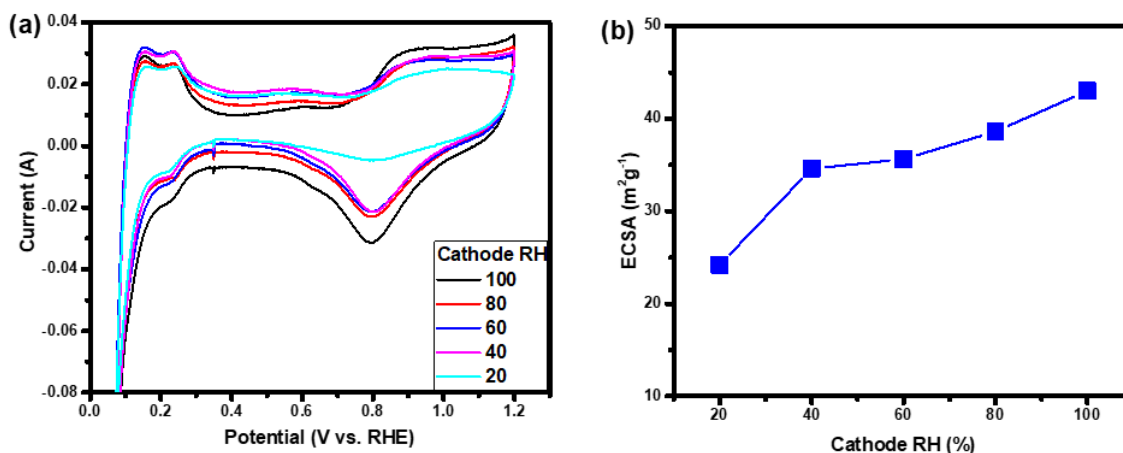


**Figure 3.29** (a) CVs (20 mV s<sup>-1</sup>) and (b) ECSA measured for asymmetric SS-CCE MEA at 80°C under H<sub>2</sub>/N<sub>2</sub> gas feeds. The cathode was varied between 20 and 100% RH where anode was fixed at 100% RH. Backpressure applied at both sides was 10 psig.

### 3.3.3.2 Effect of cathode RH on the H<sub>2</sub> crossover

After the CV measurements, a steady state electrochemical method was used to measure the current produced because of the oxidation of the H<sub>2</sub> crossed from the anode side to the inert cathode compartment. Figure 3.30.a shows the current as a function of time for various cathode RH. The current was plotted against the cathode RH as shown in Figure 3.30.b. It can be clearly seen that decreasing cathode RH has led to increase the current, which implies the increase in the H<sub>2</sub> crossover.

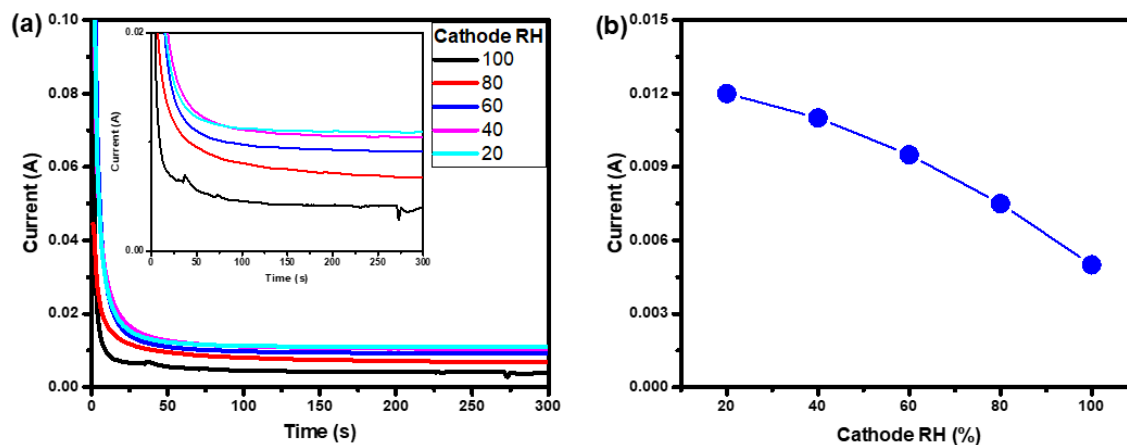


**Figure 3.30** (a) Chronoamperogram and (b) current measured with asymmetric SS-CCE MEA at a potential of 0.5 V vs RHE under H<sub>2</sub>/N<sub>2</sub> at 80 °C. The anode was fixed at 100% RH whereas the cathode RH was varied from 20 to 100% RH. The backpressure on both sides was 10 psig.

Many authors have reported that H<sub>2</sub> crossover increases with RH<sup>[68,69,71,73]</sup> while Cheng et al.<sup>[65]</sup> have described that the permeability of the H<sub>2</sub> by RH effect is complicated. However, all these studies were for a symmetrical RH as opposed to this experiment which was conducted for an asymmetrical RH. The trend of the H<sub>2</sub> crossover could be explained by the concentration gradient of the water that exits between anode and cathode

compartment. This would mean that the rate at which dissolved  $H_2$  at the anode compartment (100% RH) and diffuses to the cathode side increases as the cathode RH decreases. Besides, operating at low RH could to pin-hole formation in the membrane, thereby increasing the rate of the  $H_2$  crossover. Table 3.4 shows a summary of the calculated Pt ECSA and the  $H_2$  crossover rate at various cathode RH.

**Table 3.4 Summary of measured Pt ECSA and  $H_2$  crossover rate for various cathode RH**

Cathode RH (%)	Pt ECSA ( $m^2 g^{-1}$ )	$H_2$ crossover rate ( $nmol cm^{-2} s^{-1}$ )
20	24.2	12.0
40	34.6	11.0
60	35.6	10.0
80	38.6	8.0
100	43.0	5.0

### 3.3.4 EIS measurements of the asymmetric SS-CCE MEA

#### 3.3.4.1 Assessing the conductivity of the asymmetric SS-CCE MEA for various cathode RH

EIS was used to characterize the ion transport resistances of the asymmetric SS-CCE MEA under  $H_2/N_2$  gas feeds. The measurements were conducted for various cathode RH while the anode was kept at 100% RH. Figure 3.31 shows the Nyquist and capacitance plots at 80 °C for various cathode RH. With decreasing the cathode RH from 100% to 20%, the slopes of the plots were seen to decrease. This may be explained by the effect of the ion conduction of the CL.

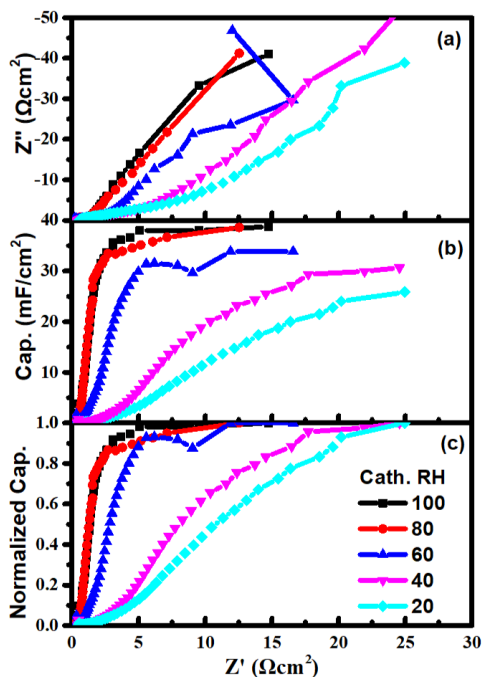


**Figure 3.31** (a) Nyquist, (b) capacitance, and (c) normalized capacitance plots for the asymmetric SS-CCE MEA at 80 °C under  $H_2/N_2$  gas feeds. The anode was fixed at 100% RH whereas the cathode RH was varied between 20% and 100%. DC bias potential of 0.425 V was applied. Backpressure of 10 psig was applied on both sides.

In Figure 3.31.a, the high frequency was expanded to give a better visualization of the Warburg region. This was shown in Figure 3.32. As mentioned previously, the Warburg length could give an estimation of the ionic resistance of the CL. The decreasing of the cathode RH increases the Warburg length. This shows that decreasing the cathode RH has led to increase ion transport resistance.

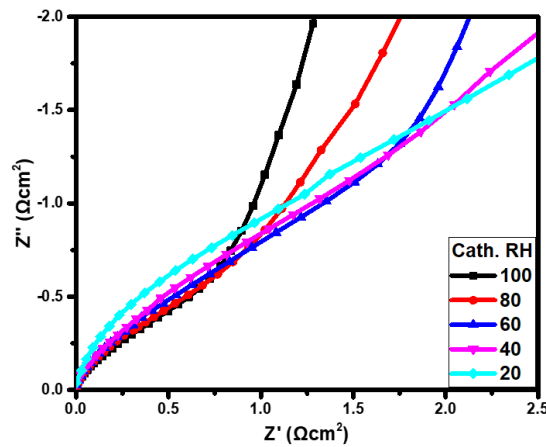


**Figure 3.32** Expansion of the high frequency region of the Nyquist plot from which the ionic resistances were estimated.

The ion transport behavior was further analysed by the capacitance plots as shown in Figure 3.31.b. At the mid frequency region, the length of the slope at the 80% and 100% cathode RH were the same steepness indicating similar resistivities. With decreasing the cathode RH from 60% to 20% the slopes became less steep as the length decreases due to different resistivities at various humidification levels. The capacitance plots were normalised to provide a qualitative comparison for the various cathode RH. As shown in Figure 3.31.c, the steepness of the slope decreases with decreasing cathode RH. This could be due to larger ionic resistances with decreasing the cathode RH.<sup>[39, 79]</sup>

To obtain numerical insights the influence of the cathode RH on the  $R_M$ ,  $R_\Sigma$  and the limiting capacitance was plotted, as shown in Figure 3.33. The limiting capacitance decreases as the  $R_M$  and  $R_\Sigma$  increases with decreasing the cathode RH from 100% to 20%. Since water conducts protons well, the increased ionic resistivity may be due to reduced water content in the CL. This also explains why EIS would not be an appropriate tool to characterize flooding in the cell.

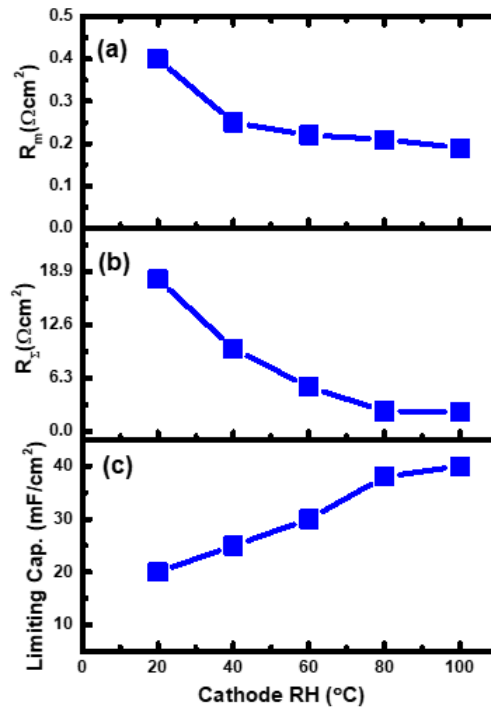


**Figure 3.33** (a) Membrane resistance (b) total ionic resistance and (c) limiting capacitance of the asymmetric SS-CCEE MEA as a function of cathode RH at 80 °C.



### 3.3.4.2 Assessing the Pt ECSA of the asymmetric SS-CCE MEA for various cell temperatures

Figure 3.34.a shows CVs of the asymmetric SS-CCE MEA for various cell temperatures at 100% RH on both anode and cathode sides. The CVs presented large  $H_2$  adsorption/desorption (potential  $< 0.40$  V) and oxide formation/reduction peaks (potential  $> 0.70$  V) at all temperatures. This could be ascribed to the ability of the asymmetric SS-CCE MEA to retain water even at high temperatures, which leads to the formation of large peaks at various active areas. In a numerical manner, the ECSA as a function of the cell temperature was estimated, as shown in Figure 3.34.b. The ECSA decreases with increasing temperature, which could be due to increase resistivity. However, at 95 °C cell temperature, the asymmetric SS-CCE MEA could still access most of the active areas (ca. 74%). This confirms that the SS-CCE CL has the ability to retain water even at high temperatures.

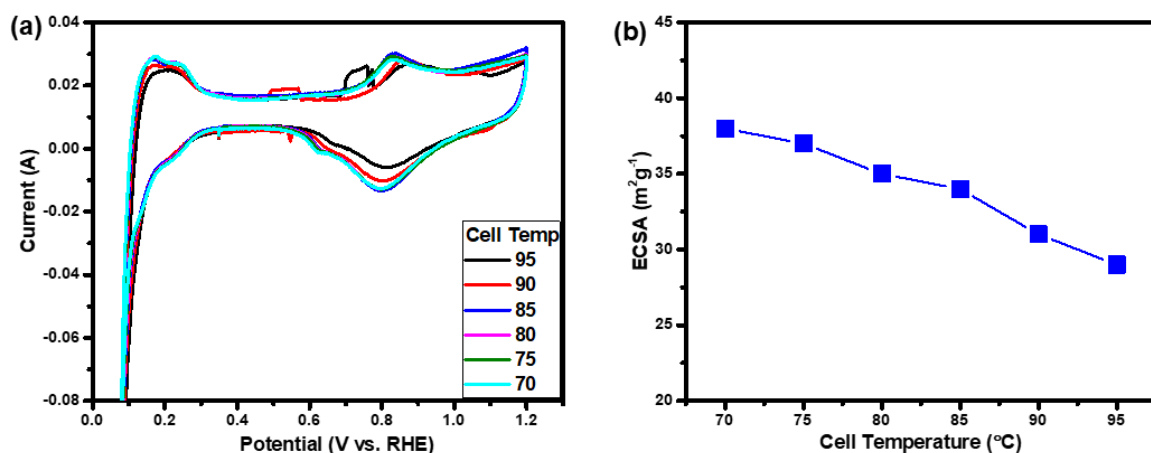


**Figure 3.34** (a) CVs ( $20 \text{ mV s}^{-1}$ ) and (b) ECSA obtained for the asymmetric SS-CCE MEA at various cell temperature from 70 °C to 95 °C under  $H_2/N_2$  gas feeds. Both the anode and cathode gases were humidified at 100% RH. Backpressure applied to both sides was 10 psig.

### 3.3.4.3 Effect of the cell temperature on the hydrogen crossover

The HOR current as a function of the cell temperature is shown in Figure 3.35. The HOR current increases with temperature as shown in Figure 3.35.b. This could be due to the decrease of the mechanical strength of the membrane, which could be the formation of pin hole with increasing temperature.<sup>[72,75]</sup> This indicates that H<sub>2</sub> permeation as a function of the cell temperature is significantly influenced by the H<sub>2</sub> diffusion coefficient as to solubility coefficient.<sup>[71]</sup> Table 3.5 shows the calculated the Pt ECSA and the H<sub>2</sub> crossover rate at various temperatures.

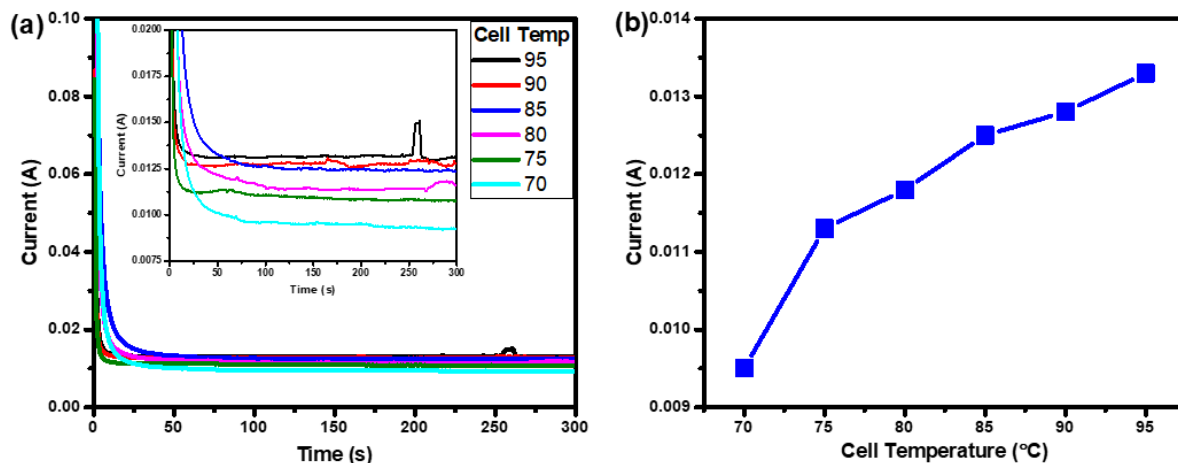


**Figure 3.35** (a) Chronoamperogram and (b) HOR current measured with asymmetric SS-CCE MEA at a potential of 0.5 V vs RHE under H<sub>2</sub>/N<sub>2</sub> at various cell temperature from 70 to 95°C. The anode and cathode were fixed at 100% RH. The backpressure on both sides was 10 psig.

**Table 3.5 Summary of measured Pt ECSA and H<sub>2</sub> crossover rate as a function of cell temperature**

Cell temperature (°C)	Pt ECSA (m <sup>2</sup> g <sup>-1</sup> )	H <sub>2</sub> crossover rate (nmol cm <sup>-2</sup> s <sup>-1</sup> )
70	38.12	10.3
75	36.90	12.0
80	34.20	12.2
85	33.80	13.0
90	31.11	13.3
95	29.60	14.0

#### **3.3.4.4 Effect of the cell temperature on conductivity of the asymmetric SS-CCE MEA**

Figure 3.36 shows Nyquist and capacitance plots for the asymmetric SS-CCE MEA as a function of the temperature. The slopes of the plots decrease with the cell temperature, indicating the variations in the ionic resistivity. The high frequency region of the Nyquist plot was expanded, as shown Figure 3.37. In here, the Warburg length increases with temperature indicating large ionic resistances. This could be because of humidification at various temperatures. The increase in temperature (> 80 °C) decreases the water-sorption properties of the membrane (Nafion), thereby increasing the ionic resistances.<sup>[72]</sup> This agrees well with the CV experiments where the ECSA decreases with temperature.

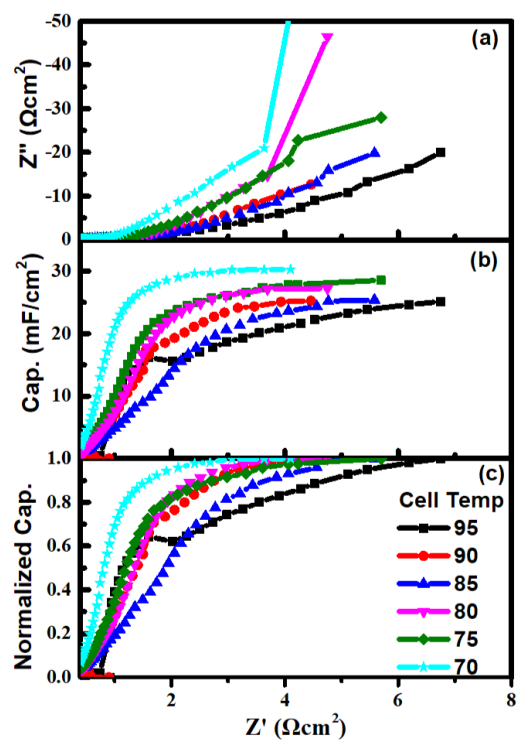


**Figure 3.36** Presents the Nyquist (a) and capacitance plots (b&c) obtained with the asymmetric SS-CCE MEA as a function of the cell temperature under  $H_2/N_2$  gas feeds. The anode and cathode gases were humidified at 100% RH. DC bias potential of 0.425 V was applied. Backpressure of 10 psig was applied on both sides.

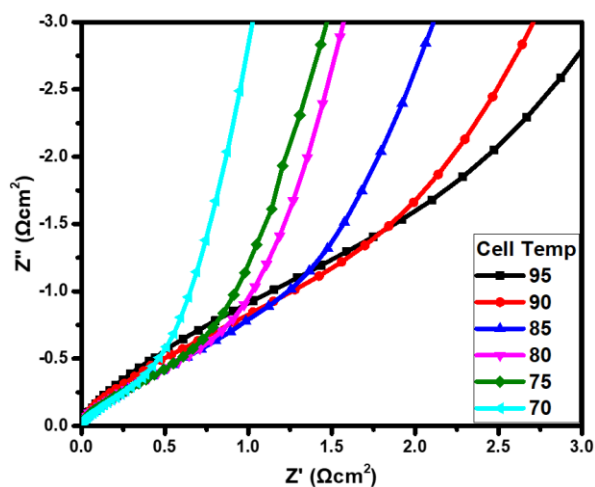


**Figure 3.37** Expansion of the high frequency region of the Nyquist plot.

The ionic resistivity changes can also be seen in the capacitance plots shown in Figure 3.36.b. From the plots, less steep slopes were observed as the temperature increases. This shows that the ionic resistances increase with the cell temperature. This could be explained by the increase contact resistance of the CL and the membrane due to dehydration.<sup>[75,80]</sup> Figure 3.36.c shows the normalised capacitance plots for further analysis. It can be deduced that the normalised capacitance for various operating temperatures are approximately the same. The large ionic resistances associated with increasing temperature could be due to deformation of the MEA structure.<sup>[75,80]</sup>

Figure 3.38 represents the  $R_M$ ,  $R_\Sigma$  and the limiting capacitance as a function of the cell temperature. The  $R_M$  was seen to increase with temperature indicating increased proton resistivity in the membrane. It was seen that  $R_\Sigma$  also increases with the temperature suggesting increase ion transport resistance in the CL layers. This accounted for the decrease of the limiting capacitance with the cell temperature. This means that increasing the cell temperature could had influence the ion migration in the MEA structure.

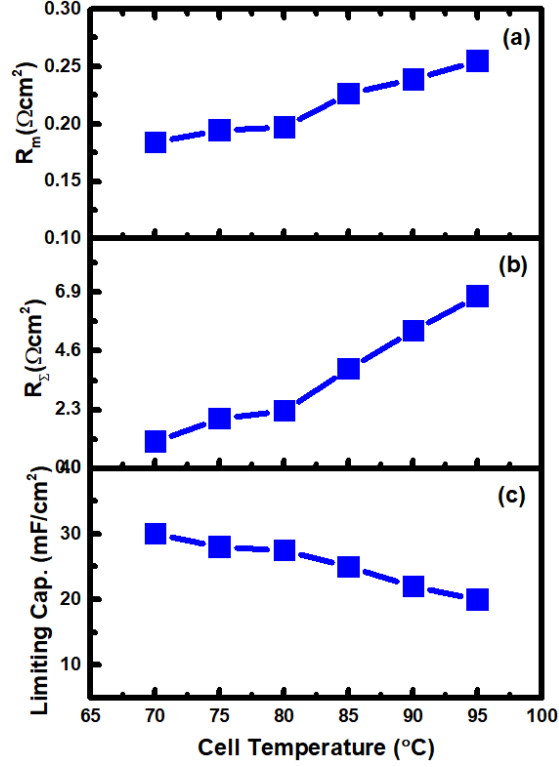


**Figure 3.38** (a) Membrane resistance (b) total ionic resistance and (c) limiting capacitance of the asymmetric SS-CCE MEA as a function of the cell temperature from 70 to 95 °C at 100% RH.

### 3.4 Comparison between the NBE and SS-CCE-based MEAs

#### 3.4.1 Fuel cell performances comparison between the MEA configurations

Figure 3.39 shows the peak power density comparison of the symmetric NBE, a symmetric SS-CCE and asymmetric SS-CCE MEA as a function of the cathode RH. The symmetric NBE MEA decreases with cathode RH from 100% to 20%. This is because the water content in the cathode electrode gradually decreases as the RH level decreases. In contrast, the symmetric SS-CCE MEA shows approximately constant peak power density values indicating that the SS-CCE has minor dependence on the RH. This is not surprising because both the anode and cathode CL contains hygroscopic material ( $\text{SiO}_2$ ), which could

increase the electrode water uptake. However, too much water is also a detriment to a good PEM fuel cell performance, which would increase mass transfer resistances. With the asymmetric SS-CCE MEA, the performance showed minor dependence on the cathode RH and better performance than the symmetric MEA. This improvement may be attributed to the effect of relative humidity and the asymmetric configuration of the electrodes. These could improve mass transport process, resulting in higher performances than the symmetric SS-CCE MEA.

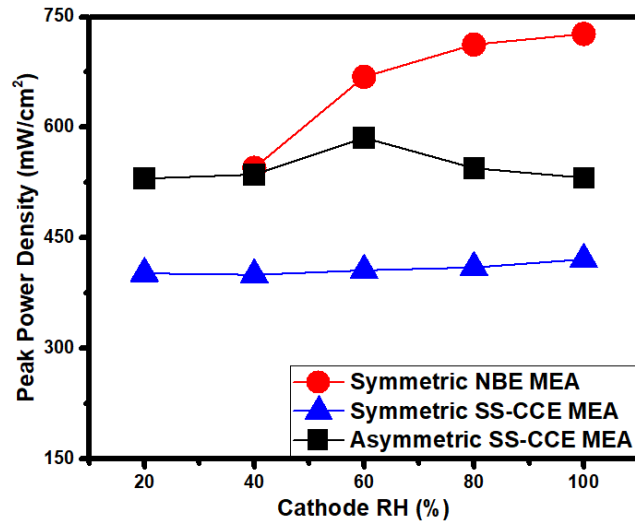


**Figure 3.39** Peak power density comparison of the symmetric NBE, a symmetric SS-CCE and asymmetric SS-CCE MEA as a function of the cathode RH at 85 °C.

Figure 3.40 compares the peak power density of the symmetric NBE, symmetric SS-CCE and asymmetric SS-CCE MEA as a function of the cell temperature. The performance of the symmetric NBE MEA increases with increasing cell temperature from 70 °C to 85 °C until it declines at 90 °C and 95 °C. The loss in performance is due to the

NBE inability to absorb water at temperature above 85 °C. In contrast, the symmetric SS-CCE shows the same performance at all cell temperatures indicating their ability to retain water under hot conditions. However, the performance was poor due to flooding. Lastly, the asymmetric SS-CCE MEA shows a gradual increase in peak power density with the cell temperature and maintains better performances at higher cell temperatures compared to the symmetric MEAs. This may be attributed to an enhanced back diffusion of water from the SS-CCE cathode CL to the Nafion anode CL, which keeps the membrane hydrated at higher temperatures.

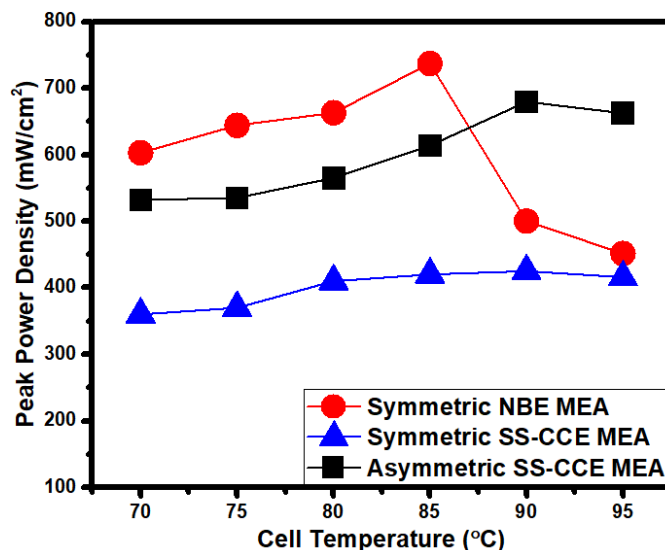


**Figure 3.40** Peak power density comparison for the symmetric SS-CCE, symmetric NBE and asymmetric SS-CCE MEA as a function of cell temperature at 100% RH.



### 3.4.2 EIS data comparison

#### 3.4.2.1 Comparison between the conductivity of the symmetric NBE and asymmetric SS-CCE MEA for various cathode RH

Figure 3.41 shows a comparison of the  $R_M$ ,  $R_\Sigma$ , and limiting capacitance values for the symmetric NBE and asymmetric SS-CCE MEA as a function of the cathode RH. In both MEAs, the  $R_M$  increased as the cathode RH decreases. However, it is worth noting that the asymmetric MEA displayed lower  $R_M$  values compared to symmetric NBE. This is because water retained by the SS-CCE at the cathode is able to keep membrane hydrated through a back diffusion process.<sup>[38]</sup> It can also be seen that the total ionic resistances for both electrodes were approximately the same as the cathode RH decreases from 100% to 40%.

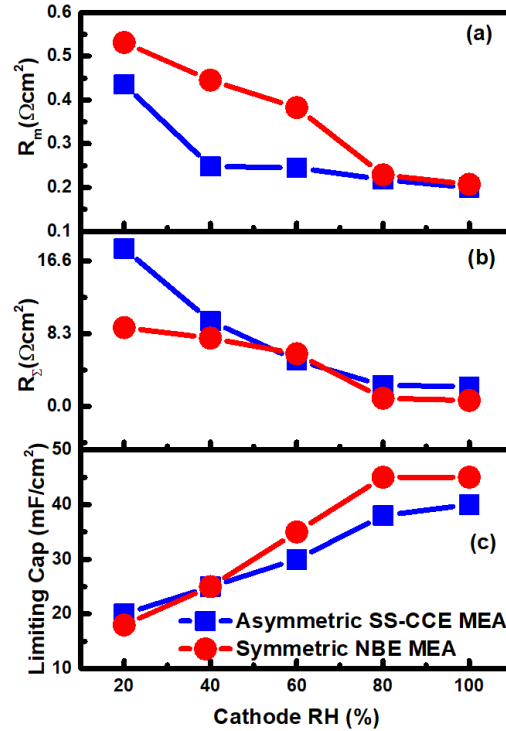


**Figure 3.41** Comparison of the (a) membrane resistance (b) total ionic resistance and (c) capacitance of the symmetric NBE and the asymmetric SS-CCE MEA as a function of the cathode RH at 80 °C.

The limiting capacitance shows similar response under RH, which decreases with decreasing cathode RH. However, the cathode RH seems to have no significant impact on the asymmetric SS-CCE MEA, which displayed an identical conductivity as the cathode RH decreases from 100 to 20%. This could be attributed to water retention properties of the asymmetric SS-CCE MEA.

#### **3.4.2.2 Comparison between the conductivity of the symmetric NBE and asymmetric SS-CCE MEA for various cell temperature**

The various resistances associated with the symmetric NBE and asymmetric MEA were compared at different cell temperatures, as shown in Figure 3.42. It was found that  $R_M$  values for the asymmetric MEA were lower than the symmetric NBE MEA, indicating a well hydrated membrane at all the cell temperatures. However,  $R_\Sigma$  values of the asymmetric MEA were higher than symmetric NBE, which could be due to the superior proton conduction of the Nafion ionomer.<sup>[72]</sup> Although, the asymmetric MEA demonstrated higher ionic resistance compared to the symmetric NBE, it is worth noting that the limiting capacitance displayed by the asymmetric MEA was slightly higher than that for the symmetric NBE. This may be attributed to the large active area presented by the asymmetric MEA due to its ability to retain water at the membrane/electrode interface in a low water environment.

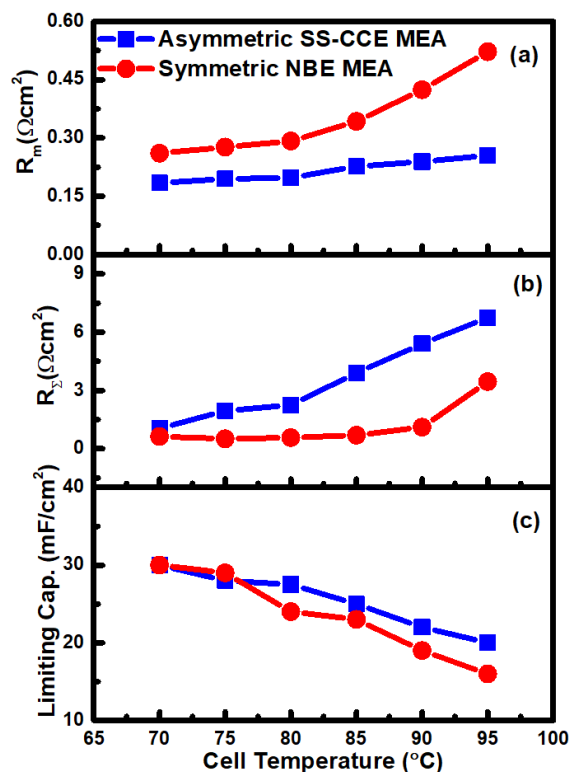


**Figure 3.42** (a) Membrane resistance, (b) total ionic resistance, and (c) limiting capacitance comparison of the NBE and the asymmetric SS-CCE MEA as a function of the cell temperature at 100% RH.

### 3.5 Diagnosing the Degradation of the NBE and SS-CCE catalyst layers

#### 3.5.1 Potential cycling durability test

Potential cycling is an accelerated degradation test tool for assessing degradation pathways in PEM fuel cell electrodes.<sup>[56,81–88]</sup> In this study, the anode is fed with  $\text{H}_2$  ( $70 \text{ mL min}^{-1}$ ) serving as the counter and reference electrode whereas the cathode serves as working electrode fed with  $\text{N}_2$  ( $100 \text{ mL min}^{-1}$ ). The cathode potential is swept back and forth between an initial voltage of 0.08 V and an upper limit voltage of 1.20 V with a scan rate range between  $50 - 200 \text{ mV s}^{-1}$ . The potential durability cycling protocol was adopted from previous work from our laboratory.<sup>[27]</sup> Figure 3.43 shows typical CVs of the PEM

fuel cell working electrode (cathode) as a result of a potential cycling from 0.08 to 1.20 V vs RHE (anode).

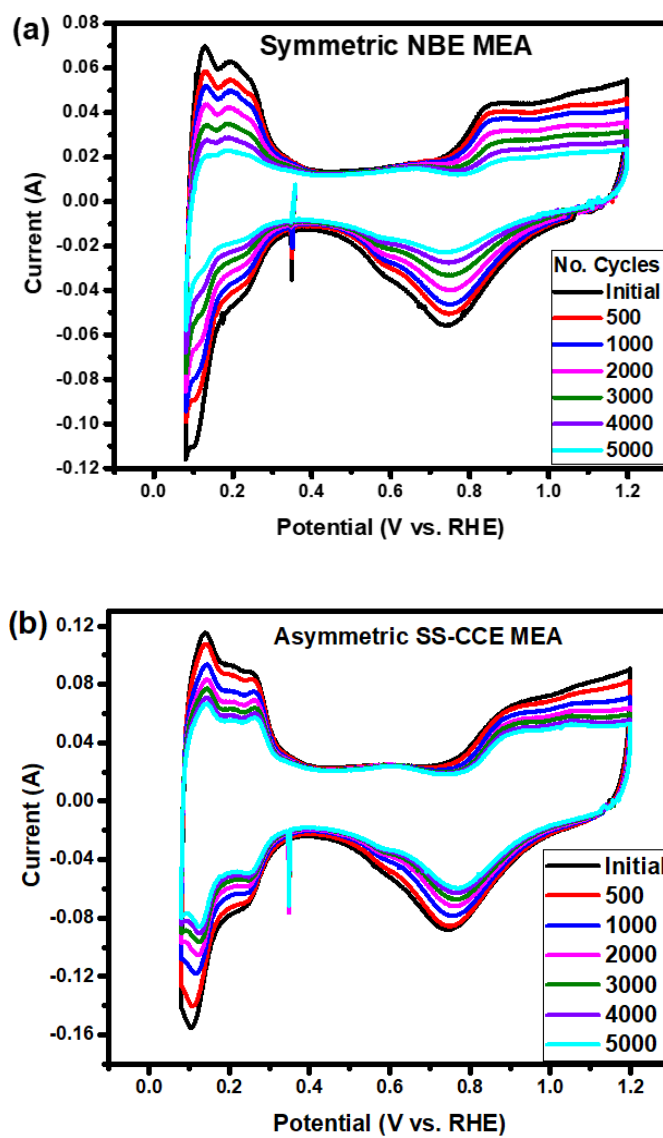


**Figure 3.43** CVs recorded at different cycles for (a) NBE MEA and (b) Asymmetric SS-CCE MEA at 30 °C under H<sub>2</sub>/N<sub>2</sub>.

After the first 1000 cycles, both electrodes exhibited a sharp decrease in the  $H_2$  adsorption/desorption (0.08 – 0.40 V) and Pt oxidation/reduction (0.70 – 1.20 V) regions. This is because fresh CL has smaller particles with low interfacial energy and would be subjected to an initial agglomeration and/or particle growth for a variety of conditions. However, the degradation in these regions was much slower between 2000 to 5000 cycles indicating that the particles have reach a more thermodynamically stable state wherein the surface to area ratio is minimized.<sup>[89]</sup> The stability was more evident for the asymmetric SS-CCE MEA compared to the symmetric NBE MEA.

To obtain numerical insight ECSA values were estimated and plotted against the number of cycles as shown in Figure 3.44.

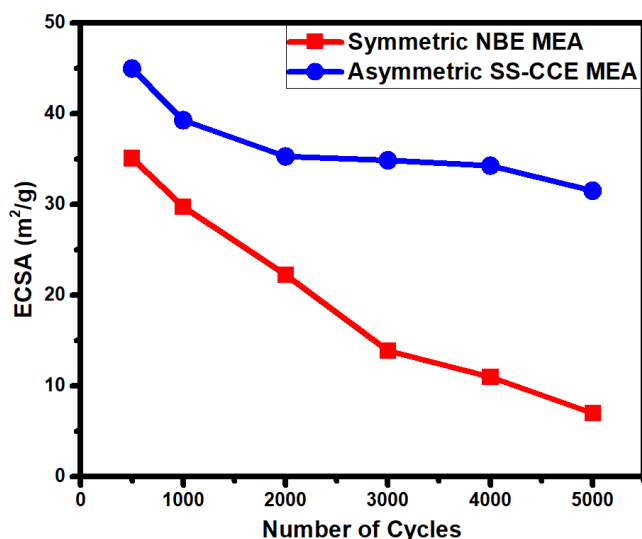


**Figure 3.44** Estimated ECSA from the CVs (Figure 3.44) as a function of the number of cycles

It was found that the symmetric NBE losses ca. 85% of its initial ECSA while the asymmetric SS-CCE MEA ca. 50% after the 5000 cycles. The decrease in ESCA could be due to Ostwald ripening, dissolution, or agglomeration of Pt particles.<sup>[56,88]</sup> Since the same

commercial Pt/C (Premetek) was employed in both electrodes, the durability of the SS-CCE employed at the cathode side of the asymmetric SS-CCE MEA can be attributed to the presence of the organosilicate ionomer in the Pt/C matrix, which tends to protect the Pt and C from further deterioration<sup>[27]</sup>.

### 3.5.2 EIS measurements during ADT

EIS is a useful diagnostic tool for investigating possible degradation pathways in the electrodes, including Pt dissolution/Ostwald ripening and ionomer degradation.<sup>[89],[90]</sup> EIS experiments were performed immediately after every 500 CVs were recorded. A perturbation voltage of 5 mV was applied at a DC bias of 0.425 V from an initial frequency of 100 kHz to a final frequency of 0.1 Hz. Figure 3.45 shows the Nyquist and capacitance plots for the symmetric NBE and asymmetric SS-CCE MEA.

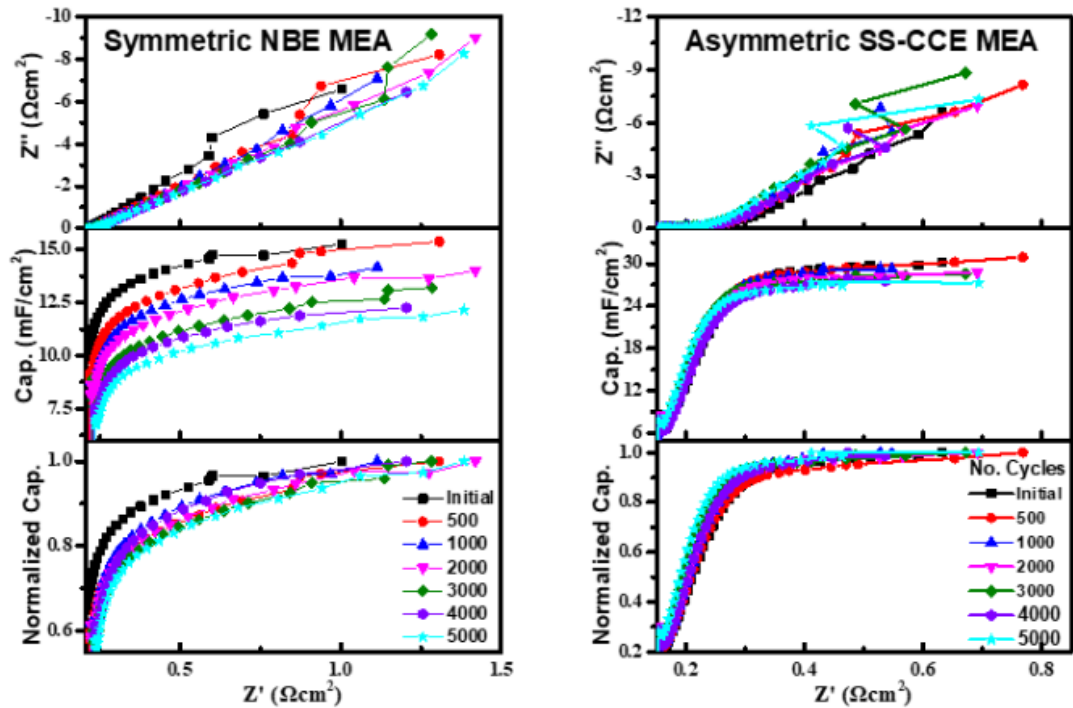


**Figure 3.45** Comparison of the EIS data of the symmetric NBE MEA (left) and the asymmetric SS-CCE MEA (right) collected under  $H_2/N_2$  at dc bias potential 0.425 V.

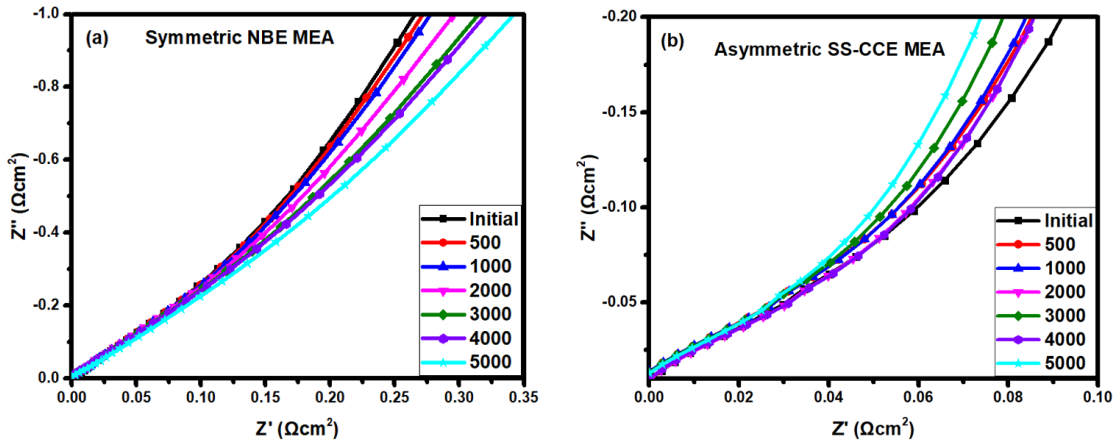


**Figure 3.46** Expansion of the high frequency region of Figure 3.45.a of the (a) symmetric NBE (b) asymmetric SS-CCE MEA

The Nyquist plots representing each electrode suggest a small change in the total ionic resistance,  $R_{\Sigma}$  upon cycling as shown in the Figure 3.36.

Figure 3.45.b shows capacitance plots obtained for each MEA at various cycles. For the symmetric NBE, it can be seen at the mid frequency region that the slope of each plot decreases with number of cycles, indicating an increased in resistivity. This be due to the deterioration of the Nafion ionomer in the electrode, which could lead to Pt dissolution/agglomeration.<sup>[88]</sup> In the case of the asymmetric SS-CCE MEA, the slope of each plot is very similar, which indicates similar active surface area for conductivity. In addition, the capacitance plots were normalized by dividing through with the maximum capacitance value. In Figure 3.45.c, the normalized capacitance slopes related to the asymmetric SS-CCE MEA were similar, indicating virtually no change in the electrode conductivity. This may be due to the strong electronic interaction between silicate and Pt/C particles, which could slow Pt growth and deterioration of the CL.<sup>[27]</sup> This behavior was not observed for the symmetric NBE, which suggest that the Nafion, acting as a binder,

degrades upon cycling where the possible degradation pathways could be agglomeration, dissolution and deposition of Pt particles in the solid electrolyte membrane. The later has been confirmed by Yasuda et al using TEM analysis.<sup>[88]</sup>

### 3.6 Pre and Post-test Comparison

#### 3.6.1 Fuel cell analysis

Fuel cell pre and post-testing results for the symmetric NBE and asymmetric SS-CCE MEA were compared to determine the performance change after the accelerated stress test (AST). Figure 3.47 shows the MEAs performance before and after a potential sweep with hydrogen and oxygen reactants.

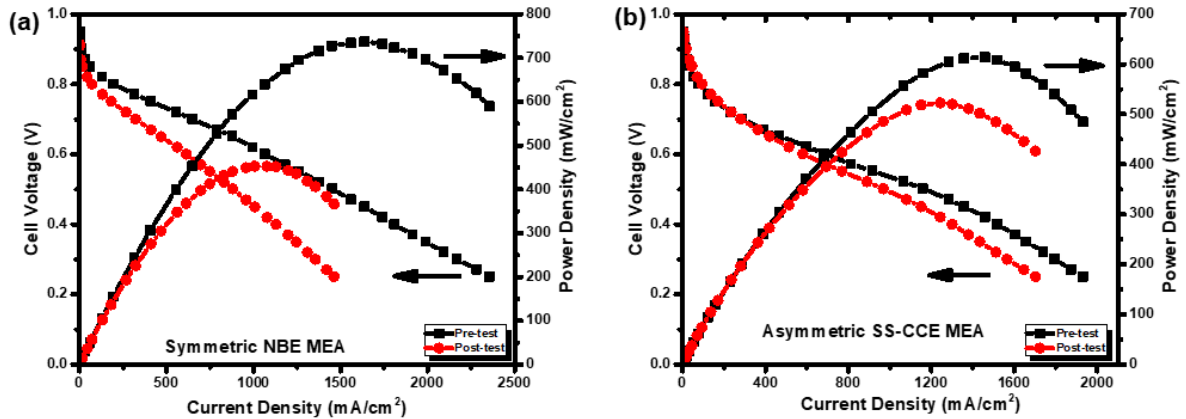


**Figure 3.47** Pre and Post-tests performance curves for the (a) symmetric NBE and (b) Asymmetric SS-CCE MEA under  $H_2/O_2$  at 85 °C cell temperature; anode and cathode kept at 100% RH; backpressure on both sides is 10 psig.

There was no significant difference in the initial MEA performance for either electrode. However, after the 5000 potential sweep tests, the performance of the symmetric NBE MEA declined significantly (ca. 40%) showing a decrease in the initial peak power



density from  $740 \text{ mW cm}^{-2}$  to  $440 \text{ mW cm}^{-2}$  after the AST. This observation agreed with the results of the CVs and EIS shown in Figure 3.43.a and 3.46 respectively. This can be attributed to increased ionic resistivity due to deterioration of the catalyst layer.

In the case of the asymmetric SS-CCE MEA, the peak power density exhibited a loss of ca. 15% from  $610 \text{ mW/cm}^2$  to  $510 \text{ mW/cm}^2$  after 5000 test cycles. This gives clear evident that SS-CCE are more durable than the NBE catalyst layers.

### 3.6.2 TEM analysis

AST causes structural changes in the CLs as to Pt growth and detachment.<sup>[91]</sup> These changes always lead to the loss of the active surface area of the catalyst layer, which could be associated with four major degradation pathways: (1) Pt dissolution/Ostwald ripening, (2) Pt detachment and agglomeration (3) carbon corrosion, and (4) degradation of the ionomer.<sup>[90,91]</sup> Figure 3.48 shows TEM images of the NBE and SS-CCE catalysts before (left) and after (right) test and their corresponding particle size distributions.

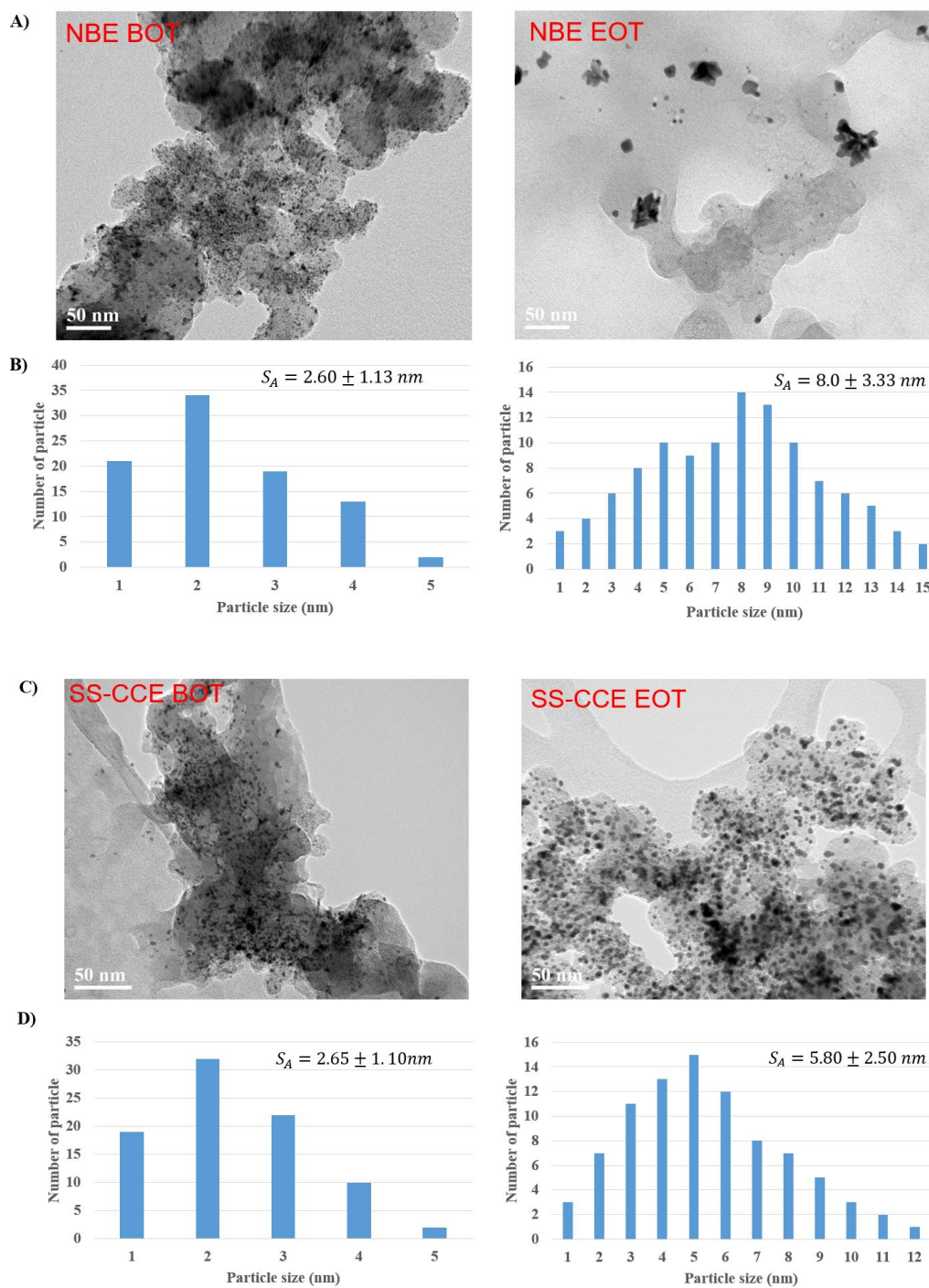


**Figure 3.48** TEM analysis of the NBE (A&B) and SS-CCE (C&D) catalyst and their corresponding size distribution. The analysis was performed using a Jeol 2010F field emission gun (FEG) operated at 200 kV. The microscope is equipped with an Oxford Inca EDS system.

For the fresh catalysts (left images), a uniform dispersion of fine Pt particles was found for the NBE and SS-CCE catalyst. The average particle size for the NBE and SS-CCE catalysts was estimated to be 2 – 3 nm using ImageJ software.

After the AST, images of both catalysts, showed that the Pt particles became larger after the 5000 potential sweep cycles. This was not a surprise because potential cycling has proven to be the main cause of coarsening and coalescence of Pt particles in the catalyst.<sup>[91]</sup> It was found that the original size of the Pt particles changed from ca. 2 – 3 nm to an average size of 7.40 nm for the NBE and 4.30 nm for the SS-CCE catalyst, as shown in Figure 3.48 C and D respectively. These observations show that Pt particles agglomerate at the cathode catalyst layer. Thus, smaller catalyst particles tend to migrate and deposit into/onto one another to form larger particles.<sup>[89]</sup> This leads to loss of surface area of the catalyst layer. After the AST, the particle size distribution was uniform for the SS-CCE but the NBE was not uniform and included large particles. This means that the starting material (Pt/C) benefits from the mechanical characteristics of the organosilane monomers, which slow the degradation of the catalyst. As a result, the SS-CCE catalyst shows better stability against potential sweep test.

### **3.6.3 Energy dispersive X-ray analysis**

The durability of the NBE and SS-CCE catalysts was further investigated by the EDX technique. Figure 3.49 and 3.50 show the EDS images of the NBE and the SS-CCE catalysts respectively.

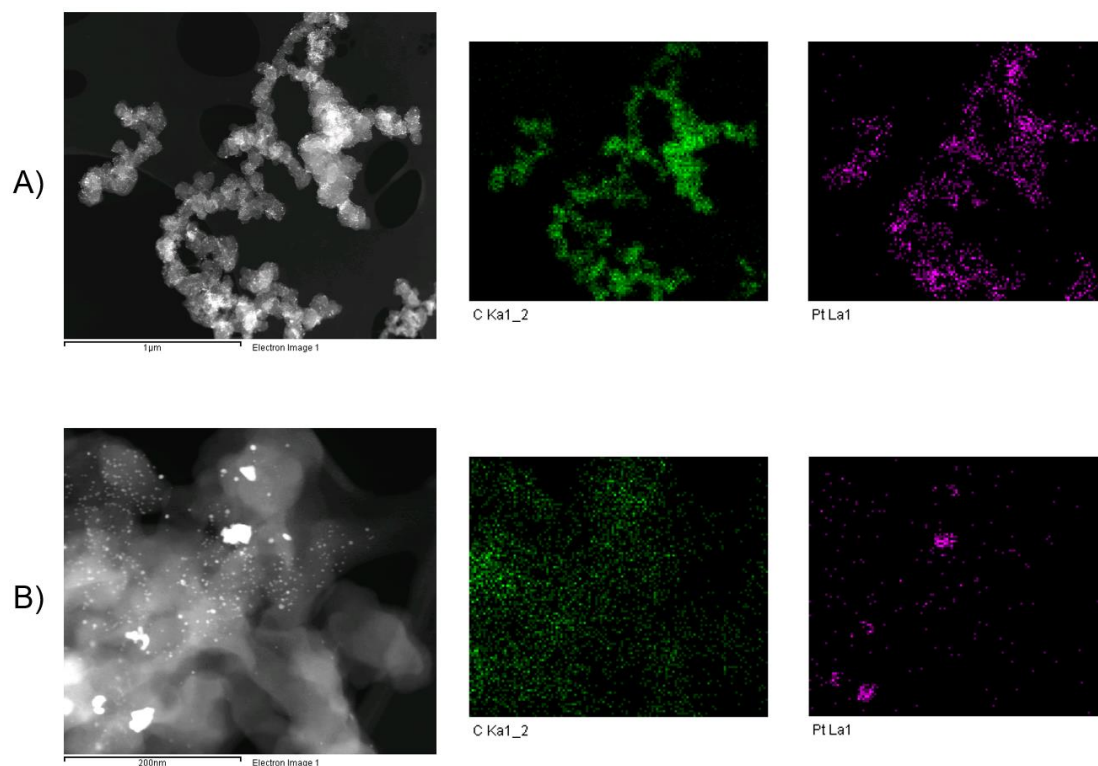


**Figure 3.49** Postmortem EDX analysis of the NBE catalyst layer: A) Fresh catalyst B) End-of-test analysis using a Jeol 2010F field emission gun (FEG) operated at 200 kV. The microscope is equipped with an Oxford Inca EDS system.

In the image A (Figure 3.49), fine particles and good carbon and platinum metal dispersion was obtained for fresh NBE catalyst. However, the post-mortem EDX image in the image B shows clumps of the Pt particles due to agglomeration. In the case of the SS-CCE catalyst (Figure 3.50), the elemental compositions (i.e., C, Pt, S, and Si) remain approximately the same after the durability test (image B) when compared to the fresh catalyst (image A). These observations confirm that the SS-CCE catalyst are more stable than the NBE catalyst.

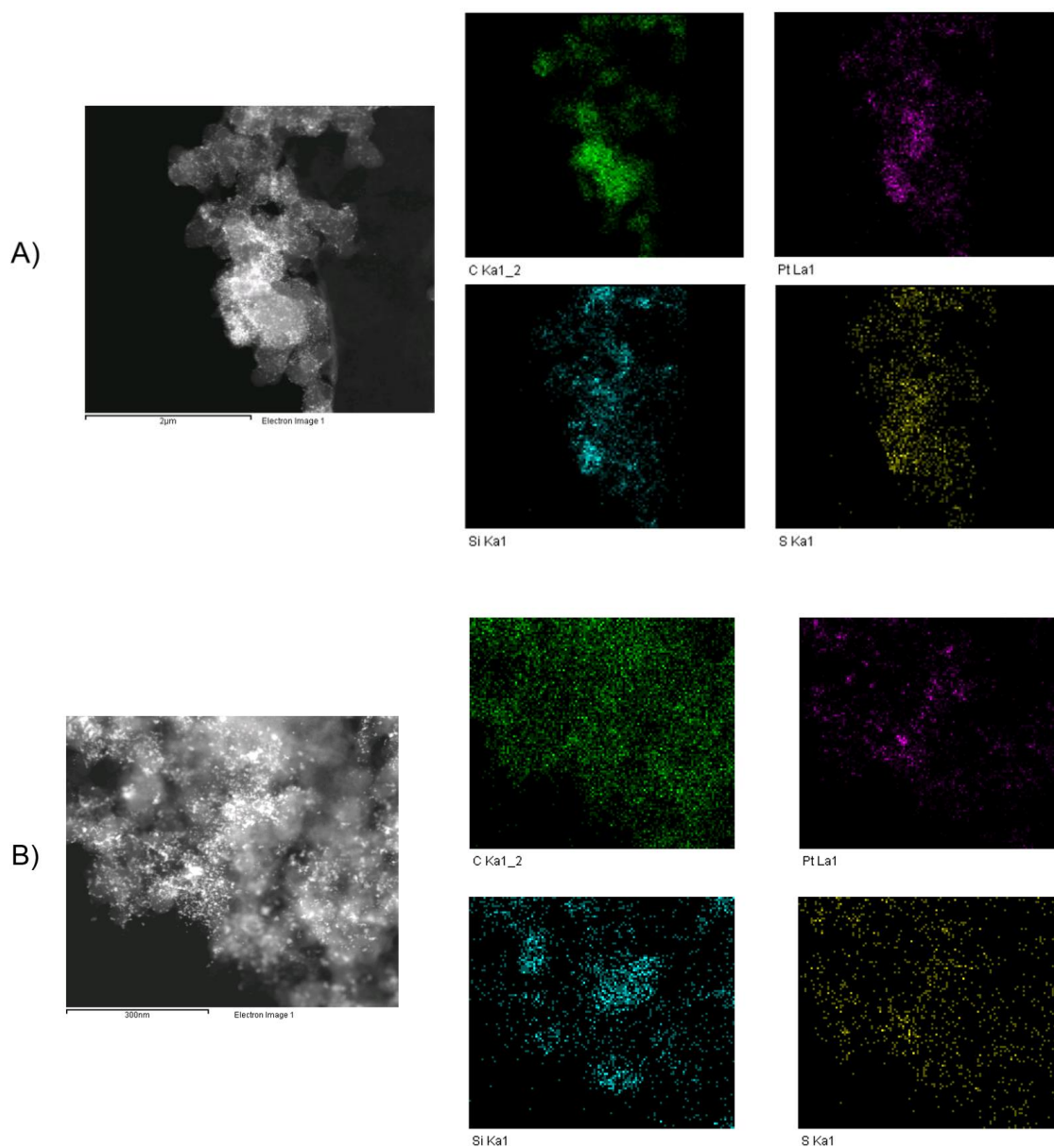


**Figure 3.50** Post mortem EDX analysis of the SS-CCE catalyst layer: A) Fresh catalyst B) End-of-test analysis using a Jeol 2010F field emission gun (FEG) operated at 200 kV. The microscope is equipped with an Oxford Inca EDS system.

## **Chapter 4 Conclusions and future work**

## 4.1 Conclusions

In this work, an in-depth material and electrochemical characterizations have been conducted on the SS-CCE catalyst layers as well as NBE catalyst layers. One of the main contributions of this work is to understand how the SS-CCE catalyst layers retain water under dry/hot conditions.

Material characterizations include XRD and TGA confirmed the presence of silicate in the 20% Pt on Vulcan XC-72 (carbon) matrix showing a loading of ca. 35%, which is the optimum loading reported in our lab. The BET and the SEM revealed a high surface area and porosity of the SS-CCE catalyst compared to the NBE catalyst.

The focus of the thesis is the influence of relative humidity and cell temperature on the performance. A single cell testing was performed with different MEA configurations including the symmetric NBE, a symmetric SS-CCE and an asymmetric MEA. It was found that the symmetric NBE MEA performs at its best when fully hydrated (i.e., 100% – 80%) while the symmetric SS-CCE MEA performance was hindered by flooding. However, at low RHs the symmetric SS-CCE MEA showed improved performance as the symmetric NBE MEA drops in performance, which could be due to reduced water content (dehydration). On the other hand, the asymmetric SS-CCE MEA showed excellent performance for all the ranges of the cathode RHs from 20% to 100% while demonstrating optimum performance at 85 °C in the mid cathode RH (i.e., 60%).

The temperature effects on these MEAs showed that the symmetric NBE MEA was subject to performance loss at temperatures above 85 °C due to the dehydration of the MEA components. In contrast, the symmetric SS-CCE MEA showed a stable, but poor performances compared to the symmetric NBE MEA and the asymmetric SS-CCE MEA.

This was explained by Vengatesan *et al.* [77] that employing silica at the anode CL can limits the electro-osmotic drag of the protons from the anode to the cathode by strongly adhering water molecules around the silica. As a result, the anode compartment becomes flooded, limiting the charge transfer kinetics from the anode to the cathode. In the case of the asymmetric SS-CCE MEA, the performance showed significant increased with increasing the cell temperature. Since the anode is always subjected to dehydration at high temperatures, the SS-CCE employed at the cathode side can hydrate the membrane through a back-diffusion processes, hence enhancing performance.

It was also found that the performance under air oxidant could be limited by the high flow rate of the air at the cathode side. The high flow rate was seen to increase the rate of evaporation in the cell. These observations were more evidence at high temperatures (90 °C and 95 °C) and low relative humidities (40% and 20%).

The impedance response gave low  $R_M$  values for the asymmetric SS-CCE MEA compared with the symmetric NBE MEA at all operation conditions. This confirmed the hydrophilic nature of the SS-CCE cathode CL, whereby water molecules could be retained at the membrane/catalyst interface for hydration processes. It was also seen that, regardless of the increasing  $R_\Sigma$  values of the asymmetric SS-CCE MEA with temperature and low RH, the polarization curves showed better performances at those extreme conditions.

The durability of the NBE and the SS-CCE CLs were studied *in situ* by potential cycling conditions at 30 °C. It was found that the extent of the degradation of the SS-CCE CL was far less than that of the NBE CL, where ECSA losses of about 50% and 85%, respectively, were measured after 5000 cycles. The initial performance of the SS-CCE cathode CL was lower than that of the NBE cathode CL. After the 5000 cycles, the



asymmetric SS-CCE MEA showed the highest MEA performance. This result confirmed that the organosilane ionomer improved the stability of the 20% Pt/C compared to the Nafion ionomer by slowing the degradation of the CL. Moreover, the post mortem analysis by the TEM and the EDX confirmed that the deterioration of the NBE cathode CL was far worse than the SS-CCE cathode CL. Thus, the Pt agglomeration was severe for the NBE cathode CL. Therefore, the 20% Pt catalyst modified with the organosilane monomers (i.e, TEOS and TPS) has improved the stability of the electrode.

Taken together, these findings highlight the role of employing SS-CCEs in the PEM fuel cell for high temperature and low relative humidity operation. Therefore, the SS-CCE possible of cutting down the cost of electrode materials and could reduce power losses due to high humidification.

## **4.2 Future work**

The future extension of this work should focus on a new approach of synthesizing the sulfonated silica ceramic electrode. Instead of the conventional sol-gel approach, the hydrothermal technique<sup>[92]</sup> could be utilized for the preparation of the SS-CCE catalyst ink. This technique may be the best approach for preparing SS-CCE for high temperature PEM fuel cell operation because it enhances the distribution of the silicate network within the Pt/C matrix, which further enhance the catalyst activity and the durability of the electrode.<sup>[92]</sup> Alipour *et al* prepared SS-CCE using a hydrothermal technique and obtained good and stable performance compared with the conventional sol-gel technique.<sup>[92]</sup> Therefore, exploring the influence of relative humidity and temperature on SS-CCE made by a hydrothermal process would be of interest.

The poor performance of the symmetric SS-CCE MEA is a vital issue that needs further investigation. Future work should concentrate on how to eliminate losses due to concentration gradient (flooding). Therefore, it would be interesting to probe the influence of mesoporous carbon nanoparticles as a catalyst support for the sulfonated silica carbon electrodes. This could create large and more pores for effective mass transport processes within the electrode.

Concerning the high ionic resistance associated with the SS-CCE catalyst layers, the MEA fabrication could be optimized to minimize ohmic and charge transfer resistances. The following ideas are suggested for the future extension of the work.

The 20% Pt on Vulcan XC-72 starting material could be replaced with a 40% Pt on Vulcan XC-72. The high metal loading in the Pt/C matrix would reduce the thickness of the catalyst layers. This may be a better approach to prepare SS-CCE based MEA because the catalyst layer can be made thinner, ionic transport resistances can be reduced and improve performance under various conditions.

Lastly, considering the gas diffusion electrode configuration, it could be possible that the membrane delaminates from the catalyst layer bonded on the gas diffusion layer under dry and hot conditions, which often leads to poor performance. Therefore, it could be interesting to consider fuel cell testing on SS-CCE MEA prepared using a catalyst coated membrane (CCM) technique. With this technique, the catalyst ink is deposited directly onto the membrane as a result, a thinner catalyst layer can be made, and the contact resistances associated the catalyst layer/membrane interface could be decreased. In addition, the SS-CCE CL adhered on the membrane would be able to retain water for the membrane/catalyst hydration under hot and dry conditions.

### 4.3 References

- [1] International Energy Agency, “Global Energy & CO<sub>2</sub> Status Report 2019,” can be found under <https://www.iea.org/geco/>, **2019**.
- [2] S. Sundaram, D. Benson, T. Mallick, *Solar Photovoltaic Technology Production: Potential Environmental Impacts and Implications for Governance*, Academic Press, **2016**.
- [3] TM Letcher, *Acad. Press* **2019**, 3–15.
- [4] P. Alstone, D. Gershenson, D. Kammen, *Nat. Clim. Chang.* **2015**, 5, 305.
- [5] S. Chalk, J. Miller, *J. Power Sources* **2006**, 159, 73–80.
- [6] The Canadian Hydrogen and Fuel Cell Association, “The Need for Clean Energy,” can be found under <http://www.chfca.ca/education-centre/the-need-for-clean-energy/>, **2019**.
- [7] C. and S. S. Rayment, *Dep. Aerosp. Mech. Eng. Univ. Notre Dame, IN*, 46556 **2003**, 11–12.
- [8] F. Barbir, *PEM Fuel Cells : Theory and Practice*, Academic Press, **2013**.
- [9] B. James, *2018 Cost Projections of PEM Fuel Cell Systems for Automobiles and Medium-Duty Vehicles Question and Answer Motivation and Outline*, **2018**.
- [10] M. Huang, H. Yang, *J. Libr. Inf. Stud.* **2013**, 11, 1–24.
- [11] J. Lobato, H. Zamora, P. Cañizares, J. Plaza, *J. Power Sources* **2015**, 288, 288–295.
- [12] T. H. X Ding, S Didari, TF Fuller, *Electrochem. Soc.* **2012**, 159, B746–B753.

- [13] J. M. Ramani, V. I. J. A. Y., Kunz, H. R., & Fenton, *J. Memb. Sci.* **2004**, 232, 31–44.
- [14] C. Yang, P. Costamagna, J. Srinivasan, S. Benziger, *J. Power Sources* **2001**, 103, 1–9.
- [15] S. Vengatesan, H. Kim, S. Lee, E. Cho, ... H. H.-I. J. of, undefined 2008, *Internaltional J. Hydrog. Energy* **2008**, 33, 171–178.
- [16] C. Ke, X. Li, Q. Shen, S. Qu, Z. Shao, B. Y. Yi, *Int. J. Hydrogen Energy* **2011**, 36, 3606–3613.
- [17] I. Choi, K. Lee, S. Ahn, O. Kwon, J. Kim, *Catal. Commun.* **2012**, 21, 86–90.
- [18] H. Su, L. Yang, S. Liao, Q. Z.-E. Acta, undefined 2010, *Electrochim. Acta* **2010**, 55, 8894–8900.
- [19] H. Liang, D. Dang, W. Xiong, H. Song, S. Liao, *J. Power Sources* **2013**, 241, 367–372.
- [20] S. Hou, H. Su, H. Zou, D. Dang, H. Song, X. Li, *Int. J. Hydrogen Energy* **2015**, 40, 15613–15621.
- [21] N. Inoue, M. Uchida, M. Watanabe, H. U.- Electrochemistry, undefined 2012, *Elsevier* **2012**, 16, 100–102.
- [22] U. H. Jung, K. T. Park, E. H. Park, S. H. Kim, *J. Power Sources* **2006**, 159, 529–532.
- [23] J. Lobato, H. Zamora, J. Plaza, P. Cañizares, *Appl. Catal. B Environ.* **2016**, 198, 516–524.

- [24] J. J. I. Eastcott, A. Yarrow, KM Kaitlyn M, A. W. Pedersen, E. B. Easton, *J. Power Sources* **2012**, *197*, 102–106.
- [25] H. Su, L. Yang, S. Liao, Q. Z.-E. Acta, undefined 2010, *Elsevier* **2010**, *55*, 8894–8900.
- [26] J. Eastcott, K. Yarrow, A. P.-J. of P. Sources, U. 2012, *Elsevier* **2012**, *197*, 102–106.
- [27] R. Esfahani, H. Fruehwald, F. Afsahi, *Appl. Catal. B Environ.* **2018**, *232*, 314–321.
- [28] N. Inoue, M. Uchida, M. Watanabe, H. U.- Electrochemistry, undefined 2012, *Electrochem. commun.* **2012**, *16*, 100–102.
- [29] B. Koh, J. Yoo, E. Jang, V. Jothi, C. Jung, *Electrochem. commun.* **2018**.
- [30] S. I. Publishing, *High Temperature Polymer Electrolyte Membrane Fuel Cells*, Springer International Publishing, Cham, **2015**.
- [31] H. Su, L. Xu, H. Zhu, Y. Wu, L. Yang, S. Liao, *Int. J. Hydrogen Energy* **2010**, *35*, 7874–7880.
- [32] K Miyatake, *Encycl. Sustain. Sci. Technol.* **2012**, 6538–6565.
- [33] R. Ye, R., Henkensmeier, D., Yoon, S.J., Huang, Z., Kim, D.K., Chang, Z., Kim, S. and Chen, *J. Electrochem. Energy Convers. Storage* **2018**, *15*, 010801.
- [34] J. Zhang, H. Zhang, J. Wu, J. Zhang, J. Zhang, H. Zhang, J. Wu, J. Zhang, **2013**, 81–119.
- [35] J. S. Lu J, Tang H, Xu C, *J. Mater. Chem.* **2012**, *22*, 5810–5819.

- [36] and G. M. Litster, S., *J. Power Sources* **2004**, *130*, 61–76.
- [37] M. B. Sassin, Y. Garsany, B. D. Gould, K. E. Swider-Lyons, *Anal. Chem.* **2017**, *89*, 511–518.
- [38] J. I. Eastcott, E. B. Easton, *J. Power Sources* **2014**, *245*, 487–494.
- [39] S. Licoccia, E. Traversa, *J. Power Sources* **2006**, *159*, 12–20.
- [40] A. Rahnavard, S. Rowshanzamir, M. P. Parnian, *Energy* **2015**, *82*, 746–757.
- [41] K. Kim, K. Lee, S. Lee, E. Cho, ... T. L. journal of, undefined 2010, *Int. J. Hydrogen Energy* **2010**, *35*, 13104–13110.
- [42] I. Choi, H. Lee, K. Lee, S. Ahn, S. Lee, H. K. Kim, *Appl. Catal. B Environ.* **2015**, *168*, 220–227.
- [43] S. Hou, S. Liao, Z. Xiong, H. Zou, D. Dang, R. Zheng, *J. Power Sources* **2015**, *273*, 168–173.
- [44] M. Cho, H. Park, S. Lee, B. Lee, H. Kim, *Electrochim. Acta* **2017**, *224*, 228–234.
- [45] N. Inoue, M. Uchida, M. Watanabe, H. Uchida, *Electrochim. Acta* **2013**, *88*, 807–813.
- [46] G. Zhu, L., Li, Y., Tian, F., Xu, B., & Zhu, *Sensors Actuators B Chem.* **2002**, *84*, 265–270.
- [47] E. B. Ranganathan, S., & Easton, *Internaltional J. Hydrog. Energy* **2010**, *35*, 1001–1007.
- [48] L. Rabinovich, O. Lev, *Electroanalysis* **2001**, *13*, 265–275.

- [49] E. B. Eastcott, J. I., & Easton, *J. Electrochem. Soc.* **2015**, *162*, F764–F771.
- [50] J. Eastcott, J. Powell, A. Vreugdenhil, E. Easton, *ECS Trans.* **2011**, *41*, 853–864.
- [51] H. Wang, X. Yuan, H. Li, *PEM Fuel Cell Diagnostic Tools*, CRC Press, **2011**.
- [52] X. Yuan, C. Song, H. Wang, J. Zhang, *Electrochemical Impedance Spectroscopy in PEM Fuel Cells: Fundamentals and Applications*, Springer Science & Business Media, **2009**.
- [53] R. Carter, S. Kocha, F. Wagner, M. Fay, *ECS Trans.* **2007**, *11*, 403–410.
- [54] K. B. Oldham, J. C. Myland, *Fundamentals of Electrochemical Science*, Academic Press, **1994**.
- [55] G. Shawn, *Electrolysis. InTech* **2012**.
- [56] F. Saleh, E. Easton, *J. Electrochem. Soc.* **2012**, *159*, B546–B553.
- [57] M. Lefebvre, R. Martin, P. Pickup, *Electrochem. Solid-State Lett.* **2002**, *2*, 259.
- [58] M. Lefebvre, Z. Qi, D. Rana, P. Pickup, *ACS Publ.* **n.d.**
- [59] R. Makharia, M. Mathias, D. Baker, *J. Electrochem. Soc.* **2005**, *152*, A970.
- [60] A. Lasia, *Electrochemical Impedance Spectroscopy and Its Applications*, New York: Springer, 2014, **2014**.
- [61] E. B. Easton, P. G. Pickup, *Electrochim. Acta* **2005**, *50*, 2469–2474.
- [62] G. Li, P. G. Pickup, *Phys. Chem. Chem. Phys.* **2000**, *2*, 1255–1260.

- [63] G. Liu, Z. Yang, M. Halim, X. Li, M. Wang, J. Kim, *Energy Convers. Manag.* **2017**, *138*, 54–60.
- [64] J. Zhang, J. Wu, H. Zhang, *PEM Fuel Cell Testing and Diagnosis*, **2013**.
- [65] X. Cheng, J. Zhang, Y. Tang, C. Song, J. Shen, *J. Power Sources* **2007**, *167*, 25–31.
- [66] R. Borup, R. Mukundan, D. Spornjak, Y. Kim, *Electrochem. Soc.* **2014**, *no. 18*, 788–788.
- [67] S. Liu, J., Shin, S., & Um, *Renew. Energy* **2019**.
- [68] D. Ozen, B. Timurkutluk, K. Altinisik, *Renew. Sustain. Energy Rev.* **2016**, *59*, 1298–1306.
- [69] H. Weydahl, S. Møller-Holst, B. Børresen, *Fuel* **2008**, *180*, 808–813.
- [70] H. Xu, H. Kunz, J. Fenton, *Electrochim. Acta* **2007**, *52*, 3525–3533.
- [71] N. Truc, S. Ito, K. Fushinobu, *J. Heat Mass Transf.* **2018**, *127*, 447–456.
- [72] K. A. Mauritz, R. B. Moore, *Chem. Rev.* **2004**, *104*, 4535–4586.
- [73] M. Yoshitake, M. Tamura, N. Yoshida, *Denki Kagaku oyobi Kogyo Butsuri Kagaku* **1996**, *64*, 727–736.
- [74] R. B. Moghaddam, E. B. Easton, *Electrochim. Acta* **2018**, *292*, 292–298.
- [75] M. B. Satterfield, J. B. Benziger, *J. Polym. Sci. Part B Polym. Phys.* **2009**, *47*, 11–24.
- [76] H. Inoue, N., Uchida, M., Watanabe, M., & Uchida, *Electrochem. commun.* **2012**, *16*, 100–102.



- [77] S. Vengatesan, H. Kim, S. Lee, H. H. Cho, EA, *Internaltional J. Hydrog. Energy* **2008**, *33*, 171–178.
- [78] H. Su, L. Yang, S. Liao, Q. Zeng, *Electrochim. Acta* **2010**, *55*, 8894–8900.
- [79] J. Zhang, Y. Tang, C. Song, Z. Xia, H. Li, H. Wang, *Electrochim. Acta* **2008**, *53*, 5315–5321.
- [80] Y. Tang, J. Zhang, C. Song, H. Liu, J. Zhang, H. Wang, S. Mackinnon, T. Peckham, J. Li, S. McDermid, et al., *J. Electrochem. Soc.* **2006**, *153*, A2036.
- [81] G. Harzer, J. Schwämmlein, *J. Electrochem. Soc.* **2018**, *165*, F3118–F3131.
- [82] P. Yu, M. Pemberton, P. Plasse, *J. Power Sources* **2005**, *144*, 11–20.
- [83] D. Stevens, M. Hicks, G. Haugen, *Electrochem. Soc.* **2005**, *152*, A2309–A2315.
- [84] T. Søndergaard, L. Cleemann, L. Zhong, H. Becker, *Electrocatalysis* **2018**, *9*, 302–313.
- [85] S. M. Sharma, R., & Andersen, *ACS Catal.* **2018**, *8*, 3424–3434.
- [86] K. Kinoshita, J. Lundquist, P. Stonehart, *J. Electroanal. Chem. Interfacial Electrochem.* **1973**, *48*, 157–166.
- [87] R. Lin, B. Li, Y. Hou, J. Ma, *Intern. J. Hydrog. Energy* **2009**, *34*, 2369–2376.
- [88] K. Yasuda, A. Taniguchi, T. Akita, T. Ioroi, *Phys. Chem. Chem. Phys.* **2006**, *8*, 746–752.
- [89] R. L. Xie, J., Wood, D. L., More, K. L., Atanassov, P., & Borup, *J. Am. Soc.* **2005**, *152*, A1011–A1020.

- [90] O. O. Reid, F. S. Saleh, E. B. Easton, *ECS Trans.* **2014**, *61*, 25–32.
- [91] and C. A. Ous, T, *J. Power Sources* **2013**, *240*, 558–582.
- [92] R. Alipour Moghadam Esfahani, R. B. Moghaddam, I. I. Ebralidze, E. B. Easton, *Appl. Catal. B Environ.* **2018**, *239*, 125–132.

## Appendices

### ELSEVIER LICENSE TERMS AND CONDITIONS

Apr 03, 2019

---

This Agreement between Mr. Richard Acheampong ("You") and Elsevier ("Elsevier") consists of your license details and the terms and conditions provided by Elsevier and Copyright Clearance Center.

License Number	4561630760845
License date	Apr 03, 2019
Licensed Content Publisher	Elsevier
Licensed Content Publication	Applied Catalysis B: Environmental
Licensed Content Title	Enhancing fuel cell catalyst layer stability using a dual-function sulfonated silica-based ionomer
Licensed Content Author	Reza Alipour Moghadam Esfahani, Holly M. Fruehwald, Foroughazam Afsahi, E. Bradley Easton
Licensed Content Date	Sep 15, 2018
Licensed Content Volume	232
Licensed Content Issue	n/a
Licensed Content Pages	8
Start Page	314
End Page	321
Type of Use	reuse in a thesis/dissertation
Portion	figures/tables/illustrations
Number of figures/tables/illustrations	1
Format	both print and electronic
Are you the author of this Elsevier article?	No
Will you be translating?	No
Order reference number	25
Original figure numbers	Figure 8
Title of your thesis/dissertation	Probing the influence of relative humidity and temperature on the sulfonated silica ceramic carbon electrode for PEM fuel cell operation
Expected completion date	May 2019

Estimated size (number of pages)	130
Requestor Location	Mr. Richard Acheampong 20 Michaelman Rd  Ajax, ON L1S 0C9 Canada Attn: Mr. Richard Acheampong
Publisher Tax ID	GB 494 6272 12
Total	0.00 CAD
Terms and Conditions	